University of Alberta

Mechanical Properties of Alumina/Epoxy Nanocomposites: Influence of Processing and Processing Induced Inhomogeneities

by

Gordon Mark Brown 

A thesis submitted to the Faculty of Graduate Studies and Research in partial fulfillment of the requirements for the degree of **Master of Science**.

Department of Mechanical Engineering

Edmonton, Alberta
Fall 2004

Your file Votre référence
ISBN: 0-612-95711-X
Our file Notre référence
ISBN: 0-612-95711-X

Acknowledgements

I would like to gratefully acknowledge the financial aid of Alberta Human Resources and the support of those at Specialized Support and Disability Services of the University of Alberta, throughout the course of this degree. I would like to thank Dr. Fernand Ellyin, Dr. Zihui Xia, Dr. Chingshen Li and Dr. John Payzant for their insights into the problem at hand, as well as the members of the ACME Group, who provided great encouragement, technical expertise and the occasional critique.

This work could not have been completed without the aid of the great number of people, foremost including Bernie Faulkner and the Mechanical Engineering shop technicians. Lab resources and equipment were supplied by:

Tom, Microbiology Prep Lab; Microbiology
Andree Koenig, Suncor Lab; Chemical Engineering
The Aerosol Lab; Mechanical Engineering
LeeAnn and Ruth in the Glover and Lemire Labs; Biochemistry
Don Whyte in the Mercer Lab; Pharmacy
Jim Skwarok in the Masliyah Lab; Chemical Engineering

As well, numerous analytical and experimental resources were utilized, including:

ACSES; XPS, Dimitre Karpuzov
Spectral Services; FTIR, Wayne Moffat
Earth and Atmospheric Science; SEM, George Braybrooke
Biological Sciences, Microscopy Unit; TEM, Randy Mandryk
Earth and Atmospheric Science; X-Ray Diffraction, Diane Caird

Table of Contents

List of Tables

List of Figures

List of Symbols

2P	Untreated, spherical alumina reinforced epoxy series 2P.
2F	Untreated, alumina fibre reinforced epoxy series 2F.
3F	Untreated, alumina fibre reinforced epoxy series 3F.
AS	Amino-silane catalyzed unreinforced epoxy series.
ES	Ethoxy-silane catalyzed unreinforced epoxy series.
AF1	Amino-silane treated alumina fibre reinforced epoxy series AF1.
AF2	Amino-silane treated alumina fibre reinforced epoxy series AF2.
EF1	Ethoxy-silane treated alumina fibre reinforced epoxy series EF1.
EF2	Ethoxy-silane treated alumina fibre reinforced epoxy series EF2.
EF3	Ethoxy-silane treated alumina fibre reinforced epoxy series EF3.
W_f	Weight fraction of alumina.
V_f	Volume fraction of alumina.
V_m	Volume fraction of matrix.
E_c	Composite tensile elastic modulus.
E_f	Fibre (axial) tensile elastic modulus.
E_m	Matrix tensile elastic modulus.
T	Current temperature.
T_{cure}	Cure temperature.
α_m	CTE for the matrix (epoxy).
α_f	CTE for the reinforcement (alumina).
ϵ_f	Failure strain.
σ_f	Failure stress (strength).
σ_c	Composite ultimate strength.
σ_m	Matrix ultimate strength.
σ	Far-field stress.
l	Fibre length.
r	Reinforcement particle radius.
m	Shorthand for E_f/E_m.
z	Shorthand variable in Cox Model.
b	Constant describing particle-matrix adhesion.
A	Constant relating 'ν' dependance.
B	Constant relating 'E' dependance.

M_f	Mass of fibre.
M_s	Mass of silane.
M_{air}	Mass of specimen in air.
M_{water}	Mass of specimen in water.
MM_{ES}	Molar mass of E-silane.
MM_{AS}	Molar mass of a-silane.
SD	Specific density.
AN	Avogadro's number.
SA_f	Fibre surface area.
SA_s	Silane surface area.
$SA_{molecule}$	Single molecule surface area.
ρ_f	Fibre density.
ρ_e	Epoxy (neat) density.
$\bar{P}$	Load vector.
$\bar{d}$	Displacement vector.
ϕ_m	Maximum packing factor.
ψ	Reduced concentration term.
ν_m	Matrix Poisson's ratio.
K	Calculated toughness.
a	Crack length.
W	Specimen width.
t	Specimen thickness.
Y	Shape function.
k	Stress concentration factor for curved gauge length.

Chapter 1

Introduction

Composites are materials formed of two main components: the matrix and the reinforcing phase. The role of the matrix is to shield and protect the reinforcing phase, to provide a means of maintaining separation between and the orientation of this phase, and to transfer load to and between the reinforcement. The reinforcing material does as its name suggests, but also can be used to alter the chemical and mechanical behavior of the matrix[64]. Bone and wood are examples of naturally occurring composites. Manufactured composites have an enormous range of forms and properties.

The driving force behind the use and application of composites lies mainly in the high strength to weight ratio that is provided by the incorporation of multiple types of material in one "composite" material. The ability to integrate a number of phases allows the tailoring of the properties of the resultant composite through the thoughtful selection of its constituents. This selection can be directed towards the enhancement of wear, strength, chemical resistance and thermal stability properties, amongst others. As a consequence of an increasing understanding of the relationships between constituents and the development of new constituent materials, composites are moving beyond age-old applications, such as 'fibre-glass' boat hulls, and increasingly towards refined usage in advanced structures, including the main components of satellites and airplanes [138]. Plastics are at the forefront of use and application in composite materials.

1.1 Polymers

Polymers are ubiquitous in manufacturing of consumer goods. However, the use of neat polymers in engineering structures is often restricted because of lower working temperatures[1], low strength and modulus. Through the addition of a filler material their range of application can be greatly extended. Polymeric materials are used as the matrices for composites owing to their corrosion resistance, low density and ability to be highly tailored. As well, they are usually a fraction of the cost of metallic or ceramic matrices and can be processed with much greater ease[45, 43]. Below follows a brief introduction to the synthesis, structure and properties of the types of polymeric materials that are used in composite structures. Although other polymers will be discussed for completeness, the polymer of most concern in this investigation is an epoxy. Epoxies are used for specific applications where higher heat resistance and greater toughness are required. They are easy to process, though they can also be brittle[45] and are more expensive than other types of engineering plastics.

1.1.1 Polymer Structure

Polymers are long molecular chains of covalently bonded carbon atoms.[2] They are typically created by small units called monomer molecules which chemically react to form polymer chains. Although one large molecule could be prepared in this polymerization reaction, the existence of multiple initiation sites results in the formation of multiple chains. Moreover, due to the presence of terminator moieties within the chemistry, the reaction only proceeds until an average chain length is achieved. A common form of polymerization is condensation polymerization, where reactions of monomers result in the production of an H_20 byproduct [45].

In the formation of a straight chain, monomers are simply added to the ends of growing chains or chains are themselves added linearly together. In

[1] Frequently less than 100 °C.

[2] Polymers can also be formed of other molecular backbones, as is the case with Si-O chain elastomers.

some polymers, a fraction of the molecules have multiple reaction sites that attach the growing chains together. This is called cross-linking. If the cross-linking is only present to very small degree, elastomeric polymers can form. In elastomers, the polymer chains are twisted into configurations which can be stretched elastically over fairly long distances without breaking. Examples of this are latex and rubber. However, if the cross-linking is carried out to a greater degree, the polymer will become harder and more brittle[119].

As the degree of cross-linking and polymer branching greatly affects the polymer's properties, this can be used to classify polymers as thermosetting or thermoplastic plastics. Some polymers can be either thermosetting or thermoplastic. Examples of thermoplastics include nylon, polyethylene and polystyrene[87]. Polyester and epoxy are examples of thermosetting polymers. Thermoplastics consist of linear and branched chains, whereas thermosetting polymers have a highly cross-linked structure.

The molecular bonding in thermoplastics is typically a weak bonding between adjacent molecules. These bonds, as will be discussed in section 1.3.1, are significantly affected by temperature. As temperature increases, long-range, cooperative motion of chains can result and the polymer becomes rubbery. This temperature is known as the glass transition temperature, T_g. The properties of the polymer are significantly different at high temperatures from those below the glass transition temperature [45]. Further increases in temperature cause an increased mobility of chains and melting. For cross-linked thermosetting polymers the distinction between the state above and below T_g is more difficult to define. Cross-links are stronger bonds. In a thermosetting polymer they are usually initiated with help of heat and further heating tends to cause further cross-linking. This occurs instead of melting, making this class of polymer capable of resisting moderate temperatures [119]. This is why these materials are called thermosets. Below T_g, only small-scale motion of chain segments is permitted between bonds and points of entanglement.

For many polymers, an important consideration for structural concern is the degree of crystallinity. Crystallinity is the degree to which the molecular chains of the polymer form regular patterns. Within this context, polymers

can be either amorphous, semi-crystalline or crystalline. The crystal structure has a significant influence on the physical, thermal, and mechanical properties of the polymer[119, 45]. The degree of crystallization is usually very slight in most polymers, though some commercial polymers are highly crystalline materials with well-defined crystalline morphology. Other polymers that are highly crystalline include nylon and high-density polyethylene.[3] A polymer with little crystallinity is PVC (polyvinylchloride) [87]. Completely amorphous polymers exist as long, randomly coiled, interpenetrating and entangled chains. Epoxies are amorphous polymers.

1.1.2 Mechanical Response of Neat Polymers

Table 1.1 illustrates the mechanical properties of a number of common plastics, both thermoset and thermoplastic.

Table 1.1: Tensile mechanical properties of common plastics.

	Density (g/cm^3)	Strength (MPa)	Modulus (GPa)	Elongation† (%)
ABS	1.18	41	2.3	5-25
Nylon 6/6	1.14	75	2.1-2.8	300
PEI	1.27	105	3	-
PEEK	1.32	94	3.5	-
PET	1.56	159	9.0	-
Polysulfone	1.24	74	2.5	50-100
Polyester	1.78	41	5.5	-
PC†	1.20	66	2.4	60-120
Epoxy - Der 332‡	1.18	66	2.6	4.4
Epoxy - Epon 826§	1.16	70	2.8	10.6

All values taken from the Engineered Materials Handbook. Vol. 2[87], except for: † - Fried[45], ‡ - Dow Corning[29] and § - Resolution Performance Products[103]. Values are representative and fall within the range of values provided by a spectrum of products: ie, polyesters can have strengths of 20-75 MPa and moduli of 5-11 GPa.

At low strain, deformation of most polymers is elastic[4], meaning the deformation is homogeneous and full recovery of the strain can occur over a

[3]No polymer is completely crystalline.

[4]Strain rate and temperature dependent - see Figure 1.1.

finite time. Elastic strain is the local movement of chains with respect to each other, within the constraints of mechanical impediments of chain branching and entanglement, and inter-chain bonding or cross-linking. During strain, chains must be rotated about cross-links or points of entanglement; increased cross-linking requires more energy for the same strain. Consequently, heavily cross-linked polymers, like epoxy or polyester, have reduced distances between cross-links (constituting the part of the polymer which can move freely) and chain mobility and extensibility is limited [90]. Macroscopically, this is seen as a rapid increase in stress with increasing strain (i.e., higher modulus). Although a 'linear' region frequently exists, the general response of polymers to loading is nonlinear.

Subsequent to chain extension and local chain movement and rotation, molecular mechanisms of plastic deformation commence. These can start at low strain values, but become dominant at higher strain, when longer range motion of chains relative to each other occurs; weak intermolecular bonds, such as hydrogen bonds, are broken and re-form. This is similar to motion above the glass transition temperature in thermoplastics. In thermosets, more energy is used to break the strong covalent cross-links between chains or to break the chains themselves. Often there is no defined "yeild point", marking the start of extensive plastic deformation. At higher strains, the deformation of polymers can occur by crazing[5] or by a process called shear banding,[6] frequently seen in epoxies [45, 22, 34].

Damage can also accumulate. This occurs in the bulk material along directions of maximum shear stress, as diffuse shear yielding. Brittle polymers have limited amounts of this mechanism, though it does occur in glassy polymers, like epoxy[81]. Perhaps more prevalent is the formation of microcracks and the opening or extension of microcracks created during manufacture[141].

[5]Crazing describes the network of fine cracks that is visible when the polymer is deformed to a certain level. Craze consists of polymer fibrils stretched in the direction of tensile deformation. The deformation involves a change in the polymer volume.

[6]In some polymers, regions of local shear deformation will occur. These regions are called shear bands and develop at 45 ° to the loading direction. Shear deformation is a dominant mode of deformation during tensile yielding of ductile polymers. This is a constant volume process.

The formation of these cracks is a diffuse energy release mechanism based on the creation of new surfaces. Coalescence of these cracks can result in the formation of a major or fatal crack. In brittle polymers, little yeilding is evident before failure. However, ductile polymers, including many engineering thermoplastics, exhibit a stress/strain behavior very different from this brittle response and have high strain before failure.

The mechanical response of plastics depends significantly on temperature and strain rate. Many amorphous polymer can exhibit a range of tensile behavior (from brittle to rubbery), simply by increasing the testing temperature to above the T_g of the polymer or by decreasing the strain rate. This is depicted in Figure 1.1. For example, decreasing the temperature results in a shift from a ductile to a brittle response/failure. Similarly, as the strain rate is increased, the modulus is seen to increase and is typically accompanied by an increase in the failure stress and a decrease in the failure strain[45]. Moreover, for very low strain rates or tests of long duration, polymers exhibit a time-dependent behavior and a viscoelastic response[53].

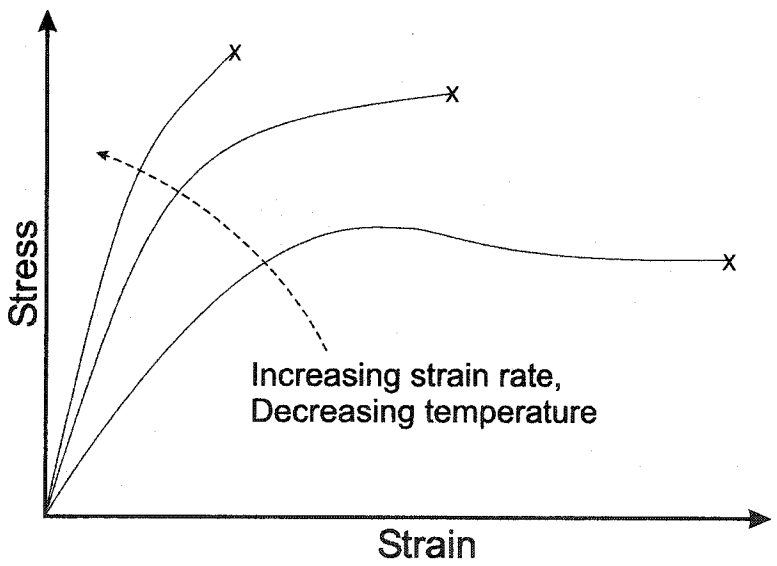

Figure 1.1: Strain-rate dependance of epoxy.

1.2 Fillers

As mentioned, neat polymers have attributes that offset their attractive cost, processability and corrosion resistance. Fillers are used to deal with such limitations. These filler materials include sand, glass beads, clay, mica and wood. Some are introduced to alleviate mold shrinkage by improving thermal stability or to alter electrical and heat insulating properties (as with graphite fibers, aluminum flakes, carbon black)[45, 61, 38, 64].

In composites, plastics can be combined with high strength and modulus fillers to provide superior mechanical properties. These constituents are then regarded as reinforcing materials and not simply fillers. For example, particulate reinforcement based on silica or carbon black is widely used improve the strength and abrasion resistance of commercial elastomers. Tires are perhaps the most ubiquitous example of this and have driven early research in particle reinforcement[35]. Fibres, in the form of continuous threads and fabrics, as well as discontinuous whiskers, are used to reinforce both thermoplastics and thermosets for aerospace and industrial applications.

Table 1.2 details some of the mechanical properties of filler materials and Table 1.3 outlines some of the properties the composites of these reinforcing materials have.

Table 1.2: Mechanical properties of common filler materials.

Material	Density (g/cm^3)	Tensile Modulus (GPa)	Tensile Strength (MPa)
Graphite	1.8	1000	2000
E-Glass	2.5	72	3450
Boron	2.35	455	2100
SiC	3.2	480	1520
Al_2O_3	3.96	380	1380
Aluminum	2.6	70	275
Steel	7.8	210	650

All values are representative; large variations exist for each material type as a result of processing variations, alloying, etc..
Data from Engineered Materials Handbook: Vol. 1[111] and Mechanics of Composite Materials[64].

Specialized fillers provide high composite strength and stiffness, though often at the expense of added cost and more stringent processing requirements [45]. Fibres are a choice reinforcement due to the ability to align them, providing directionally enhanced properties (though this anisotropy does have inherent disadvantages). Current research into new fibre reinforced composites ranges from the use of organic flax fibres [11] to carbon nanotubes [84, 77, 101]. This investigation focuses on discontinuous reinforcing of epoxy, using spherical and whisker-shaped alumina particles.

Table 1.3: Composite materials and properties.

Composite	Density	Tensile Modulus	Tensile Strength
	(g/cm^3)	(GPa)	(MPa)
Graphite/Epoxy	1.6	26	220
Glass/Epoxy	1.8	5.6	155
SiC/Aluminum	2.85	204	1460

Epoxy values from 'Mechanics of Composite Materials'[64].
Aluminum values from 'Engineering Mechanics of Composite Materials'[32].

Until recently, the size of particulate fillers used to improve polymer properties have been on the micrometer scale or larger[138, 65, 66]. As the scale of the reinforcing material diminishes, bulk values of mechanical properties give way to those approaching the theoretical limit[64, 131, 88].[7] This means that smaller particles (and/or fibers) tend to have fewer flaws, and higher strengths and stiffness than larger particles. In addition, smaller particles yield smaller stress concentrations.

New processing techniques, based on sol-gel and electro-explosion, among others, have led to the synthesis of nano-scaled fillers[65, 118]. These nanometer sized particles, "nanoparticles", have higher surface areas and the possibility of higher volume loadings than large particles. The composites formed of these reinforcing fillers, having at least one sub-micrometer dimension, are

[7]This may or may not be the case at the nm scale, for the dimensions of the filler approach that of the individual polymer chains. Compared to to the bulk material, the general trend follows for micrometer scale particles. New evidence suggests that materials approaching the atomic scale do not scale according to this rule[127].

termed nanocomposites. (In contrast, typical continuous glass fibre laminate composites, with fibre diameters of approximately 10 micrometers, can be considered micro/meso composites.)

The first nanocomposites were based on silica clays, such as montmorillonite, having a layered, nm-thin flake structure. Significant advances in mechanical, gas barrier, fire retardant and electrical properties have resulted[65] from their use. The success of silica-based nanocomposites has led to the investment of time and effort in other ceramic materials. For polymer composites, titanium oxide has been investigated owing to its use as a pigment[94, 124]. Recent interest has also been shown in other inorganic fillers, such as zirconia and alumina[65, 112]. (Previously, it was of great difficulty to reliably and reproducibly synthesize nano-scale oxide particles.)

However, the extent to which oxide particles modify the polymer properties is closely associated with the size, shape, and dispersion uniformity of the filler. The degree of interaction between the inorganic filler and the organic matrix is also significant. For example, the benefits of silica addition to polymers is due to the achievement of a more uniform dispersion of the silica by mechanical and chemical "exfoliation" of the silica galleries[8] and affecting polymerization between silica flakes[66, 71, 68, 72]. With other oxide particles the same issues arise and to discuss nanocomposites and their properties, a framework for particle-particle and polymer-particle interactions must first be developed. This now follows.

1.3 The Basis of Nanoscale Interactions

To understand the various aspects of synthesizing ceramic polymer nanocomposites and why this processing alters the mechanical properties from that of the unreinforced polymer, a basic framework for particle interactions will be presented. Much of this information comes from the field of ceramics, for the study of advanced ceramics provides almost all of the fundamentals required for the current investigation. At the same time, it is emphasized that this in-

[8]Stacks of silica plates or flakes.

vestigation is a mechanical one, though many of the fundamentals of this topic are of a chemical nature. These concepts are tools for understanding and do not constitute the basis of this work; they are typically beyond its scope. Appropriate references will direct the reader to further depth and range, where appropriate.

1.3.1 Forces and Bonding

The mechanisms by which particles, or particles and polymer chains, interact is through intermolecular forces.[9] As an example, the dispersion of nanometer sized ceramic particles is fundamentally dependent on the forces between the particles[44]. These forces are the attractions and repulsions that arise because of differences in charge, such as between electrons and protons in atoms or the strong dipole moments that exist in polar materials. Molecules form associations with each other at intermolecular separations where the attraction and repulsion forces are in equilibrium or such that a minimum energy state is achieved[70]. In some instances, both primary and secondary energy minima can exist.

The strength of a bond depends on how closely molecules are to each other. Weaker bonds are formed at large interparticle separations and are frequently considered physical bonds. For instance, in the secondary minimum, long-range attractive van der Waals forces dominate[52]. At smaller separations, primary bonding forces dominate, including covalent or electrostatic (ionic) bonds[16, 46].

Covalent bonds are the strongest bonds, formed when electron sharing between two atoms provides the lowest energy state of an orbital filled with two electrons. Covalent bonds form the basis for the backbones of polymer chains. Ionic bonds are formed by the electrostatic attractions of charged atoms. Anions and cations associate so that a stable energy minimum exists; ionic bonds are also very strong. Both ionic and covalent bonds represent short-range, chemical bonding between two atoms or groups of atoms. (When molecules

[9] As the concepts are essentially the same, we will talk about particles and molecules interchangeably.

or particles bond via these strong, primary bonds, the bonding is taken as between atoms and the greater structure then seen as a new, larger molecule,) Weaker and longer range bonds can be formed between hydrogen ions and highly electronegative anions, such as O^{2-} or F^{-}. These are important bonds in polar structures.[10] Lastly, one of the weakest and furthest reaching forces is the van der Waals forces. These are electrostatic forces due to dipole moment fluctuations that result in a net attractive force between molecules[70]. Van der Waals forces promote the agglomeration of dry powders and coagulation of particles in liquid suspension[110].

1.3.2 Surface Chemistry

Just as molecules interact according to their chemistry, so do particles, though this is the chemistry of a surface that is composed of many different chemical groups. The surface of an ideal metal oxide is an alternating lattice of metal and oxygen atoms. Yet, the surface of the oxide also contains physically and chemically bound functional groups, depending on the medium (gas or liquid) that the surface is exposed to. One of the most important of these, for interactions with polymers, is the hydroxyl group (OH)[119, 110, 70]. Van der Waals forces, though weak, act at large distances and can cause the physical (rapid and reversible) adsorption of molecules to a surface. However, such adsorption can lead to the chemical bonding of molecules to the surface and changes in surface structure.

For ceramics, chemical hydration is one of the important consequences of surface adsorption. Water vapor in air, or liquid water in solution can chemically adsorb to the oxide, mainly because of the polarity of water molecules and the surface charge of the oxide. The adsorption changes the surface such that hydroxyl groups are found chemically attached and water molecules are bound via hydrogen bonds. Hydration is a very important mechanism in processing of ceramic materials, because the change in surface structure alters the way ceramic particles interact with each other and with the liquid they are being processed in. In turn, this can affect the rate and extent of particle

[10]Containing oxygen, hydrogen or having hydrated surfaces.

aggregation in dispersions, especially if the liquid they are processed in is not water[59].

Alumina can be hydrated, altering the metal oxide lattice and forming various hydrated alumina structures, such as boehmite ($AlO(OH)$) and gibbsite ($Al(OH)_3$). An example mechanism of alumina hydration[59] is:

$$Al + AlO + H_2O \rightleftarrows 2AlOH$$
$$AlOH \rightleftarrows AlO^- + H^+$$
$$H^+ + AlOH \rightleftarrows AlOH_2^+$$

Hydration is also depicted for a general metal oxide in air and in water, in Figure 1.2.

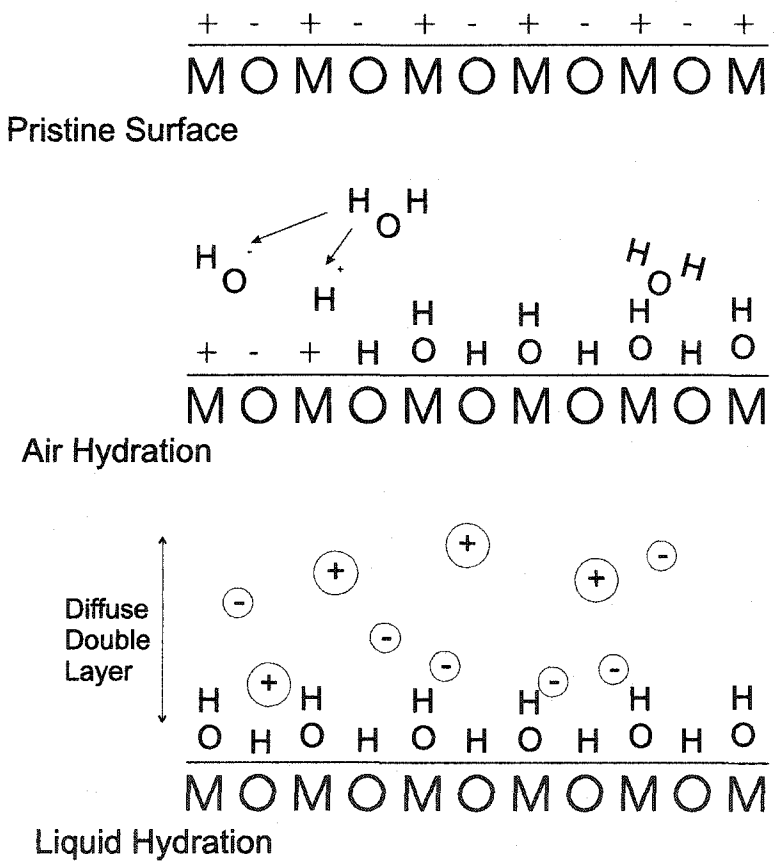

Figure 1.2: Adsorption of moisture to a metal oxide surface, changing the chemical nature of the surface. Adapted from James[59]. 'M' is a metal atom such as Ti, Al, Si; 'O' is oxygen.

Metal oxide surfaces are generally basic in nature, as is true for alumina particles. This means that in water at pH 7, surfaces will be positively charged. Above the point of neutral charge, at a pH of 8-9, surfaces will be negatively charged. The effect of this charge is to promote the association of oppositely charged counter ions, which establish an electric double layer of charge around the particle.[11] This layer forms long-range, electrostatic repulsion forces between particles and, in conjunction with van der Waals forces of attraction, is the basis for the DLVO theory (attraction/repulsion double layer theory named for B. Derjaguin, L. Landau, E. Verwey and G. Overbeek) [62, 44, 59, 48, 52, 110, 46, 70]. Although DLVO theory will not be considered in depth, the manipulation of surface characteristics to alter the way particles interact at long distances is the main method for providing stable particle dispersions and for altering the agglomeration behavior of particles in a liquid[62, 44].

Surface forces can also exist in the form of the interfacial tension when a liquid wets a solid. This wetting and spreading of liquid is actually a result of a combination of dispersion forces acting at the surface and contributions from polar forces and hydrogen bonding[106]. Surface forces are significant in nanocomposites synthesis, for both the surface treatment of oxide particles and integration of particles in a liquid matrix requires wetting of the ceramic surface. The liquid will "wet" the surface, if the angle of the liquid-solid junction is $< 90°$. The lower the angle, the better the wetting. If two particles are in contact, liquid will concentrate at the region between them and surface tension in the liquid will exert forces on the particles. If there is a narrow channel or separation of particles, this pressure is evidenced as capillary forces that both pull the particles together and draw the liquid into the space between the surfaces. The rate of penetration of the liquid into the medium will increase with higher surface tension, lower viscosity and smaller inter-surface separations. In liquids, these forces can provide a means for the cohesion of wetted agglomerates[110].

[11] These ions can be of a variety of species due to varying levels of hydration.

1.4 Powder Agglomeration

Within any powder there is a distribution of primary particle sizes. Manufacturing tolerances cause this, though improvements in old techniques and new methods are providing increasingly narrow distributions. This distribution is the starting point for the synthesis of a homogeneously dispersed particulate composite. A non-uniform distribution of particles in a composite can occur because of the clustering, clumping or aggregation of these primary particles; either prior to incorporation with the matrix or during the incorporation process. The mechanisms for this follow directly from the previous discussion.

As "dry" powders, particles are in close proximity to each other and the absence of an electrostatic double layer, as well as other repulsive forces, can result in the clumping of primary particles. This spontaneous agglomeration is the result of van der Waals forces or electrostatic attraction; the latter due to a transfer of electrons in regions of contact or to surface adsorbed ions[119, 110]. Both of these forces bring particles together and loosely bind them. Additionally, hydration of the surface can promote hydrogen bonding between the chemically altered oxide surfaces and physically adsorbed water molecules. Dry agglomerates tend to be loosely bound and weak clumps, though hydration of the particle surfaces can result in the formation of liquid bridges between particles. Subsequent dehydration of the powder can lead to strong salt-bridges between particles, forming much stronger clumps[105, 54]. Moreover, the size and strength of these agglomerates is enhanced by broad primary particle distributions, because small particles can fit into the gaps left by larger particles and facilitate the bridging of interparticle gaps during hydration and wetting[116].

In liquids, particles tend to clump because of Brownian motion, as a certain fraction of particles will invariably have enough thermal energy to overcome repulsive forces and approach to either the primary or secondary minima[110]. Due to surface charging, the process of clumping becomes more complex. The electric double layer forms a potential barrier between primary and secondary minima. Consequently, two main types of clumping exist, corresponding to

particles associating in either the primary or secondary minima. The former results in strong agglomerates, through a process of coagulation/agglomeration. These strong clumps typically contain ionic or hydrogen bonds. Flocculation is the process where particles are held in the secondary minimum, generally by hydrogen bonding and van der Waals attraction. These flocculates are weakly bound and have low packing factors[107, 119].

Clumping of primary particles also results because of chemical incompatibility between liquid and powder. The adage, "like attracts like" is borne out when a dissimilar combination of phases is chosen. Metal oxide surfaces are lyophobic/hydrophilic and in polar liquids can easily be wetted. In many inorganic liquids, however, phase segregation can occur and particles clump together to reduce the surface area exposed to the lyphilic or hydrophobic inorganic molecules (minimizing the surface energy of the clump; a thermodynamically driven process) [107, 119, 110, 62, 44]. These clumps can become large if enough time elapses and their formation can be accelerated by gentle agitation[73, 74].

For previously agglomerated powders immersed into a liquid, similar patterns arise, with smaller clumps becoming larger clumps (typically weak flocculates). However, capillary forces also come into play[110, 115]. Liquid wetting the clump surface will enter spaces between particles and can further strengthen the clumps, if the liquid can form a bridge between particles. As this force is related to surface area, the particle size and geometry have a role; smaller particles mean increased compressive forces and alignment of primary particles in clumps will cause smaller spaces and stronger bonding. Non-wetting of surfaces by liquids can result in persistent clumping and perhaps a greater extent of phase segregation.

1.5 Mechanical Mixing and Settling Processes

The process of integrating the reinforcing phase with the polymer is a nontrivial issue for inorganic nanoparticles. Both the chemical differences and small size/large surface areas present an enormous challenge to achieving a homo-

geneous distribution. Mechanical mixing is the process of separating particles enough that the liquid (in this case, polymer monomers) can get between the particles and prevent their bonding to each other. It is also the addition of kinetic energy to the system to aid in the wetting of the larger clumps and particles, and the breakdown of larger clumps into primary particles.

When a powder is first mixed into a liquid, the clumps of powder contain occluded air which must be displaced by the liquid. As the liquid wets the outer surface and is drawn into the clump, air trapped within the clump becomes compressed. Wetting, penetration of liquid and pressure buildup continue until the pressure of the occluded air balances the capillary force of liquid entering the clump. The powder within the occluded air bubble cannot be wetted unless the clump is broken and the air is released[105].

Typically the dispersion of particles and the shift in particle size towards a finer particle fraction (breakdown of clumps) occur together, though low-energy mixing can often promote the flocculation of primary particles. In fact, at any time both fragmentation of larger particles, and the re-agglomeration of smaller particles and clumps occur. Adding energy to the system simply shifts the equilibrium particle size; if enough time elapses during mixing, this equilibrium will be achieved. Higher energy mixing establishes high shear gradients in the liquid. These cause the movement of particles and exert forces on larger clumps that break them into smaller clumps. The higher the gradients, the lower the scale of mixing and the finer the particles that can result[73].

Ultrasonic mixing is a prime example of a high energy density technique for particle size reduction and dispersion.[12] Ultrasonic mixing involves the high frequency/low amplitude vibrations that cause pressure gradients in a liquid. The pressure gradients result in the formation of micrometer size bubbles that, upon collapsing shortly after formation establish high shear gradients in the liquid and tremendous forces at particle and clump surfaces. The shock waves

[12]Ultrasonic processing of powder is extensively documented and information on fragmentation rates, particle size and strength, and energy input required, amongst other topics, can be easily found [73, 74, 132, 58, 41, 129, 105].

caused by bubble collapse can induce surface damage and the fragmentation of brittle materials. The implosions also have the effect of accelerating small particles to high velocities, which can later collide with large clumps and aid in their breakdown [41, 129, 74]. Ultrasonic processing has been used in the synthesis of numerous nanocomposites systems [8, 139, 80, 113, 124].[13]

At the same time, gravitational forces act against the achievement of a stable dispersion of particles by separating according to density. The molecules of the filler phase repeatedly collide with other particles from all angles and randomization tends to keep any net motion downward from becoming significant. Similarly, Brownian motion of the molecules in the liquid also keeps the dispersed particles from settling. As agglomerates get larger, however, they are less affected by collisions with liquid molecules and their cumulative settling action becomes greater. Larger clumps then begin to settle faster[107]. Settling presents a significant problem to the uniform dispersion of inorganic filler in a polymer, for polymers have specific densities close to 1, while most inorganic fillers are between 2 and 5. The sedimentation velocity will increase with increasing density of the particle and increased mass of the particle or clump. The sedimentation velocity will decrease with an increase in the particle surface area or the increase in breadth of particle size distribution[99, 58].

Mixing is a time-dependent process and cessation of mixing permits the mechanisms of agglomeration and segregation to undo the benefits of mixing [99]. The small size of nanoparticles and a proclivity to aggregate ensure that these mechanisms are of importance in nanocomposite processing. Mechanical mixing can only achieve a certain particle size, beyond which the chemical interactions of particles, molecules and surfaces cannot be overcome. Consequently, ultrasonic and other methods of processing are often used in combination with a chemical means of reducing agglomeration and stabilizing the powder suspension.

[13]However, the continued presence of agglomerates or particle clumps is typically acknowledged. Ultrasonic processing only serves to increase the relative fraction of primary particles or to decrease the fraction of agglomerates; it cannot completely eliminate them.

1.6 Chemical Aids to Powder Incorportion

1.6.1 Surfactants

As mentioned in section 1.3.1, the chemistry of the liquid and the surface chemistry of the powders can be altered to improve the compatibility between the two phases. For example, alumina particles in water of pH lower than 9 can develop positive charges that result in repulsive interparticle forces[110, 48]. However, ionic materials other than water can also be adsorbed onto powder surfaces[52, 17]. In nonaqueous liquids this can also lead to particle charging[107].

Chemicals designed to adsorb to surfaces, called "surfactants", can also be used to provide a three-dimensional barrier to particle agglomeration. Chemical prevention of two particles approaching each other closely enough to become agglomerated is sometimes called steric hindrance. Although aqueous systems are most commonly stabilized by an electrostatic double layer, it is also possible to prevent coagulation with a thick adsorbed layer. This layer constitutes a steric barrier. The layer must be thick enough to keep approaching particles outside the range of attractive van der Waals forces, and it must completely cover the particle and be well anchored to it. If a uniform coating of a very non-polar organic compound is absorbed around each of two particles, the particles may contact but will not stick to each other[107]. This is because the non-polar materials have much less van der Waals attraction than highly polar oxide powder surfaces do. An effective means of accomplishing this is through the use of block-copolymers. These two-part chains have one end that is compatible with the particle and one compatible with the liquid the particle is immersed in[66, 118, 108].

Other steric barriers that are used include stearic acid, oleic acid, Menhaden fish oil and other fatty acid chains, as well as titanates and silanes[107, 24, 99, 124]. Many of these surfactants were discovered for dispersion and stabilization of particles in ceramic processes. As such, their use is temporary and their continued presence frequently obviated by subsequent processing steps, including sintering.

Further, the function of a surfactant does not necessarily include strong bonding between particles and liquid. For polymer nanocomposites this is a significant concern. The goal of controlling structure on the nanometer scale is more easily reached when the particles themselves have a chemical functionality to facilitate the integration with the matrix. For stronger attachment to the polymer chains (by strong covalent or ionic interactions), functional chemical groups need to be located on the surface of the particles[66]. Organic modification of metal oxide nanoparticles is a common method to induce chemical functionality to the surface, which can then be used for further reactions. This surface is of utmost importance in the resulting composite. For this reason, an introduction to the concept of the interface must be made.

1.6.2 The Interface

The interface is the juncture between the matrix and reinforcing phase; it is the contact surface at which the two phases interact. On a macro/mesoscopic level, this concept is easy to illustrate. Take, for example, a glass fibre-epoxy laminate. As the stiffer, stronger phase, the glass fibres take a proportionately larger fraction of the applied load. To achieve maximum strength, the matrix functions to transfer stress to the fibres. If one fibre fractures, the strength and stiffness of the composite, as a whole, will not suffer if the matrix can effectively transfer the load to the surrounding fibres. Only locally will there be an effect of this fibre break. However, transfer of the load is by shear and dependent on the strength of the interfacial bond between the epoxy and the glass fibres. The interface between the two is therefore significant and dependent on the physical and chemical nature of the reinforcing phase, and the chemistry of the polymer. It is increasingly acknowledged that the concept of the interface is a potential key to a successful composite system.

Yet it has been found that silica-based glasses and most polymers do not form sufficiently strong interfacial bonds[27, 107]. A chemical functionality is lent to the glass to improve on the bond strength, typically through the use of a silane-based coupling agent applied to the surface of the glass during

manufacture.[14] The silane bonds strongly to the glass and the epoxy, thereby improving the composite properties.

However, the presence of a third material in the composite system complicates matters. The concept of an interface becomes obscured and that of an "interphase" region similarly more illustrative. There now exists a phase between the matrix and the filler. In micro/mesoscale composites, such as laminates, the volume fraction of the interphase is generally considered to be quite small and though important to the strength, it will constitute a relatively negligible part of the modulus. Typical glass fibres, for example, are $\sim 10\mu$m in diameter, whereas a monolayer of silane is < 10 nm thick - a difference of three orders of magnitude. However, in the case of nanoparticles, the interface is of comparable magnitude to the particle and hence should contribute much more to the material properties, including the strength[60]. This scale issue is illustrated schematically in Figure 1.3.

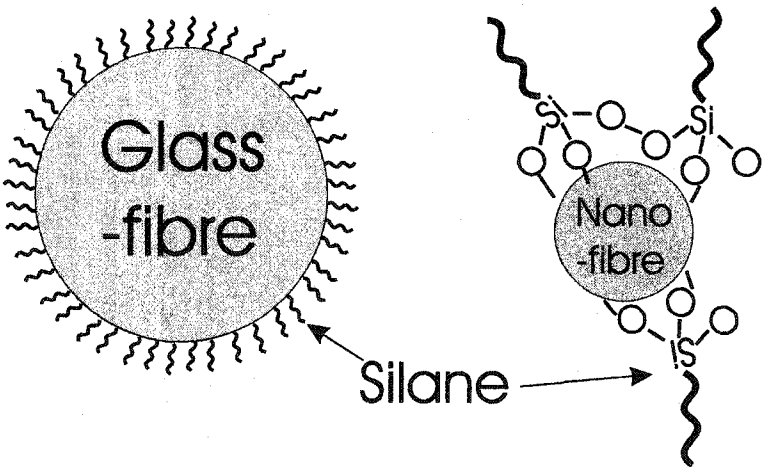

Figure 1.3: Scale of the silane-enhanced interphase.

In nanocomposite materials the interphase is a diffuse region were the properties of their reinforcement and polymer become indistinct. Filler/matrix interactions take place over a larger region and comprise both particle/polymer interactions, as well as the entanglement of the grafted molecules (coupling agents) and the chains of the polymer matrix[27, 49]. Furthermore, a uni-

[14]The silane chemistry is explained below in section 1.6.3.

form monolayer of coverage is an ideal and practically there is a more extensive interphase region, contributing much more to the diffuse nature of the interface[143, 107, 65]. The molecular scale of interactions between polymer and particle, and the added complexity of the coupling agents to the interphase region, mean that nanocomposite properties are significantly driven by micro and nanoscale structures. Control of this nanometer scale structure therefore provides the greatest opportunity for homogeneity. This consequently provides the potential for different properties than regular composites[65]. It also has important implications for modeling of nanocomposite materials, for the range of hybridization/homogenization can be simultaneously on the micro, nano and molecular level[118, 66].

1.6.3 Silanes

Since they will be employed in this investigation, a further introduction to silanes will be given here. As mentioned, silanes are commonly used dispersants and agents for interfacial adhesion improvement. Silanes are silicon-based monomers, having four chemical groups attached to the silicon atom. Typically, three of the groups are organic groups such as chlorine, amine or methoxy. They will hydrolyze in the presence of water, then self-condensed to form a stable siloxane structure or bond to hydroxyl groups on the surface of inorganic materials, including metal oxides[28]. Organic reactivity can be given to the silanes by including a chain with an organically reactive group, such as amino, chloro, epoxy or methacrylate. The choice of organic functional groups is of critical importance in achieving the maximum strength of reinforced composites[107, 109, 102]. For epoxy based polymer nanocomposites, commonly employed silanes have reactive organic groups based on ethoxide or amino (and diamino) functionality. Under appropriate conditions, treatment of metal oxides particles (like alumina) will result in the inorganic groups covalently bonded to the oxide surface and the organic functionality projecting out from the surface. The chemistry of the oxide surface is thus altered and

the potential for stronger bonding to organic polymers enhanced.[15]

Silanes are being increasingly used in nanocomposite production, as they provide a number of potential benefits above and beyond those already mentioned [107, 24, 28]. In particular, silane coupling agents can:

- physically adsorb, hydrogen bond and covalently bond to the particle
- improve resin wetting and remove water from the particle surface
- increase surface roughness
- prevent corrosion
- increase the cross-link density around the particle
- enhance transfer of stress between matrix and reinforcing filler
- protect the particle by eliminating micro cracks: prevent flaw generation
- strengthen existing particle clumps

The last two points are particularly important for this investigation because of the presence of existing clumps in the as-received alumina. These clumps alter the mechanical properties of the composite and the presence of silanes can help alleviate the detrimental impact of agglomeration.

1.7 Mechanisms of Reinforcement

Now that general concerns of fillers and their integration in the polymer matrix have been satisfied, a discussion of the mechanisms by which the mechanical properties of the polymer are altered remains. Both compliant particles (though not employed in this investigation) and rigid particles, such as alumina, are included for completeness.

[15]It is important to note that silanes bind to the surface of the oxide via hydroxyl groups. Although oxide surfaces contain some hydroxyl groups, levels of hydration affect the surface density and can alter the efficiency of silane treatment. Methods to increase silanization include pre-reactions of oxides with acids, plasma surface treatments and ionization procedures[120, 56, 118, 13, 114].

1.7.1 Elasto-Plastic Mechanisms

Let's first consider the effect of a single particle. For many brittle matrix composites, such as epoxy, rubber particles or rubber blends have been employed as counterpoint to the high strength and low ductility of the matrix [145, 90]. The philosophy behind the use of rubber is to uniformly disperse it throughout the matrix and provide widespread "structural softening" [134] for enhanced toughness or ductility. Rubber addition allows energy to be dissipated in the plastic deformation induced around the particle as the particle itself deforms; called cavitation. Also, particle debonding, coupled with deformation, creates new surface area and relieves local regions of residual strain. Both of these mechanisms can further induce bands of micro shear to originate from the particle site. As damage accumulates, the rubber can bridge the microcracks at these sites and affect a closing force on the crack faces. However, rubber addition lowers the modulus and strength of the composite, making it undesirable for some applications.

In contrast, reinforcing the matrix with a stronger, stiffer phase can enhance both modulus and strength. While a ductile rubber essentially acts as a void (though still providing some crack closure/bridging capability), a stiff inorganic phase can take more load than the matrix. Correspondingly, the strain in the filler will be lower than that of the matrix. The difference in properties causes a multiaxial state of stress in and around the particle, even for a uniaxial, farfield load. Inorganics, particularly those that are silane treated, can also cause increased rates of local cross-linking and result in an uneven distribution in local ductility [90]. The presence of the particle may initiate local microcracks in the matrix to relieve the stress and compensate for the strain mismatch.

The stress state is further complicated by a difference in the thermal expansion coefficients (CTE) of inorganic filler and matrix. For example, epoxy and alumina have CTE's of $\sim$ 60 x10^6/°C[64] and $\sim$ 7 x10^6/°C[38], respectively, meaning that cooling from the cure temperature, T_{cure}, of the epoxy, the alu-

mina will be in radial compression and experience a tensile hoop stress [134].[16] (Over time this thermal residual stress will lessen due to the viscoelasticity of the epoxy, though perhaps never entirely so[91].)

If the particle is poorly bonded, it can still enhance stiffness and strength because of this initial compressive state of stress. Poor bonding or debonding can cause void nucleation, plastic deformation and cavitation as well as shear yielding, though to a limited extent[12]. However, it is typically desired that this interfacial bond is stronger. This means more energy is required to deform the matrix around the particle and the particle can take more of the load. As well, the polymer chain extensibility is reduced, for the matrix around the particle is bonded to the particle or physically entangled with it[49].

1.7.2 Fracture Mechanisms

From a fracture mechanics point of view, stiff particles can shield approaching cracks from advancing and increase the energy release rate required to do so[21]. The particle effectively applies closure forces on the crack and reduces the crack tip opening displacement[83]. This can also be seen as crack pinning (stopping/slowing the movement of the crack front), and crack blunting, for the crack requires sharpening before further advance is possible[57]. The idea of pinning an advancing crack front was developed originally by Lange[76], Evans[42] and Green[47]. They put forward the concept of the crack front needing to 'bow' out between pinned locations and reconnect behind the impediments to enable further crack advance. The bowing causes a change in the local crack propagation direction and entails an increase energy release to do so.

Moreover, the multiaxial stress state around the particle can alter the direction of crack propagation perpendicular to the crack plane, deflecting the crack to another plane. This can result in an increase in energy as more surface area is created[98, 12]. As well, there is generally a region of zero crack

[16]The normal strain across the interface, due to the thermal mismatch, is of the form $\epsilon = (\alpha_m - \alpha_f)(\mathrm{T} - \mathrm{T_c})$, where α_m is the CTE for the matrix (epoxy) and α_f is the CTE for the fibre (alumina).

advance around the pinned location and because of local velocity gradients, an accompanying plastic deformation of the matrix. The matrix yielding, is evidenced as ridges around and behind the pinning locations, termed "rivers" or "lances"[81, 10]. As these ridges coalesce behind the particle, a comet-like appearance is created.

If the plane of the crack has shifted during this advance, a "plateau" of material on another plane may be left in the wake of the crack front. Multiple occurrences of this can lead to the formation of a series of steps that evidence increased surface area and the enhanced energy release associated with mixed mode of fracture [82, 10].

As the crack does advance, a number of mechanisms can occur to further increase energy release or slow the crack advance. Well-bonded particles, of sufficient size, can bridge the crack and continue to apply closure forces as the crack moves around it[82]. As the crack opens further, the particle can induce more extensive yielding of the matrix and will eventually debond or fracture. Although each of these requires energy, the largest enhancement of properties will correspond to the greatest energy release. Larger particles can more easily bridge the crack face and impose a larger closure forced on the crack[10, 83]. However, large particles are larger stress concentrators and as a particle can only affect material properties in its vicinity[134] smaller, more uniformly distributed particles will more extensively alter material properties. Smaller particles also have more surface area (per mass) and can therefore provide greater restriction on chain mobility and enhanced load transfer. Smaller particles also have reduced inter-particle spacing and can more effectively trap cracks[83].

1.7.3 Mechanisms Involving Clumps

Dispersion of reinforcement has a critical role for property enhancement[104]. Yet, as has already been stated in section 1.4, particle clumps do exist and are more difficult to eliminate with reduced particle size. Particle agglomeration has numerous negative consequences for particle reinforcement of plastics. Clumps evidence poor wetting between the phases; clumps can therefore have

poor interfacial load transfer and regions of interfacial debonding or other crack-like features. Such regions tend to attract matrix cracks or serve as further crack initiation sites[21, 123]. Coupling agents, as per section 1.6.3, can alleviate this problem by strengthening and diffusing the interface. The chemically bonded chains can increase the effective surface area of the clump by extending out into the matrix and enhance the interaction of the clump with the matrix[49].

Clumps make the effective reinforcement larger and both increase the stress concentration and reduce the effective volume fraction of dispersed phase. This causes less surface area, lowers load transfer efficiency and reduces restriction on local matrix deformation. Clumps are generally weaker than the material they are made of, and because of geometric constraints cannot be 100% dense. Therefore, clumps contain pre-existing void-like features and act as defects in the matrix[133, 142, 81, 128, 4, 123]. If there is extensive clumping, the effective cross-sectional area of the material is also reduced and the matrix will experience a higher stress level than that of a pristine polymer.

This does not mean that clumps do not have some benefits. Clumps can cause crack front pinning and bowing[81]. They can deflect the crack to another plane, increase the surface area of the fracture and still transfer loads. In many ways they act as reinforcement of a larger scale. However, clumps tend to fracture earlier and provide less effective energy dissipation mechanisms than a comparatively sized solid particle.

1.8 State of the Art

The stage has now been set for an investigation into the mechanical properties of alumina/epoxy nanocomposites. Within this context, the nonuniform dispersion of particles, the inhomogeneity of clumps and the bonding/integration of alumina with the epoxy matrix will be presented as influential in altering the mechanical properties of the resulting material. Prior to this discussion, a summary of sources for the introductory material, as well as the current state of nanocomposite synthesis and testing, is now presented.

Although this work focuses on nanocomposites, the majority of material concerning 'composites' centers on laminates and reinforcement of a scale larger than 'nano'. These resources are less useful than those focusing on polymers and issues of general reinforcement, mixing or fracture. Consequently, for foundational concepts, important areas of interest include:

- basic polymer science; for polymerization, gel and cure; the mechanical properties of neat polymers, etc.[45, 60, 34]
- ceramic science; for issues of ceramic surface chemistry, hydration, bonding and agglomeration, etc.[132, 110, 70, 36, 88]
- surface analysis and modification; for particle - particle interactions, particle- polymer interactions, dispersion, surface characterization, surfactants, binders, flocculants, etc. [119, 3, 18, 17, 14, 19, 39]
- mixing and particle size reduction: including ultrasonic processing[41, 73, 74] and conventional mixing[105, 58]
- particle size determination[136, 5] and sedimentation[105]
- fracture mechanisms [21, 20, 78, 22, 145, 144]

A good review of general issues concerning silica-based nanocomposites can be found in Alexandre[4]. Other non-ceramic nanocomposite investigations have focused on carbon nanotubes [7, 84, 77, 101] and carbon fibres [146, 86]. These frequently include discussion of agglomeration issues, particularly with carbon nanotubes (owing to their tangled forms). Numerous thermoplastic nanocomposite papers have been published on PMMA [146, 9, 1, 8], PE [67, 86] and PAN [139]. Works specific to epoxy and other brittle thermoset-based nanocomposites include Ng[94], Cao[23], Wetzel[140] and Singh[123].

Kickelbick[65], Gutowski[49], Schmidt[117] and others [66, 112] discuss nanoparticles and their alteration, with Gutowski providing a thorough explaination of the mechanical interactions of polymers with molecules grafted onto the nanoparticles. Chemical enhancement of interfacial characteristics is approached by Abboud et al.[1], Huh[56], and Vassileva[135] - typically using

silane coupling agents. Further insight into these interfacial issues, with a focus on silanes, can be found in compilations edited by Mittal[107, 27, 19, 39, 14] and Ishida[102, 109]. In contrast, chemical enhancement of nanoparticles during synthesis is the focus of Vogelson and others[138, 137, 75], illustrating the exceptional gains that can be made in strength and modulus via this approach (ie., increases of 700% and $\sim$ 300%, respectively).

Many general discussions of nanocomposite processing are found. Some include ultrasonic processing [101, 77, 7, 147, 123, 13, 69, 80], though details of mixing and ultrasonics are better described elsewhere [41, 73, 74, 6, 58, 129, 99]. Some only provide a brief acknowledgment of agglomeration problems [15, 94, 57, 50], though others discuss the manner in which agglomerates can be prevented [139, 24, 8, 23] and the implications of their presence on mechanical properties.

For example, Singh et al. [123] provides an in-depth discussion of mechanisms of reinforcement (including agglomeration) for brittle thermosets. Kim [67] focuses on the specifics of agglomerate deformation in ductile matrices. Wetzel et al. include agglomerate issues in the dynamic, flexural and wear characteristics of Al_2O_3 and $CaSiO_3$ composites[140]. As well, Ash reveals the detriment of clumps to enhanced ductility and failure strain in PMMA-TiO_2 nanocomposites [8].

While many papers include SEM and TEM analysis, use of digital analysis of particle agglomeration and clump morphology is lauded in a number of areas, including nano-filled films[51] and polymer blends[121].

Lastly, a great review of modeling concepts for particulate reinforcement of polymers is given by Ahmed and Jones[2]. More directed reinforcement studies concern glass bead filled epoxies [82, 81] and toughening mechanisms [98, 134, 91, 126]. Other works span a range of modeling issues in nanocomposites [25, 127, 55, 15, 135]. Further sources are found in the text.

Chapter 2

Material System

2.1 Polymer Components

The Epon 826/Epicure 9551 system is a high elongation, epoxy matrix supplied by Resolution Performance Products. The Epon 826 is a DGEBA-epoxy resin of the general form shown in Figure 2.1.

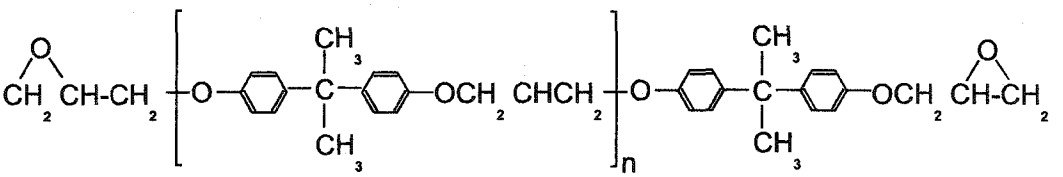

Figure 2.1: General form of the Epon 826 epoxy monomer.

The Epicure 9551 is a non-methylene dianiline (non-MDA), polyamine hardener, with a general form given as [103, 92]

$$H_2N - R[(RNH-)_nH]]_m$$

where 'n' and 'm' are integers allowing multiple functionality and branching, and 'R' is an arbitrary organic sequence.

Both components are liquids at room temperature and are combined, mixed and cured to form an epoxy solid. The properties of these components, as supplied by the manufacturer, are found in Table 2.1 and properties of the combined resin system (pre-gel) in Table 2.2. Curing is a condensation polymerization process involving the ring opening of the glycidyl $(C - O - C)$

groups[1] and a reaction with the amine groups (NH_2) of the hardener.

Table 2.1: Properties of Epon 826 resin/Epicure 9551 hardener

Property	**Epon 826**	**Epicure 9551**
Density (g/cm^3)	1.16	0.96
Viscosity at 25°C (cP)	65-95	30-70
EEW†	178-186	-
AHEW‡	-	57-67

† - epoxide equivalent weight; grams of resin containing one gram equivalent of epoxide
‡ - amine hydrogen equivalent weight (g/g)

Table 2.2: Properties of combined epoxy resin/hardener. (pre-gel)

Property	**Combined Resin**
Mix Ratio by weight (resin/hardener)	100 / 36
Mix Viscosity at 25°C (cP)	1100
Gel Time 50°C, 100g (hr)	1.3
Suggested Cure Schedule (hr/°C)	2 / 120

All information from Resolution Performance Products [103].

The Epon 826/Epicure 9551 system produces an amorphous polymer which is highly corrosion resistant, making it suitable for applications including hydrocarbon pipeline materials. It is used and tailored for filament-winding processes. As such, subsequent to mixing of the two components, a period of time, known as the pot-life, exists before the gelation and cure of the polymer system. For the filament-winding application, this time is extended and is roughly 2.5 hours at room temperature.[2] The epoxy is cured at elevated temperatures, though bulk castings require a reduced cure temperature because of the exothermic nature of the chemical reaction. Further cross-linking can be facilitated with a post-cure treatment. Cast specimens of the neat epoxy have properties given in Table 2.3[103].

[1] Also called ethoxy or epoxide groups.
[2] At elevated temperatures, pot life and gel time are reduced.

Table 2.3: Properties of neat cast epoxy.

Property	Value
T_g ($^\circ C$)	110
Tensile Strength (MPa)	69
Tensile Modulus (GPa)	2.76
Tensile Elongation (%)	10.6
Fracture Toughness, (MPa$\sqrt{m}$)	5
Coefficient of Thermal Expansion ($\mu m/m^\circ C$)	56

Manufacturer specified values. The neat resin is cured for 2 hrs at 80 °C and in the ratio of hardener:resin of 36:100.[103]

2.2 Alumina Powder

Alumina is formed of Al and O atoms, but their arrangement can be in a number of stoichiometric ratios and crystallographic forms. Pure, crystalline alumina is denoted Al_2O_3 and has α, γ and β forms. As alumina is hydrated, the relative amount of oxygen increases. Fully hydrated forms ($Al(OH)_3$) include bayerite, gibbsite and nordstrandite. Partially hydrated forms include boehmite and diaspore ($AlO(OH)$)[3]. A sample of alumina can contain a number of these forms, particularly in an aqueous environment.

The alumina nanoparticles used in this experimentation were purchased from Argonide Corporation (Sanford, Florida). They were developed primarily for use as an accelerator in solid-rocket fuel and for biological filtration[130]. Two morphologies of particles were purchased: nanosized spheres (80 nm diameter) and fibres ($2-4$ nm diameter by $50-100$ nm long).

The alumina particles, as received in 100 g, sealed packages, are powdery in form and white or slightly off-white in color. The packages were found to contain contaminants in the form of large (up to mm scale) flakes of alumina, as well as pieces of plastic sheet (the latter coming possibly from the packaging process). Use of a wire mesh to sift the as-received powder reduced the number of contaminants entering the mixing process.

Attempts to elucidate information from Argonide regarding the nature of the alumina powders were unrewarding. Although some information was found

on the internet[130, 131], most was gleaned from experimental analysis of the powder in hand:

2.2.1 XPS Characterization

X-ray Photoelectron Spectroscopy (XPS) is a surface analysis technique for determining elemental composition. In this process a sample of material is irradiated with x-ray photons that excite the inner shell electrons of atoms and cause emission of photoelectrons. The energy of these photoelectrons is characteristic of the material and provides information about the top 2-20 atomic layers[63, 18, 3]. XPS analysis was completed on an AXIS 165 spectrometer, using a αK-source, at the Alberta Center for Surface Engineering and Science (ACSES). Fibres from a freshly opened package were hand pressed onto the double-sided, graphite tape of a brass test stub for XPS analysis. The pristine powder was analyzed in three scans, with one minute of surface etching between scans. A survey scan of the alumina fibres is shown in Figure 2.2.

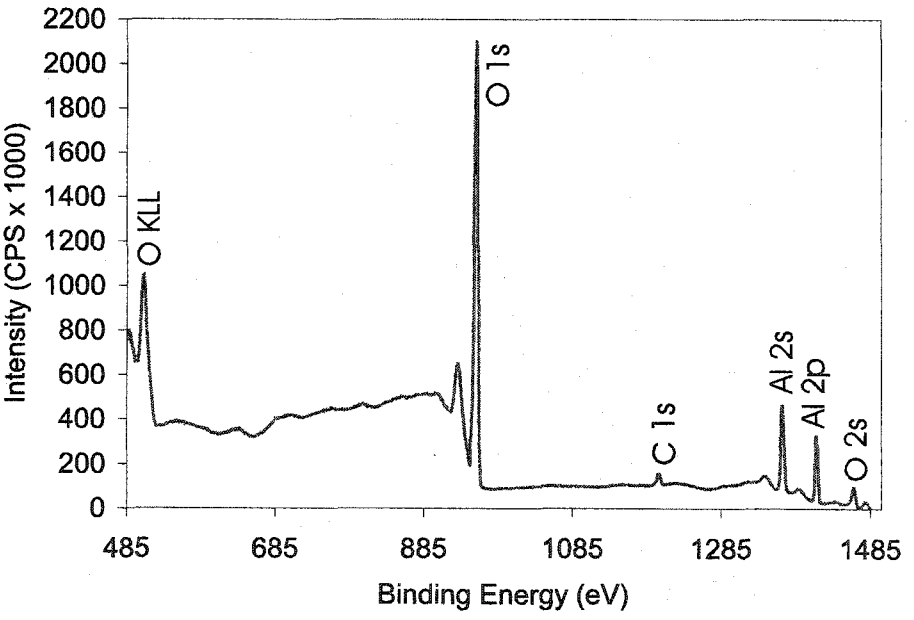

Figure 2.2: XPS survey spectra of alumina fibres.

The survey scan reveals an O/Al ratio of $\sim$ 2.1, meaning slightly more than one water molecule associated with each Al_2O_3 unit. This is very close

to the value for boehmite (O/Al of ~ 2). One minute of surface etching was used to reveal more of the interior structure of the alumina fibres. After this there was a decrease in the O/Al ratio, to ~ 1.87. As the value of unhydrated Al_2O_3 is 1.5, the interior structure is less hydrated than the surface, though still likely composed of mostly boehmite.[3]

The presence of boehmite is further supported by curve fitting of the O1s curve from the surface survey. Assuming the structure to be composed of only hydrated and unhydrated alumina[4], two curves were fitted; corresponding to Al-O-Al oxygen (O1) and Al-O-H oxygen (O2)[3]. This is shown in Figure 2.3.

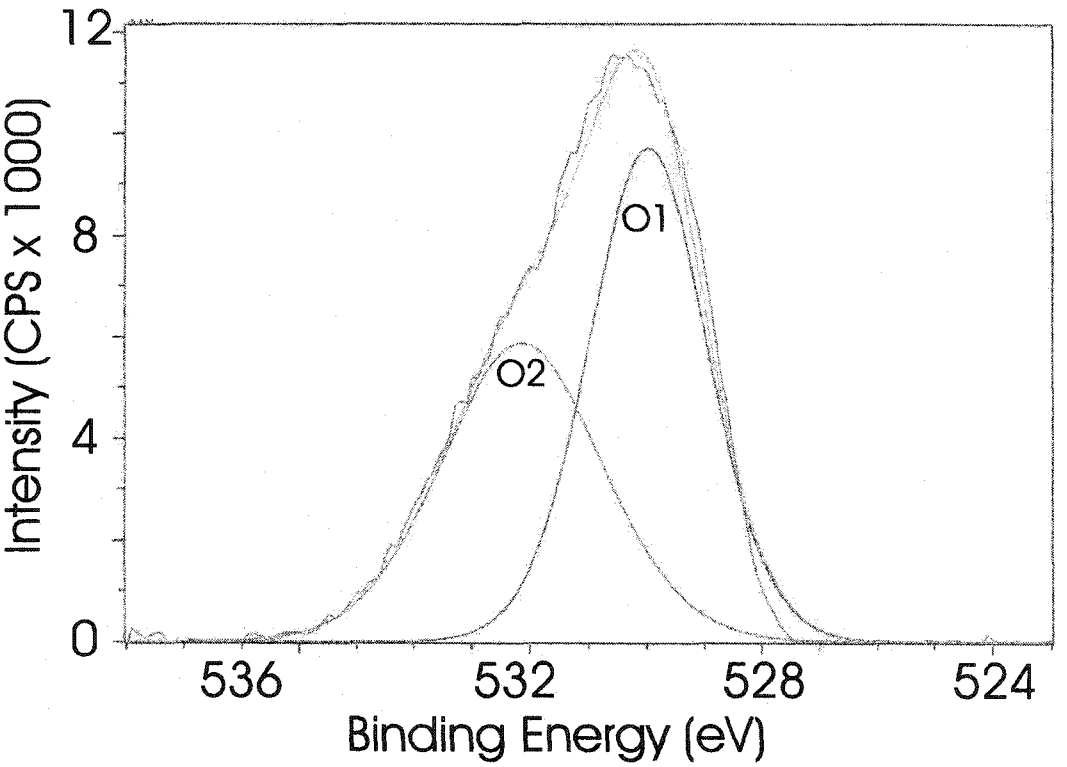

Figure 2.3: Curve-fitted peaks for O 1s core level.
Note: O1 at 529.2 eV, FWHM of 2.362 eV; O2 at 531.4 eV, FWHM of 3.198 eV

Table 2.4 summarizes the data from the fitting process. From this, we see again evidence of hydration and that the alumina is not a purely crystalline Al_2O_3.

[3]All curves are shift-corrected by 0.8 eV down in energy, according to calibrations made with the C 1s curve ($285.8eV \rightarrow 285.0eV$).

[4]Water is not considered.

2.2.2 FTIR Characterization

Similarly, freshly opened, as-received fibres were analyzed using microscopic Fourier Transform Infra-Red spectroscopy (FTIR). All testing was conducted at the MicroAnalytical and Spectral Services lab of the University of Alberta's chemistry department, on a Nicolet Magna-IR Spectrometer 750. In FTIR, the fibres are subjected to infra-red radiation and either the absorbance or transmittance of specific frequencies of IR energy is detected. Results are typically shown as a graph of the absorbance or transmittance versus wavenumber, in cm^{-1}. The wavenumbers correspond to the vibrational frequencies of specific bonds[18, 17], hence, the composition of the sample can be determined.[5]

Results of the analysis are shown in Figure 2.4. Amorphous alumina was found (as determined by comparison with standard reference texts), though amounts of specific oxides could not be determined.

2.2.3 Particle Size Determination

Primary particle size distribution was determined using SEM micrographs of fracture surfaces (discussed in Section 4) and TEM micrographs from Argonide [130]. They show a narrow distribution of fibre diameters (though having a range of aspect ratios) and a broad range of sphere diameters (40 nm to several microns). However, an initial determination of the actual clump and particle sizes was made for both sphere and fibre powders, owing to the knowledge that particle clumps of significant size exist. This was made despite the information

[5]This includes hydrogen, which cannot be detected with XPS.

Table 2.4: Hydration information from O 1s curve fitting.

Material	O : Al
Al_2O_3	1.5 : 1
$AlO(OH)$	2 : 1
$Al(OH)_3$	3 : 1
Fibres - fresh surface	2.1 : 1
Fibres - 1 min etching	1.87 : 1

supplied on the web by Argonide[130] in 2002, suggesting little agglomeration was present. In fact, newer information recently published on the web (2004) by Argonide[131] acknowledges agglomeration and provides more details than before.

The particle size determination was made by first briefly sonicating a small mass of dried powder in de-iodized water (to fully wet the powder). Small amounts of this mixture were then pipetted into the mixing chamber of a Mastersizer particle analyzer. This apparatus uses a laser to determine sample information, via light diffraction[110]. In all analyses, laser obscuration was between 13.5% and 15.5%, and a software model based on a refractive index for alumina of 1.78 was used. (The practical detection limits of this machine are 0.2μm to 2 mm.) Two sets of results were obtained and averaged for each sample.

Figure 2.5 shows the distribution histogram of particle size versus the volume percentage of the sample in that range, for both spheres and fibres. Figure 2.6 shows the same data as a cumulative fraction distribution. In both cases, the actual particle size ranges between 0.4μm and 275μm, revealing extensive

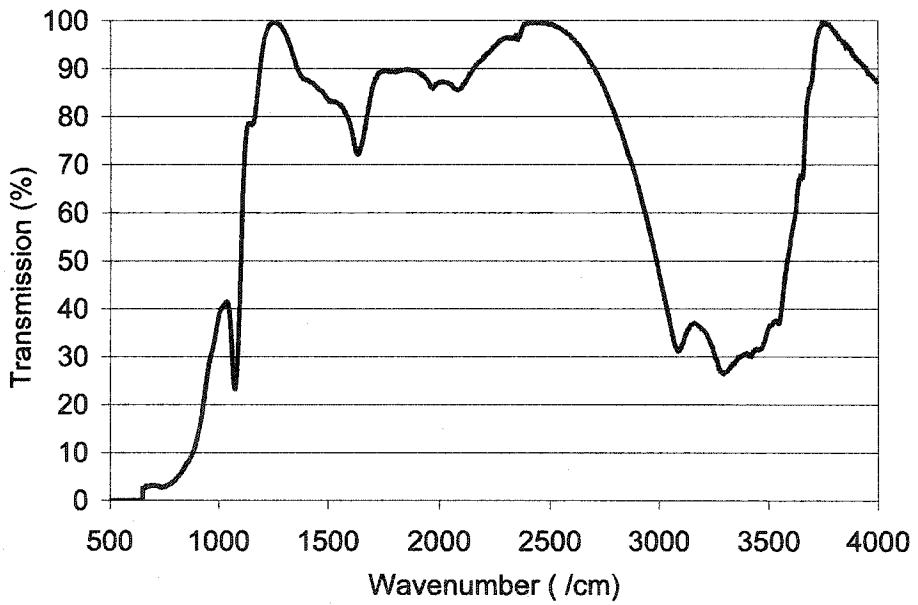

Figure 2.4: FTIR spectrum for pristine alumina fibres.

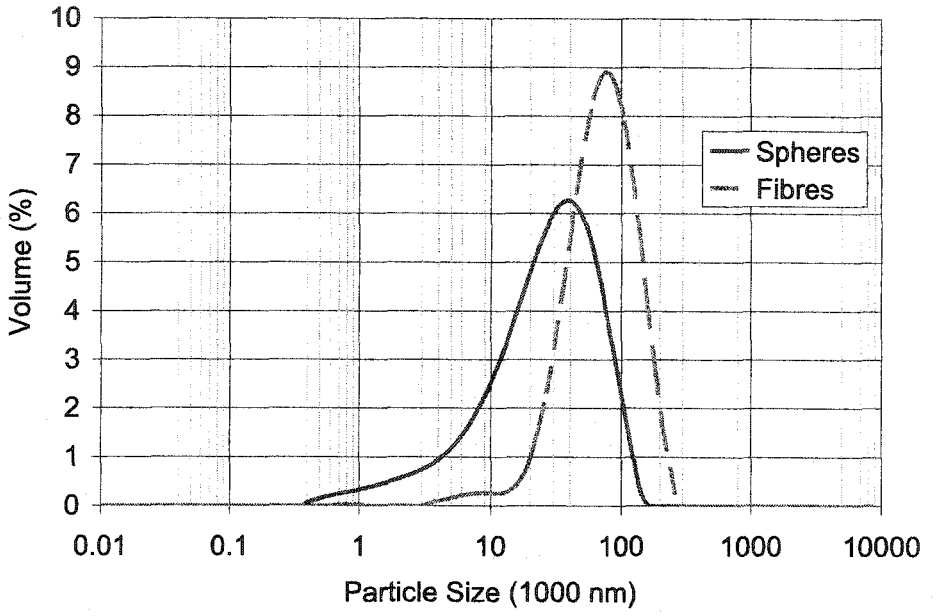

Figure 2.5: Histogram of particle size distribution for alumina spheres and fibres based on laser light diffraction.

clumping of particles. The spherical particles have a 50^{th} percentile diameter, D_{50}, of $\sim 31\mu$m and the fibres have a D_{50} of $\sim 76\mu$m. Surface areas, calculated based on the assumption of spherical, or equivalently spherical, particles are $0.762 m^2/g$ and $0.167 m^2/g$, respectively.

Determination of clumping correspondence with the corrected information released by Argonide, suggesting that the bulk density of the fibre aggregates of boehmite is $\sim 0.71 g/cc$. These clumps are therefore $\sim 75\%$ void space with < 10nm spacings between fibres[131]. A summary of the alumina analysis is provided in Table 2.5.

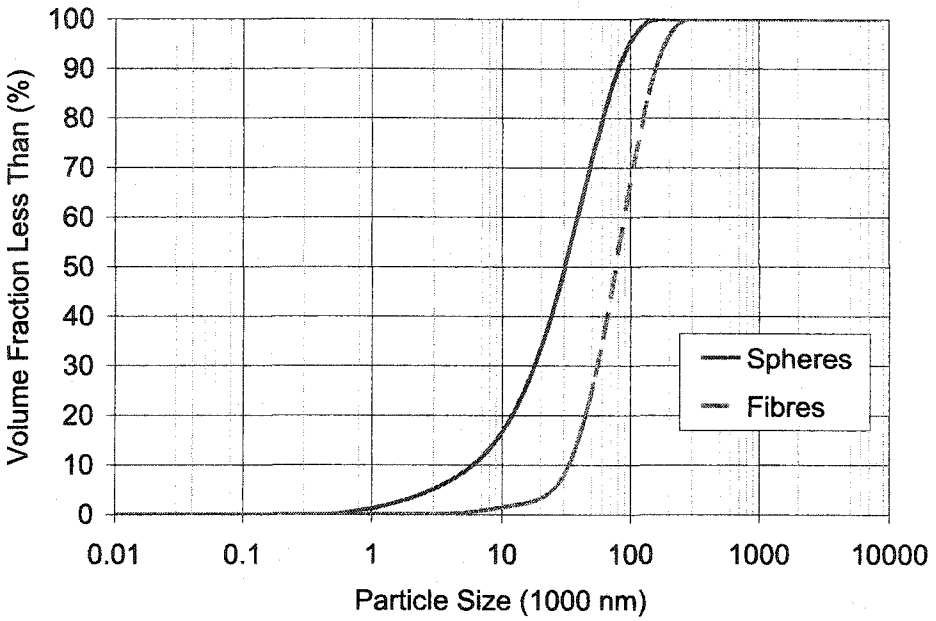

Figure 2.6: Cumulative distribution of particle size for pristine spherical and fibre alumina.

Table 2.5: Measured properties of alumina.

Property	Alumina	
Morphology	Spheres	Fibres
Particle Size:		
Primary Particle(nm)	80	2-4 x 50-100
Clump, D_{50} (μm)	31	76
Specific Surface Area:		
Primary (m^2/g)	300	700
Clump (m^2/g)	0.76	0.17
Surface Composition	hydrated (boehmite)	
Bulk Composition	boehmite/Al_2O_3	
Theoretical Density (g/cm^3)	3.0	
Bulk Density (g/cm^3)	0.71	
Density (assumed†)	3.5	

† - Based on 50% alumina and 50% boehmite.

Chapter 3

Experimental Procedure

3.1 Preparation of Neat Epoxy Specimens

3.1.1 Casting of Epoxy Plates

As the epoxy is a two-part liquid system, a solid polymer plate was first made. The epoxy resin was preheated to approximately 60 °C prior to this mixing, to allow the melting of crystalline solids (present due to storage), and the lowering of the viscosity for enhanced mixing and the escape of air bubbles / volatiles. The hardener and epoxy resin were then combined and thoroughly mixed, via the mechanical shear imposed with an impeller-type mixing blade[1] (hand drill or drill press driven). Previous works determined that a mixing time of > 5 minutes was sufficient for this purpose[53].

A major concern in the curing of filler-modified epoxy resins is the competition between removal of out-gassing bubbles and settling of filler materials.[2] This is especially significant for agglomerated filler materials and the fractions of the incorporated filler that are not uniformly or stably dispersed. Initial mixing tests revealed that the majority of poorly dispersed filler and large filler clumps settled into a thin layer at the bottom of the mixing container soon after cessation of mixing.

For the neat epoxy specimens, particle settling is not a concern; however, making thinner specimens reduces the distance that bubbles, either those incorporated during the mixing process or those formed during polymerization,

[1] Dantco Industries, USA

[2] The specific density of alumina is > 3 and epoxy is ~ 1.15.

must travel to the surface. It was decided that casting specimens in a mold open to the air, having a large surface area and a reduced plate thickness would alleviate this problem in the period before gel and after mixing. For the composite specimens, the thickness of the resulting plate could not be excessive, yet would have to account for a region of settled filler. The plate thickness was chosen such that the entire specimen thickness would be comprised of a uniformly dispersed region from the middle portion of the cast plate.

A steel mold was created, having interior dimensions of 228.6 x 266.7 x 25.4 mm. The mold was designed as a generic open-faced, plate mold, with the capacity to incorporate a mold top for vacuum-applications. Surfaces of the mold were ground to help removal of the cast epoxy plate. The mold would allow the production of approximately $9 - 11$ specimens per cast plate, using a total volume of approximately 300 ml of the epoxy-hardener system. The mold is shown in Figure 3.1.

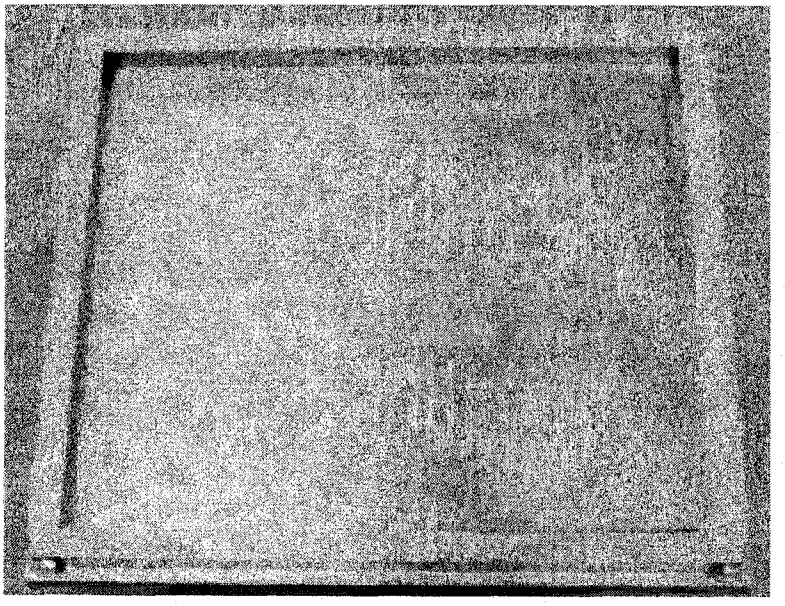

Figure 3.1: Casting Mold

After leveling of the mold in the cure oven, a mold release agent, "Freekote", was sprayed on the mold's inner surfaces to ease removal of the cast epoxy plate. The mold release agent was allowed to evaporate (air cure) prior to pouring of the epoxy-hardener system. The mold was then preheated to a

temperature of 60 °C. The preheating of the mold was used to both ensure a rapid rise in the initial cure temperature (due to the large mass of the mold), as well as to permit expansion of the steel pieces to seal the mold and prevent leaking. The epoxy/hardener system was poured into the mold and cured.

3.1.2 Gel and Cure

In filament winding applications, the pot life marks the limit of use for a mixture of the epoxy resin and hardener. In castings that contain particles, the gel time is of more consequence. After mixing of the two components of the polymer system, polymerization of the monomers begins. Initially the viscosity of the system is reduced. During this time volatiles escape; filler more dense than the polymer begins to sink. However, as the liquid transitions from linear and branched molecules to a network of chains the viscosity increases and a higher fraction of the system forms an insoluble gel. At the gel point the molecular weight of the resin is very high and the system is rubbery[60]. (At an initial cured temperature of 60°C, the gel point is found to be $\sim$ 23 minutes.) After this point, volatiles can not as readily escape and filler can no longer settle. Raising the temperature beyond the gel point causes cross-linking of the polymer chains and the transition to a glassy state. Higher initial temperatures reduce the gel time, but with bulk castings the possibility of polymer degradation from high temperature becomes significant[53].

For the Epon 826 epoxy and Epicure 9551 hardener system, a cure cycle of 80 °C for two hours, followed by a post cure at 120 °C for 2.5 hours, is suggested by the manufacturer[103]. This has been optimized for filament-wound applications. Following the manufacturer's schedule for bulk castings, the actual temperature far exceeds the designated temperature of 80 °C and reaches approximately 150 °C with the exothermic heat of polymerization. At this elevated temperature not only is cracking possible, but there is an increase in volatile production and a reduction in cross-linking of the polymer. Consequently, previous castings involved a cure at 50 °C for two hours, followed by a post cure of 120 °C for 2.5 hours[53]. This two-stage cure permits adequate cross-linking without the risk of local overshoot in temperature.

In this experimentation an initial cure cycle of 60 °C for 70 minutes was employed, followed by a post cure at 120 °C for 2.5 hours. The increase in temperature was used to account for a reduction in the bulk volume of material compared to previous castings and also to more quickly reach the gel point of the polymer. This cure cycle was affected using computer control of a small oven, employing software developed in-house[141]. From room temperature, an initial rise of 4.0 °C/min is used to reach the initial cure temperature. This temperature is held for the 70 minutes of initial cure, followed by a similar rise at 4.0 °C/min to the post cure temperature. This temperature is held for the designated post-cure period, followed by a decrease in temperature at −0.83 °C/min to room temperature. The cast plate and mold are permitted to cool to room temperature within the oven for relief of residual stresses.

Following cure, the epoxy plates were easily removed from the mold because of the slight contraction of the epoxy. For the 300 ml volume of epoxy-hardener system used, the resulting plates had dimensions of approximately 228 x 266 x 6 mm.

3.1.3 Machining the Specimens

Modified-dog bone specimens were designed for mechanical testing. Their geometry is illustrated in Figure 3.2. These specimens are a departure from the ASTM D-638[31] standard tensile specimens, because of the need for a reduced specimen thickness and to allow for a number of tests to be conducted using one specimen geometry.

The majority of specimens were manufactured using a computer numerical control mill with the entire process requiring approximately 8 minutes per specimen. The plates were first cut into rectangular strips and alignment holes drilled into their ends. The rough specimens were then vacuum-clamped to a machining jig to prevent chatter/movement during maching. This jig is shown with a neat resin specimen attached in Figure 3.3. Specimens were machined 0.05 mm over dimension to allow for tool wear, using removable cutting tip inserts to reduce machining cost. A manufactured specimen is shown in Figure 3.4, with alignment holes still attached.

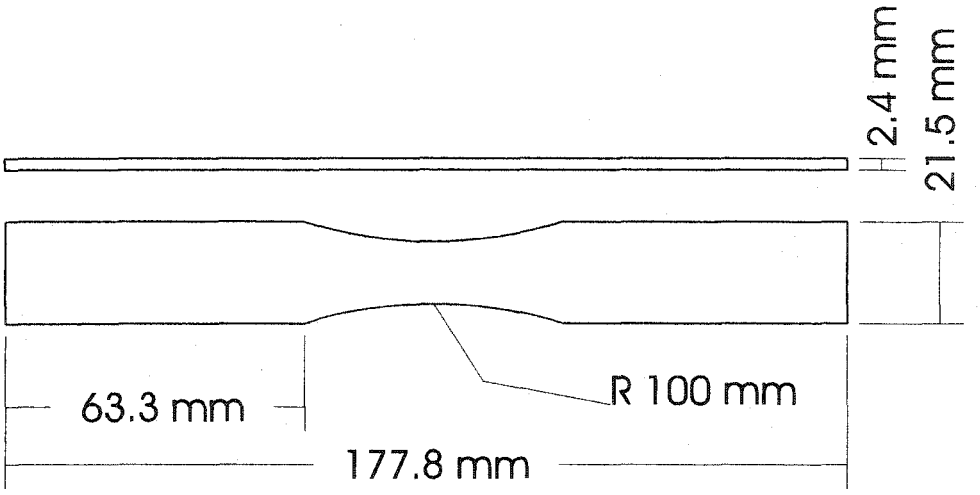

Figure 3.2: Tensile Specimen Geometry

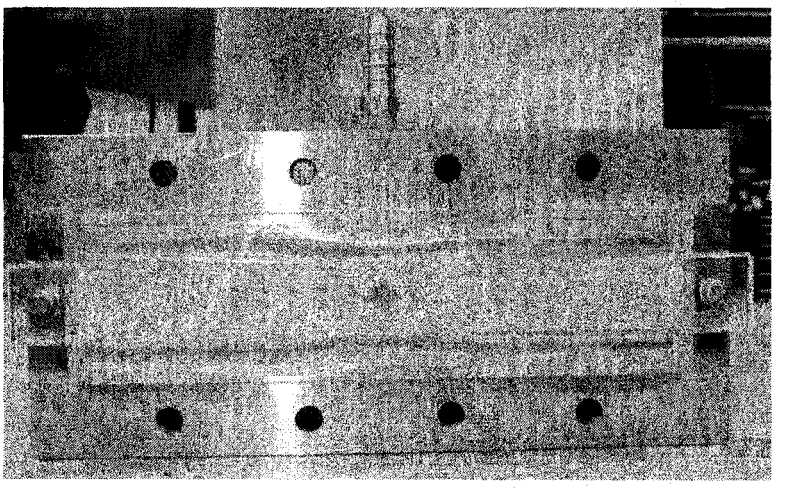

Figure 3.3: The Milling Jig Setup with Specimen.

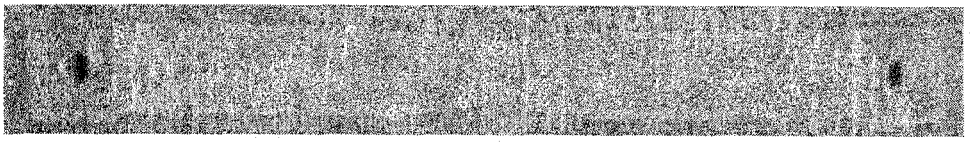

Figure 3.4: Example of Nanocomposite Specimen

All surfaces of the specimen, within the gauge-length, were manually polished using a succession of sandpapers, from 240 grit to 600 grit paper. Flat surfaces were polished on a polishing table. The 100 mm inner radius of each specimen was polished using a piece of 100 mm radius outer-surface steel pipe, covered in sandpaper, and a teflon fence to maintain a 90° edge angle. All polishing was conducted in water. Surfaces were inspected both by hand and with an optical microscope to establish an average surface quality. Final dimensions were checked and recorded prior to testing.

In order to protect the specimens from being broken in the grips during testing (being quite brittle), aluminum end-tabs were machined. An example of this is shown in Figure 3.5. Ends of the specimens were roughened using emery cloth and inner surfaces of the end-tabs roughened similarly. End-tabs were washed with isopropyl alcohol and bonded to the specimens using a 2-part adhesive (DP460, 3M, USA). The adhesive was allowed to cure overnight.

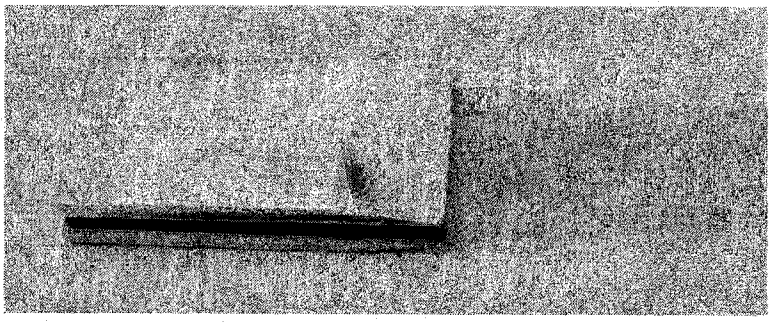

Figure 3.5: End-tab geometry

3.2 Surface Modification of Alumina Fibres

As mentioned in the introduction, a solution for improving interfacial adhesion consists of establishing covalent chemical bonds between the two phases. Consequently, some of the fibre powder was modified using silane coupling agents to alter the interfacial region between powder and polymer, and to change the agglomeration behavior of the powder. Only the fibres were treated, as it was felt that the greatest range in properties could be achieved using fibres rather

than spherical alumina.

3.2.1 Silanes

Two types of silane were employed; Aldrich - 440167 (Dow Corning z-6040) and Aldrich-104884 (Dow Corning z-6020), both supplied by Sigma-Aldrich, Canada and manufactured by Dow Corning, USA. The first is a di-amino-functional silane for coupling with the epoxy resin's ethoxide groups. It has the chemical name [3-(2-aminoethyl(amino)propyl]trimethoxysilane and its structure is given below in Figure 3.6.

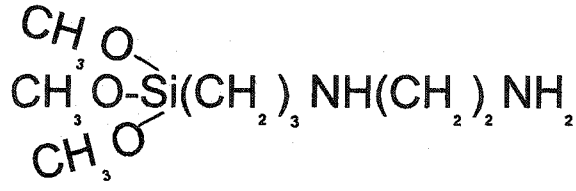

Figure 3.6: Chemical Structure of the Amino-Silane.

The second is an epoxy-functionalized silane containing a glycidyl group for reactions with the hardener's amine groups. It has the chemical name (3-glycidyloxypropyl)trimethoxysilane and is shown below in Figure 3.7.

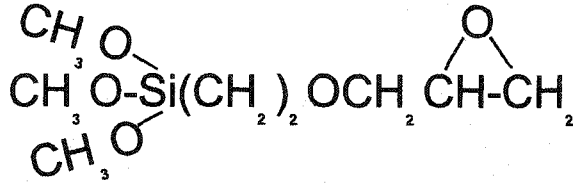

Figure 3.7: Chemical Structure of Epoxy-Silane.

3.2.2 General Silane Modification Procedure

For perfect coverage of the powder, a monolayer of silane on each primary particle is desired. Although this perfection is unachievable in practice and a non-uniform particle size distribution is known, this assumption serves as the upper limit of the coverage expected. In fact, one would expect multilayer, polysiloxane coverage of at least part of the powder surface. However, using the

surface area coverage of one silane molecule, the ideal mass of silane required can be calculated to be $\sim 1/3$ of the fibre mass[1].[3] Details of this calculation are found in Appendix A.

For comparison with pristine powder nanocomposite specimens, 5 wt.% was chosen as the maximum filler fraction. For full castings (producing 9 to 11 specimens), this means an epoxy/hardener mass of $\sim$ 342g and a filler mass of $\sim$ 18g. The corresponding mass of silane needed to treat one batch of fibre powder is therefore $\sim$ 6g. For all batches, a 25% margin was added to account for processing losses, meaning $\sim$ 8g of silane was used.

Hydrolysis of the methyl groups of the silane is achieved most efficiently in a slightly acidic liquid and an aqueous suspension was used for surface treatment.[4] This water was treated with a 0.1% acetic acid solution[5] to reduce the pH of the water to within the manufacturer's recommended range of $3.5 - 4.5$. Confirmation of pH was made using pH paper with a pH range of $0 - 6$[6].

For stable silane concentrations, a maximum concentration of 0.5% silane in water is permitted. Correspondingly, a volume of water in excess of one liter was used for each fibre treatment batch. Liquid silane was added to the acidic water and stirred magnetically for more than 15 minutes to hydrolyze and homogenize the silane. This procedure is detailed in Appendix B.

Prior to addition to the silane/acidic water mixture, fibres were dehydrated above 160°C for more than 2 hours and then cooled. Fibres were then slowly added to the mixture while both stirring with a magnetic stirrer and sonicating at low power in a 1-liter glass beaker or 1-litre graduated cylinder. (It was found that settling of the powder, during treatment, occurred in the "dead" spaces of the beaker and that the narrow graduated cylinder promoted better fibre movement.) After a period of the sonicating, the powders were mixed continuously for three days. In previous works[1, 56], an extended surface treatment (in excess of three days) was suggested. This is in contrast to the

[3]Based on the surface area coverage of one 3-(trimethoxysilyl)propyl methacrylate molecule, used by Abboud et al., as representatively close to the silanes employed here.

[4]The acidic environment causes positive surface charging of the alumina and helps hydrolyze the methyl groups.

[5]From pure, concentrated acetic acid supplied by Fisher Scientific.

[6]ColorpHast pH 0-6, EM Reagents.

15 minutes suggested by the manufacturer. However, the benefits of longer periods of mixing were reflected in small-scale surface treatment trials, where short periods of exposure to the silane had little impact on the stability of dispersions - as determined by sedimentation measurements.

After the mixing process, 1.5 mL samples of the water/silane/fibre mixture were removed at intervals from the middle of the mixing beaker. These were centrifuged[7] and the mass of treated fibres per liquid mass was determined after decanting (pouring off) of the supernatant and evaporation of the remaining fluid. These masses provided information on both the particle size of the treated fibres and the dispersion stability of the treated fibres in water.

Following mixing, the remaining treated fibres were settled and the supernatant decanted. It excessively cloudy, the supernatant was centrifuged to recover the most finely dispersed fibres.[8] Fibres were washed in methanol to remove excess silane and oven dried at 110°C for one hour. Care was taken during the washing process to allow settling of fibres prior to decanting of wash-methanol to prevent excessive loss of the fine particle fraction. Drying was used to complete condensation of the silanol groups on the powder surface and to remove traces of methanol from the hydrolysis of the silane (a byproduct).

3.2.3 Variations in Silane Modification

Variations in the treatment process were made to alter the extent of silanization and shift the particle size distribution in each fibre batch. This resulted in the production of five treated fibre types; two based on the amino-silane and three on the epoxy-silane.

AF1 The first amino silane treated fibre batch was sonicated for four hours[9] and had seven hours of high-shear mixing using a 2.5cm impeller blade. The total mixing time was three days.

[7]Beckman Allegra 21R

[8]1 hour at 20,000 G, using 250 or 500 ml tubes; with either a Sorval SLA 3000 or a Beckman J2-21.

[9]Sonifer W-375, with microtip, at 40 percent duty cycle; Heat Systems-Ultrasonics, Inc.

AF2 The second amino silane treated series involved one hour of sonicating and four days of magnetic stirrer mixing. The supernatant was decanted off and the fibres washed in 100 ml of methanol in a 150 ml glass test tube. The fibres were allowed to settle for two weeks before decanting off the methanol, re-rinsing and then drying the fibres. This step was added to reduce particle size by additional wetting of clumps in the low surface tension methanol.

EF1 The mixing of the first ethoxy silane series used three days of gentle mixing following an hour of ultrasonic mixing.

EF2, EF3 The last two ethoxy silane treated series, EF2 and EF3, were both attempts to enhance the fibre size distribution by taking advantage of the density differences and the settling of larger clumps prior to more finely dispersed clumps. The settling tests showed that after stoppage of mixing, and a settling period of $\sim$ 10 minutes, roughly a third of fibres remained in suspension. Accordingly, both EF2 and EF3 initially used $\sim$ 35g of fibres and corresponding amounts of silane for surface treatment. In each batch, the total mass of fibres was added to one liter of 0.5% ethoxy silane treated water. This was then sonicated for one hour and stirred for 24 hours. The treated fibres were permitted to settle for $\sim$ 10 minutes after stoppage of mixing and the supernatant decanted and saved. Another one liter of water (silane-treated) was added to the remaining fibres, which were sonicated for one hour and stirred again for 24 hours. This process was repeated a third time and the supernatant from each of the three steps centrifuged for one hour (in a Beckman J2-21 at 20K x G), to recover the fine fraction of treated fibres from the initial 35g used. The liquid was decanted and these fibres washed in methanol, decanted again and dried. The coarse, clumped fibres remaining after the third decanting of EF3 were also saved, washed in methanol and dried. The two parts of the third series are termed EF3-fine and EF3-coarse.

A summary of the surface modification is provided in Table 3.1.

Table 3.1: Summary of silane surface modification procedures.

	Fibre Mass (g)		Silane Mass	Mixing Time (hrs)		
	Initial	Yield	(g)	Sirring	Sonicating	Impeller
AF1	21	18	7.3	72	4	7
AF2	22	20	7	72	1.5	-
EF1	21	18	7.3	72	1.5	-
EF2	28	17	10	3 x 24	3 x 1	-
EF3fine	35	20	11.4	3 x 24	3 x 1	-
EF3coarse	-	10.5	-	-	-	-

3.3 Alumina Nanocomposite Preparation

3.3.1 Incorporation and Mixing of Pristine Alumina

Several small-scale (< 50 mL epoxy/hardener system) mixing trials were conducted to help evaluate the implementation of theoretical mixing concepts. These involved the mixing of alumina powder into the epoxy or hardener by hand (using a glass stir rod), with impeller-type high shear blades, magnetic stirrers or using ultrasonic probe/magnetic stirrer combinations. The dispersion effectiveness was qualitatively analyzed and settling during cure observed. Agglomerate size was investigated using an optical microscope. Hand mixing, high shear (< 3000 rpm) and mixing using magnetic stirrers all showed minimal impact on dispersion stability and clump reduction.

Ultrasonic mixing was observed to be the most effective agglomerate reducing and powder dispersion mechanism. The dispersion stability was enhanced with longer processing times, showing less settling after mixing and a reduced clump size. Similarly, longer post-mixing periods resulted in settling of a larger fraction of the powder. Settling rates appeared to increase during cure, prior to gelation, confirming a reduced viscosity during this period. Cured samples evidenced a distinctive sedimentary layer of powder at the bottom of the castings. Mixing in the hardener was found to be more effective than in the epoxy, though heating of the liquids by ultrasonic mixing reduced the difference to a degree.

To further elucidate the response of particle size distributions to ultrasonic processing and settling, laser diffraction experiments were conducted on pristine powder.[10] A Mastersizer Particle Size Analyzer was employed and particles were sonicated briefly (< 30sec) to aid wetting of the particles prior to analysis. The evolution of particle size for the fibre-morphology, alumina powder over a one hour period of sonicating was completed using a probe-equipped ultrasonic machine, operating at 20kHz and 20W. At intervals, samples were removed by pipette from the middle of the mixing beaker and tested. In another experiment, freshly wetted fibres were allowed to settle in the mixing beaker for one hour. Samples were removed from the middle of the beaker at intervals and tested.

In order to best observe the impact of particle dispersion and agglomeration on mechanical properties, it was decided to investigate low loadings of filler. This would permit the influence of particles and clumps on the matrix, and the proximity of clusters on each other, to be more effectively illustrated than with high alumina loadings. As the settling of alumina during cure would reduce the overall loading of the specimen, more powder than theoretically required was utilized. The initial filler weight fraction was based on the total mass of polymer system used. All plates consisting of pristine powders were manufactured using the same epoxy:hardener ratio as that of the neat-epoxy plates (100: 36 by weight). For the $\sim$ 6 mm thickness plates required for manufacturing specimens, $\sim$ 91g of hardener and $\sim$ 251 g of epoxy were used.

During nanocomposite synthesis, all powder was first mixed in only one component of the epoxy system – the hardener or the epoxy. Where mixing generated excessive heat, that could potentially damage the monomer or generate excessive fumes (especially with ultrasonic processing), an ice bath was employed to moderate the temperature at or below 60°C. Following mixing of powder in the first component, the second component of the epoxy system was added and mixing of the two-part system proceeded for a minimum of six minutes. The final mixture was then poured into a pre-heated mold and cured as per the procedure of the neat-epoxy plates. Variations in this mix-

[10]In deionized water at a pH of approximately 7.

ing procedure are detailed below. The mixing parameters are summarized in Table 3.2.

Series 1

The first series was manufactured to test the mixing principles established in the small-scale mixing trials, as applied to large-scale mixing and subsequently provide initial specimens for mechanical property determination. Spherical particles were used to facilitate visualization of dispersion using SEM. Emphasis was placed on length of mixing / extent of dispersion and very little on the interfacial characteristics of the resulting nanocomposite. For this reason, the powder was not dehydrated prior to incorporation and the epoxy not preheated to lower its viscosity.

Alumina, from a freshly opened package of 100 g, was slowly added to a 400mL beaker of room temperature epoxy over a period of 20 minutes, using a 2.5cm high-shear impeller blade (mounted in a drill press at 500 RPMs). Following this, an ultrasonic probe[11], operating at $\sim$ 200 W was used for 2.75 hours. Following mixing, hardener was added and mixed with the impeller blade (on a hand drill), for seven minutes.

Series 2

In series 2, initial mixing of the powder was conducted in the hardener, to take advantage of its lower viscosity and thereby enhance wetting of the particles (for increased matrix adhesion and particle dispersion). For the same reasons, mixing with the epoxy was done using epoxy pre-heated to 60°C, and with powders dehydrated for $>$ 2hr at $>$ 160°C to remove some of the physically adsorbed water[1]. Both morphologies of alumina powder were used, for it was envisioned that the fibres could provide potentially smaller agglomerates (smaller primary particle size), stronger agglomerates (enhanced packing factor) and better mechanical integration with the matrix polymer chains.

Mixing of the alumina spheres was completed in five ultrasonic treatments

[11] A Branson Sonifer 450 ultrasonic probe.

of approximately 15 minutes each.[12] After each increment the mixture was allowed to stand for several minutes to evaluate the degree of dispersion by noting the amount of settling, the formation of a clear, mostly liquid layer at of the top or a sedimentary layer at the bottom. After approximately one hour of mixing, little settling was noted and the mixture was deemed to have enough stability for mixing with the epoxy. Epoxy resin was then mixed into the hardener/alumina for five minutes, again using the ultrasonic probe.

The alumina fibres were initially added to the hardener over a period of 6 minutes. Again, $15-20$ minute increments of mixing of the hardener/alumina system were used. After each period, settling and dispersion were evaluated. Following an hour of mixing, it was observed that little settling was occurring and a good suspension of particles was assumed. A final 20 minutes of sonicating was employed. The hardener/alumina mixture was ultrasonically mixed with epoxy for 6 minutes. Specimens for these series are denoted '2P' for those containing alumina spheres and '2F' for those with fibres.

Series 3

All procedures for series 3 were the same as for series 2 fibres specimens, except that 18 minutes of mixing the two component system was employed instead of 6 minutes. This is because observation of settling during the pre-gel period in series 2, revealed that settling of filler was extensive. (Evaluation of gel time made during the initial mixing trials established gelation to be $\sim$ 23 minutes from initial mixing of the second component.)[13] After the addition of the epoxy to the hardener/alumina mixture, mixing of series 3 fibres was extended to ensure more fibres and more of the large fibre agglomerates were retained in the bulk of the cast plate (knowing large particles settle faster and leaving only $5-6$ minutes of settling before gel). Specimens for this series are prefixed with '3F'.

[12]Same probe as above.

[13]Both components were at 60°C, using a plate thickness of $5-10$mm and after a minimum of 5 minutes of mixing to achieve uniform polymerization.

Table 3.2: Mixing methodology for series 1, 2 and 3 nanocomposites

	Spheres (g)	Fibres (g)	Mixed in:	Duration (hrs)	Combined mixing duration (min)
1E	-	-	-	-	7
1P	22.8	-	epoxy	2.75	7
2E	-	-	-	-	7
2P	31	-	hardener	1.5	6
2F	-	31	hardener	1.5	6
3F	-	31	hardener	1.5	18

All preparations included a mixing ratio (Hardener:Epoxy) of 36:100 by weight.

3.3.2 Incorporation and Mixing of Treated Alumina

Treated fibres were incorporated into the epoxy in the same manner as untreated fibres. Ethoxy-silane treated fibres were mixed first in epoxy. Amino-silane treated fibres were mixed first with the hardener.

As some surface treatments produced a lower fibre mass than expected, the mass of the polymer system used was concomittantly reduced to maintain the desired alumina loadings. In these cases, the mold was partitioned with a steel bar so that the cast plates were of appropriate thickness, though fewer specimens were obtained from each casting. An additional fibre plate was cast using EF3-coarse fibres.

The only series with a different procedure was the AF2 fibre series, where, after mixing of both the resin components with the AF2 fibres (for 6 minutes) the fibres were allowed to settle in the mixing beaker for 10 minutes. The resin was then poured into the mold, leaving the thicker, clump-rich region of settled fibres in the beaker. This was a settling stratification procedure, intended to reduce the presence of larger clumps in the cast test specimens.

Three non-fibre series were also cast for comparison purposes. One was another neat-resin epoxy plate akin to that from which 2E specimens were machined, designated '2eB'. The other two contained either amino- or ethoxy-silane as catalysts for polymerization, in case the presence of the silane from fibre treatment (especially uncondensed silane), had an impact on the neat

resin properties. Assuming all of the silane employed in fibre treatment was incorporated in the nanocomposite plates, 5.2 g of silane were added to the neat (silane) plates; designated 'AS' and 'ES'.

These mixing parameters are summarized in Table 3.3.

Table 3.3: Mixing methodology for treated-fibre nanocomposites and silanated neat-resin castings

	Mixed in:	Mixing Time‡	Mass (g)		
		(min)	Fibres	Epoxy	Hardener
AS§	hardener	30, -, 5	-	251	91
ES§	epoxy	20, -, 5	-	251	91
AF1	hardener	900, 120, 5	18	251	91
AF2	hardener	130, 30, 5†	20	251	91
EF1	epoxy	120, 45, 5	18	251	91
EF2	epoxy	120, 30, 5	17	204	74
EF3f	epoxy	120, 30, 5	20	162	59
EF3c	epoxy	80, 24, 5	10.5	125	45.5

‡ - mixing times for stirring, ultrasonics, after both components are combined.
† - followed by 10 min of settling before pouring into mold.
§ - includes 5.2 g of silane and no alumina fibres

3.4 Specimen Filler Fraction Determination

To determine the actual weight fraction of filler, W_f, in the specimen, a technique based on specific densities was employed[64]. This was done because it is fast, simple and reliable. The process involved the measurement of the weight of the specimen in air and the weight of the specimen while immersed in a liquid. In this case, the liquid used was deionized water. It has a room temperature density of $1.0 g/cm^3$. Specimens were weighed in air using an Acculab VI - 1 mg balance, with a ± 2 mg precision. To weigh the specimens in water, a small holding jig was created of a styrofoam block and a metal rod. This was used to suspend the specimens in a beaker of water. A thin wire loop held the specimens. Specimens were first wetted down with water (to prevent air bubbles from sticking to the specimen) and then lowered into the beaker. Each specimen was completely immersed and tapped numerous

times to remove remaining bubbles. For each series, specimens were measured in groups of four or five. At least two groups of specimens were measured for each series.

Specific density is calculated as:

$$SD = \frac{M_{air}}{M_{air} - M_{water}} \tag{3.1}$$

Weight fraction is calculated as:

$$W_f = \frac{\rho_f(SD - \rho_e)}{SD(\rho_f - \rho_e)} \tag{3.2}$$

where ρ_e is the density of the epoxy and ρ_f is the density of the alumina.

Measurements were also conducted with the wire immersed to the same height, to determine how the presence of the wire would alter the results. It was determined that the wire constituted a very small fraction of the total specimen mass ($< 0.01\%$) and was therefore not taken into account. Samples of the plates from which each specimen series were cast were also measured. This was to determine the bulk weight fraction of alumina for the entire cast plate. In all calculations the resin was assumed void-free.

3.5 Tensile Testing

Testing of the epoxy was conducted in two 45kN hydraulic MTS testing machines. The first uses an MTS 442 controller with a 410 digital function generator and parallel-sided grips. The second has an MTS 810 frame, with MTS 647 hydraulic-wedge grips and a Teststar IIs DAQ system. Testing was conducted using load-control. It was determined that the expected loads required to fail the specimens would be up to approximately 3kN; hence the lowest load scale was used (with a maximum 4.5kN range).

To provide results consistent with that of experiments performed by previous investigators[53], a strain rate between 10^{-3}/s and 10^{-4}/s was adequate. This corresponds to a loading rate between 4.5N/s and 45N/s. Series 1 was

initially tested at the lower of these rates ($4.5N/s$), but subsequent testing was conducted at ($45N/s$), to increase the linearity of the response.

Tests were initiated by vertically aligning specimens in the test machine and gripping them either hydraulically or with the small, hex-bolt tightened grips (depending on the machine). Care was taken to align the grips both vertically and rotationally. Specimens were initially aligned using a plumb line on the reverse side of the machine. Subsequent aligning was conducted by measuring the distance of the specimen sides to the grip edges. Alignment in the 810 frame was made using pre-aligned stops. A loaded specimen is shown in Figure 3.8.

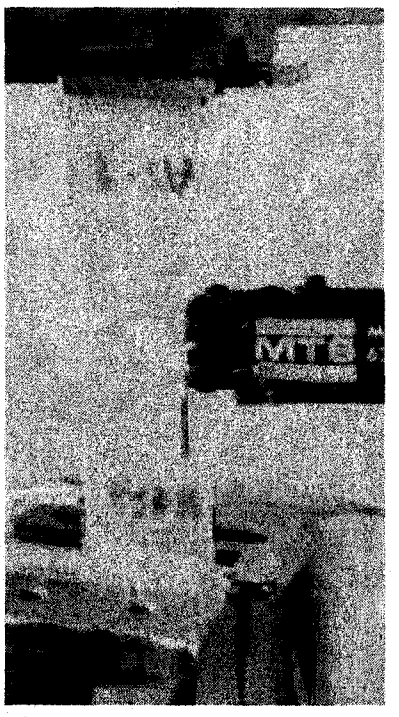

Figure 3.8: Extensometer mounted on specimen for tension/compression testing.

Controlling the loading rate, strain was left to be determined. Owing to the constant curvature of the gauge-length and the need to account for the changing cross-sectional area, an MTS extensometer was employed, having a gauge length of 7.87 mm.[14] Calibrations using an MTS screw-type calibrator

[14]Using a Zeiss toolmakers microscope to measure the distance between knife blades.

determined that the extensometer had a linear response up to 15% strain, in tension. The extensometer, shown in Figure 3.8, was attached to the specimens using dental elastics at location marked on the specimen prior to loading in the MTS testing machine.

Initial tests revealed that the extensometer provided a load noise signal and appeared steady throughout the test. The strain signal was digitally sampled using a Tektronix TDS 410A digitizing oscilloscope, after conditioning with the MTS 442 controller. The stress signal was similarly recorded. For the tests completed in the 810 frame, both signals were recorded using the software of the Teststar IIs DAQ system; the extensometer signal was an auxiliary input passing through a separate signal conditioner box.

It was initially noted that failure of the specimen always resulted at the points of contact with the extensometer knives. It was felt that the adjusting of the extensometer for zeroing purposes, as well as the pressure required to keep the knives in contact with the specimen, were resulting in damage of the specimen at the sites of contact. To determine if the extensometer knives were unduly influencing the failure stress and strain results, several tests were conducted using 3.175mm strain gauges. One gauge was used for each test, aligned in the direction of loading and affixed on the side of the specimen, in the center of the gauge length, by a technician. These tests showed similar values of stress and strain as those for previous tests, using extensometers.[15]

To compensate for extensometer damage, small patches of fabric were glued to the edge of the specimen using an "M-Bond" acrylonitril strain gauge adhesive (3M, USA) prior to extensometer mounting. Subsequent tests evidenced that these patches did indeed protect the specimen from the knives and extended the failure. Changes in specimen cross-section throughout the test were not measured.

[15]In these cases failure of the specimen was transferred from the location of the knife blades to the center of the gauge length, through the strain gauge.

3.6 Compression Testing

Compression tests were conducted to evaluate if the material responded differently in compression than in tension. Compression testing was made more difficult by the thin cross-section of the specimens; consequently, the specimens were prone to buckling. To ensure a state of pure compression, Euler buckling calculations were conducted, using the smallest width as the overall width of the specimen. Assuming both ends are fixed and mode 1 buckling, the critical load was calculated to be approximately 300 N, corresponding to approximately 0.3% strain.

Specimens were mounted in the MTS testing machine in a manner similar to that for tensile testing. Load control compression tests were conducted at a loading rate of 45N/s for 7 to 10 seconds. Load and strain data was acquired as in tensile testing. The compression tests were closely monitored for buckling and stopped when out-of-plane displacement was noted.

3.7 Fracture Testing

3.7.1 Pre-Cracking of Specimens

A series of tests were conducted on practice specimens to determine the most practical means of pre-cracking. The philosophy behind this procedure is to create a notch in the specimen, with a crack perpendicular to the desired direction of tensile loading. In metallic structures, this type of cracking is accomplished by the machining of a notch in the specimen, followed by fatigue-cracking[37]. However, fatigue-cracking is a delicate process. The point at which fracture initiates and the period of stable crack propagation can often be quite short[40]. This is especially so with brittle materials, as is the case with the Epon 826 system. Attempts to initiate and propagate a stable crack using a fatigue-cracking process were aborted, owing to the wide range of crack lengths and a large number of specimen failures.

The ASTM standard for determining the fracture toughness of plastic materials (D 5045)[30], specifies an alternative practice for initiating sharp-crack

formation in brittle plastics. In ASTM D5045, one sharply draws a fresh razor blade across the plastic specimen, or rocks the razor blade back and forth across the edge of the specimen. Attempts at this technique provided either no sharp crack tip (as determined by a optical microscope), a bifurcated crack tip or, frequently, a failed specimen. As the specimens used in this study are not of the geometry referred to by the ASTM standard and because of the shallow and irregular crack geometry formed through this process (which is also difficult to make repeatable) an alternative was devised.

Cracking of the specimens was accomplished through the use of an Instron CTK 85,000 lb-frame, hydraulic-screw testing machine. Inserted into the cross head was a small jig containing a single-sided razor blade. This jig was manufactured in-house and is shown in Figure 3.9. Specimens were pre-cracked after bonding of the end tabs, for the process of cracking creates a defect in the specimen that make it more prone to unanticipated fracture.[16] The specimen is held on edge by a steel fence and supported on a steel plate, to prevent specimen bending. The razor blade can be lowered, with a known cross-head velocity, a defined distance into the edge of the specimen. The razor blade is then removed by raising the cross-head and gently rocking the specimen off the razor blade.

A number of issues must be considered in this process. Firstly, plastic deformation of the material by the lowering of the razor blade causes residual stress at the notch. Proper alignment of the cracking jig is necessary for maintenance of the perpendicular condition of the razor blade to the specimen width, as well as the need for a crack parallel to the surface of the specimen. Additionally, at some point during the lowering process (especially at higher cross head speeds) the razor blade begins to act as a wedge, forcing apart the sides of the crack at a rate greater than the penetration of the razor blade tip. Consequently, the combination of cross-head speed and crack depth can result in the propagation of an unstable crack ahead of the razor blade tip. It is desired that the razor blade both penetrate the material, resulting in a notch,

[16] If bonding of the end-tabs takes place after pre-cracking, the number of viable specimens can be reduced by breakage.

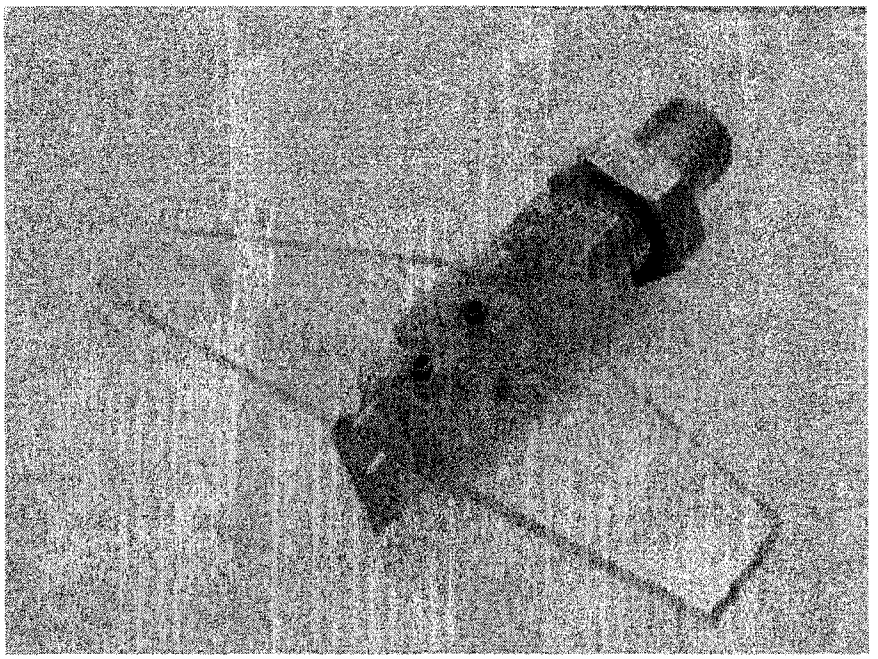

Figure 3.9: Apparatus for pre-cracking the nanocomposite specimens in the Instron Testing Machine.

and wedge the sides of the notch such that a sharp crack is created ahead of the razor blade tip (without propagating unstably through the specimen).

To determine the cross head speeds and duration of razor blade penetration to create a sharp crack of desired length, a series of tests were conducted. These tests used cross-head speeds ranging from 12.7μm/min to 127mm/min and employed times consistent with total notch and crack length dimensions of up to 2mm (or approximately 13% of the specimen width). These tests revealed bounds for stable crack tip propagation ahead of the razor blade, both on the cross head speed and the total length of the notch/crack. Repeatability of the crack/notch formation process was found for a rate of 2.54mm/min and for times corresponding to crack lengths of up to 2.5mm.

3.7.2 Determination of Crack Geometry

Determination of crack geometry and crack length was made subsequent to the cracking process. This was done using a Zeiss microscope equipped with 4, 8, 16 and 40 time optical lenses. General measurement was done optically

at a magnification of approximately 50 times. This magnification was chosen to enable the entire crack to fit within the grid of the eyepiece for easiest measurement. Details of the crack tip were investigated at higher magnifications.

Crack length, a, was determined from the edge of the specimen, taking into account the zone of plastic deformation at the notch where material protrudes from the specimen edge. The tip of the crack was specified using the shadow cast by the crack; when reducing the aperture of the microscope to shine a small circle of light to either side of the crack, the polymer transmits light except where there is a discontinuity in the material (as with a crack). The point where transmission ends is demarcated by a sharp shadow. With relative ease, the location of the crack tip can be determined. This is particularly useful for sharp-crack tips, which can often be difficult to discern.

Measurements were made on both sides of the specimen and the average value used for crack length (total crack length includes the crack notch and sharp crack regions). Variations between sides was less than 0.05 mm. This provided confindence in the cracking technique, though affirmation of a crack front parallel to the thickness was only determined post-failure and a slight curvature in the initial crack front was typically seen. This was caused during the removal of the razor blade and possibly resulted in an intial mixed mode of fracture (though slight). The geometry of the crack notch and crack tip are shown in Figure 3.10.

Measurement of crack lengths was also made optically, following failure of the specimen. These values were systematically higher than pre-crack values by a small amount. As only comparison between values is made in this investigation, pre-crack values are employed.[17]

3.7.3 Fracture Testing

The pre-cracked specimens were tested in monotonic tensile loading in the same MTS testing machines employed for tensile and compression testing.

[17]In all cases, the notch created by the razor blade is smaller than that of the razor blade itself, owing to the fact that there is elastic recovery of the strains imposed by the razor blade and the crack closes somewhat upon razor removal.

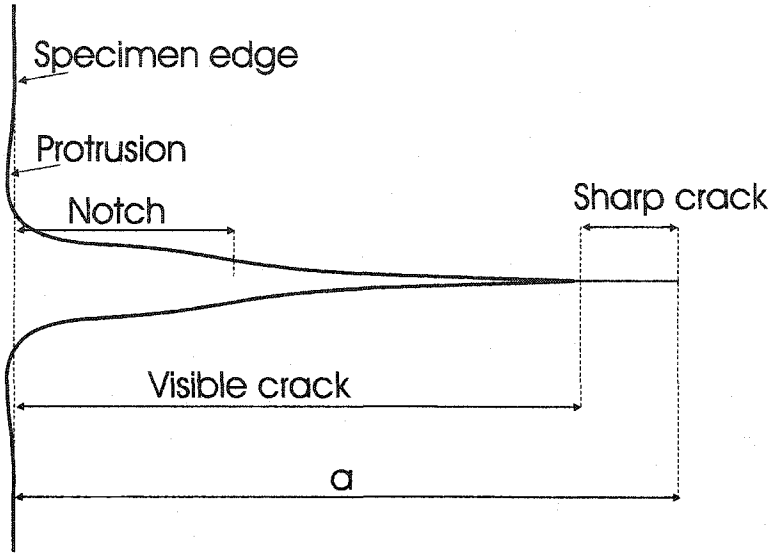

Figure 3.10: Crack notch and tip geometry.

Specimens were mounted and aligned in the grips of the machine with the cracked edge facing towards the right for each test. Tests were conducted under load control with a loading rate of 3.56N/s. Load data was acquired as in tensile testing. Stroke values were also recorded.[18] Data was collected until failure of the specimen. The specimen was then preserved for crack and fracture surface analysis.

[18]No linear relationship between strain and stroke could be determined for these machines.

Chapter 4

Results

4.1 Summary of Manufacturing

At total of 15 plates were manufactured for mechanical testing. The methods for manufacturing these plates have been discussed. Below follows a description of their general appearance and a summary of the specimens obtained from each plate is given in Table 4.1.

Table 4.1: Summary of cast plates and machined specimens.

Series	Color	Settling?	# of Specimens			
			Total	Tension	Fracture	Early Failure
1E	clear	X	10	6	3	1
1P	olive	Y	9	5	2	2
2E	clear	X	8	3	4	1
2F	olive	Y	8	3	5	0
2P	lt. grey	minor	9	3	5	1
3F	olive	Y	9	2	4	3
AF1	lt. green	Y	10	4	5	1
AF2	lt. green	Y	9	4	5	0
EF1	lt. green	Y	9	4	5	0
EF2	lt. green	Y	8	4	4	0
EF3f	lt. green	Y	7	3	4	0
EF3c	clear	all	-	-	-	-
2EB	clear	X	11	4	4	1
AS	clear	X	10	4	4	2
ES	clear	X	10	4	5	1

'X' = no significant settling; 'Y' = settled layer visible

Figure 4.1 illustrates the color and transparency variations of untreated fibre plates and Figure 4.2 does the same for treated fibre series.

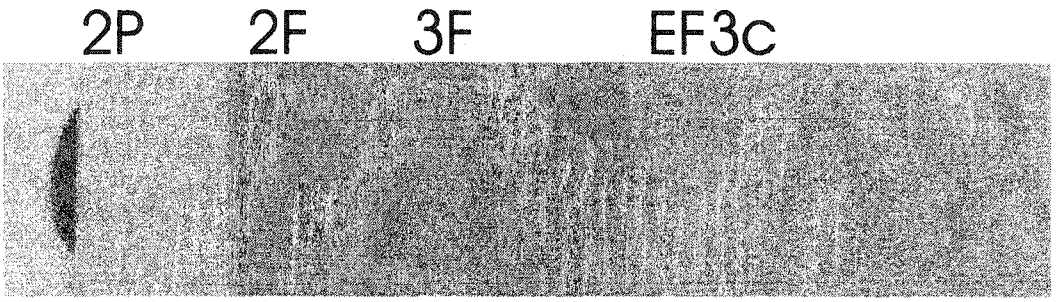

Figure 4.1: Cast plate color and transparency: untreated fibre series. Sections of plate overlay the word "GATEWAY".

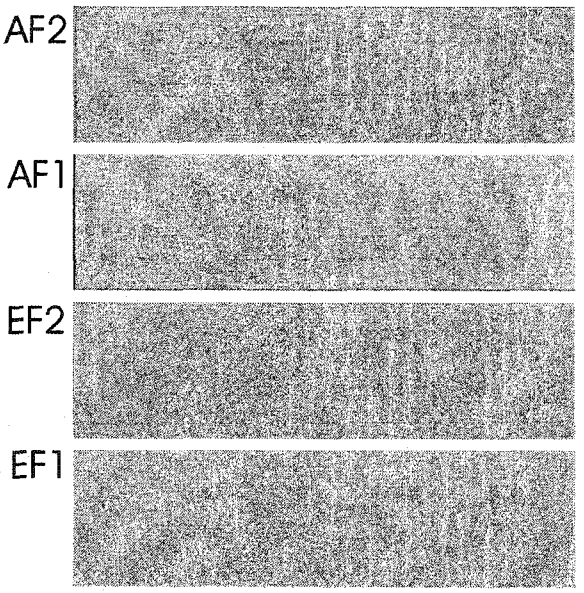

Figure 4.2: Cast plate color and transparency: treated fibre series.

4.2 Verification of Surface Modification

To characterize the treatment of the alumina fibres, microscope Fourier Transfer Infra-Red spectroscopy (FTIR) was conducted on samples of amino silane and ethoxy silane treated fibres (AF1, EF3-fine). The transmission spectra, between 500cm^{-1} and 4000cm^{-1} are shown in Figure 4.3, including that for pris-

tine alumina.[1] To allow comparison, spectra for the condensed phase amino- and ethoxy-silanes[122] are shown in Figure 4.4 and Figure 4.5, repectively.

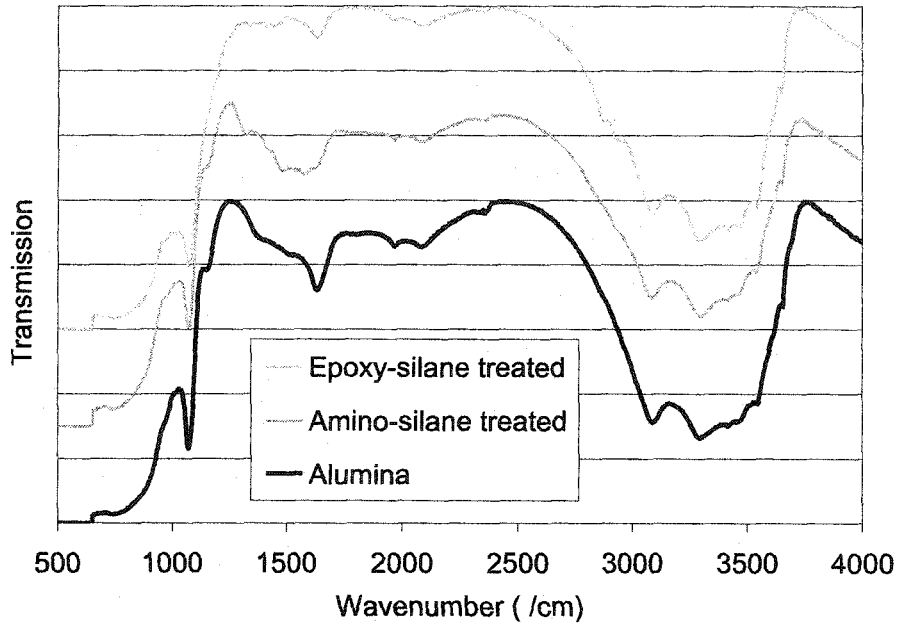

Figure 4.3: FTIR spectra for pristine alumina fibres and amino- and ethoxy-silane treated fibres.

The spectra are not particularly illustrative of the presence of silane, especially because light scattering from particle clumps results in a rotation in the baseline of the spectra - a phenomenon caused by solid-phase analysis[89]. To reveal the differences in the spectra of Figure 4.3, a spectral subtraction of these curves can be made, removing the alumina signal from the signals of the treated fibres. In doing this, the remaining bands compare much more favorably with the spectra of Figure 4.4 and Figure 4.5. Significant regions of the subtracted signals for a amino-silane treated fibres are shown in Figure 4.7, and for ethoxy-silane treated fibres in Figure 4.6.

In Figure 4.6, sharp peaks at $\sim 1130cm^{-1}$ and $1200cm^{-1}$ are suggestive of $Si-O-Si$ and $C-O-C$ epoxide stretching[14, 85]. The double peaks at $2850cm^{-1}$ and $2950cm^{-1}$ represent the distinct CH_2 stretch seen in Figure 4.5. Similarly, Figure 4.7 shows $Si-O-Si$ characteristics at $\sim 1130cm^{-1}$. There

[1]All spectra have a common scale, though they are translated vertically for clarity.

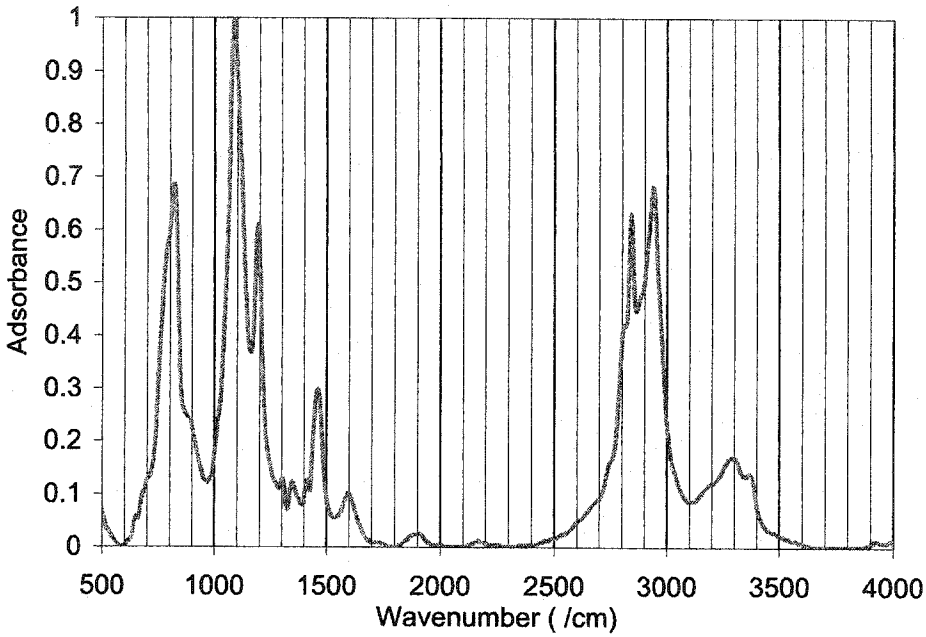

Figure 4.4: FTIR spectra for [3-(2-aminoethyl(amino)propyl]trimethoxysilane.

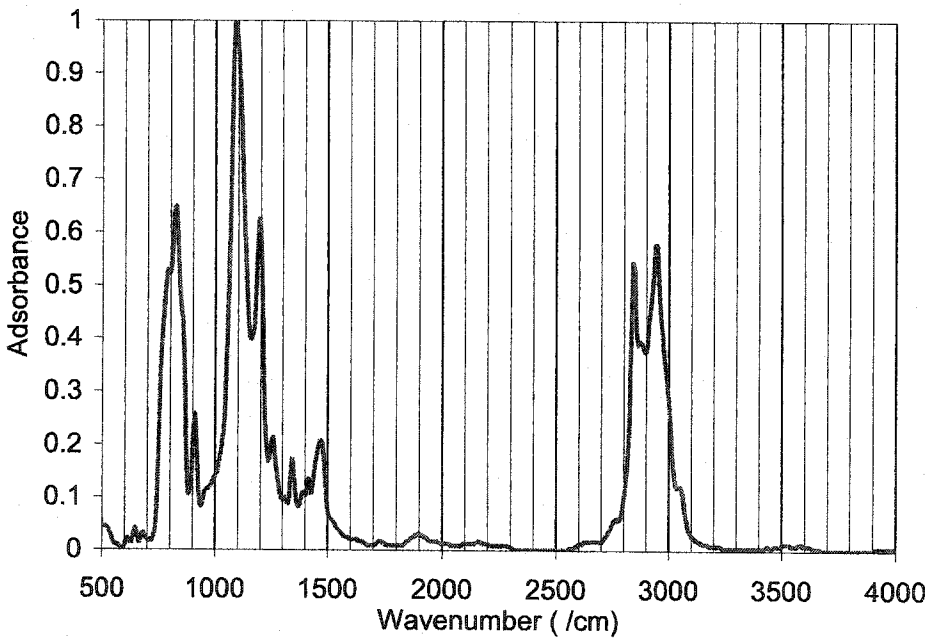

Figure 4.5: FTIR spectra for (3-glycidyloxypropyl)trimethoxysilane.

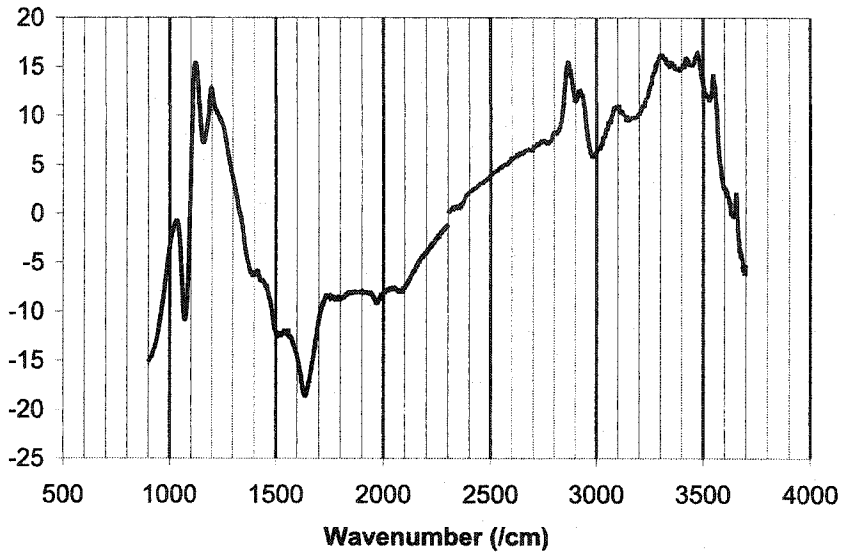

Figure 4.6: Epoxy-Treated fibre spectral subtraction.

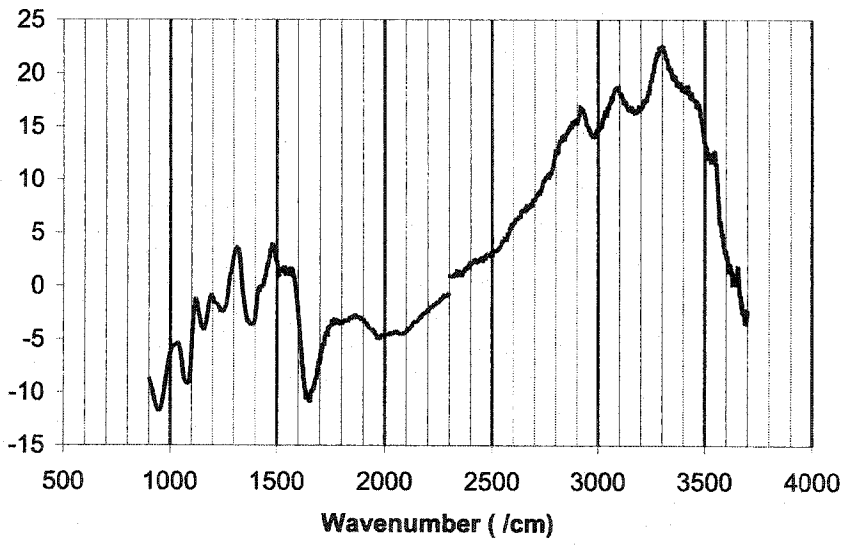

Figure 4.7: Amino-Treated fibre spectral subtraction.

are also bands visible in Figure 4.4 at $1340cm^{-1}$, $1470cm^{-1}$ and a plateau through to $1600cm^{-1}$. It is noted that a $SiCH_2R$ band is at $1420cm^{-1}$ and NH stretching at $\sim 1590cm^{-1}$. The oxide region has a number of important bands linked to amino groups, including the $R-NHR$ ($3370cm^{-1}-3280cm^{-1}$) and $R-NH_2$ ($3400cm^{-1}-3320cm^{-1}$) stretching[39, 14, 85].

4.3 Shifting the Particle Size Distribution

The use of ultrasonic processing to shift the size distribution of the fibres was seen to be effective within a very short period. This is depicted in Figure 4.8. The D_{50} of the powder (in water) decreases with processing time and the particle size distribution narrows. It is noted that in the last 30 minutes of processing the particle size begins to plateau and further improvement is minimal.

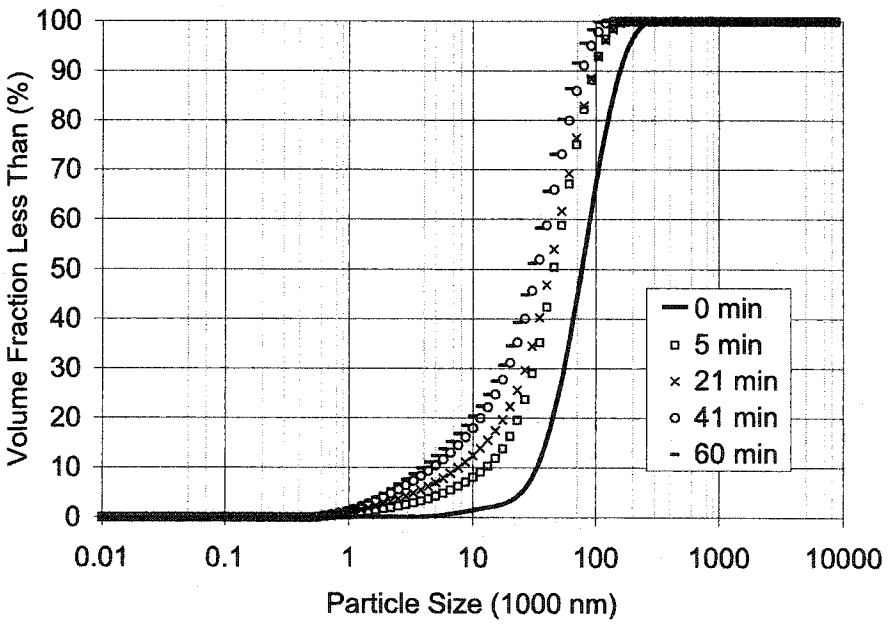

Figure 4.8: Shift in particle size distribution via ultrasonic processing.

Settling of the fibres, in water, was also found to shift the particle size distribution towards a smaller average clump size. Figure 4.9 shows the distribution of fibres remaining suspended in water after mixing has ceased. The

sedimentation rate is highest at the start and after one hour of settling the remaining fibres are much finer than even after one hour of ultrasonic processing.

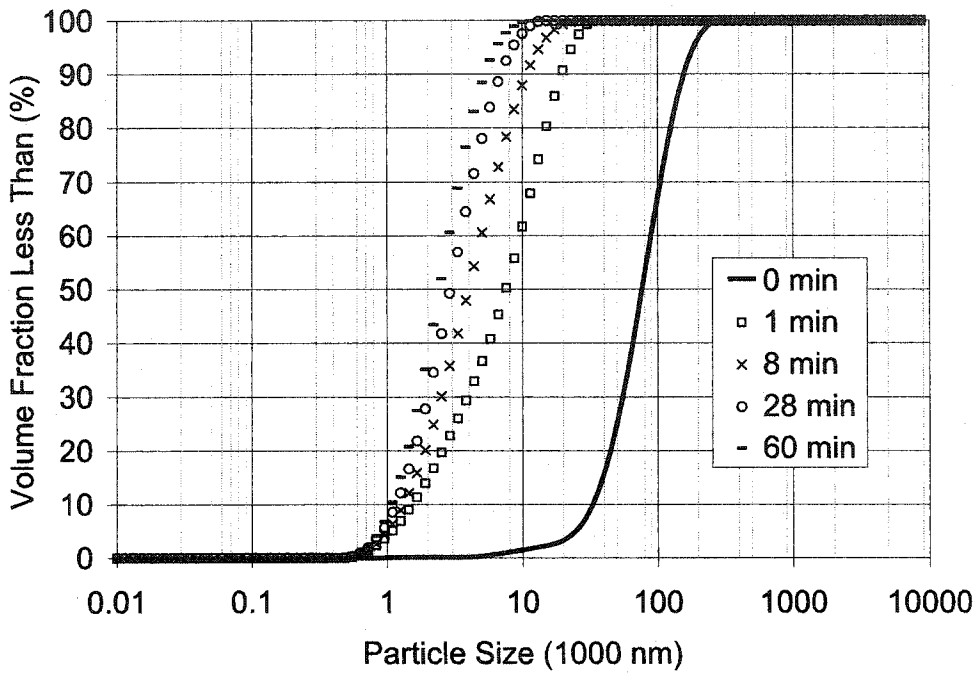

Figure 4.9: Shift in particle size distribution due to sedimentaion.

Figure 4.10 and Figure 4.11 shows the change in particle size for amino- and ethoxy-silane modified powders. Enhancement in distribution is seen, especially for AF2 fibres.[2] It is important to note the distinction between EF3fine and EF3coarse powders; the former has an enhanced distribution and the latter a larger clump size than the pristine powder. These results are summarized in Table 4.2.

[2]This could be a result of decreasing hydrophobicity and more a reflection of the suspension liquid (water) than the reduction in clump size. Moreover, the laser diffraction modeling was based on the refractive index of alumina, though the presence of silane most likely alters this value and the resulting distribution.

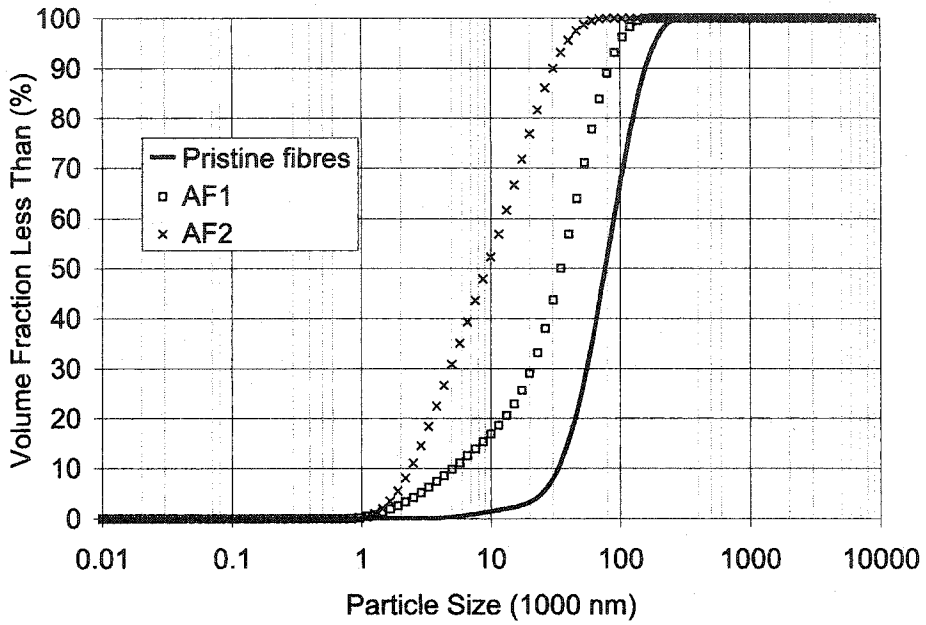

Figure 4.10: Particle size distributions of AF1 and AF2 series.

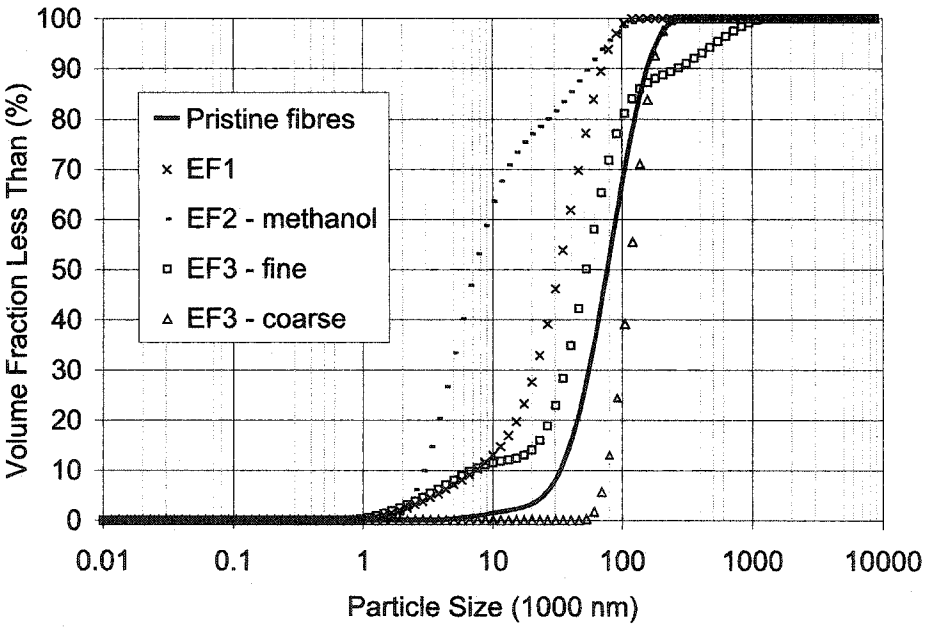

Figure 4.11: Particle size distributions of EF1, EF2, EF3f/c series.

Table 4.2: Summary of shifts in particle size distribution.

Powder	Time (min)	$D_{50}(\mu m)$
Fibre	0	79.4
Sonicate	60	30.2
Settle	60	2.5
Sphere	0	30.2
AF1	0	34.7
AF2	0	9.2
EF1	0	34.7
EF2	0	7.6
EF3f	0	52.5
EF3c	0	120.6

With initial ultrasonic dispersion in water (30 seconds).

4.4 Evaluating Specimen Filler Distribution

4.4.1 Alumina Loading

A macroscopic determination of alumina loading in the epoxy specimens was made using specific gravities. Calculations were made with an assumed overall density of 3500 kg/m^3, based on a 50/50 split between Al_2O_3 and $AlO(OH)$. Due to processing variations, the specimen filler fractions were difficult to regulate and differ from bulk values and between series. The main cause of reduced loading from bulk specimens is the difference in density and resultant settling before gel. The untreated series have W_f's of $< 10\%$ and treated series have W_f's of $< 5\%$. Volume fractions, V_f, for all specimens are $< 3\%$. Table 4.3 summarizes the alumina loadings in the test specimens.

4.4.2 Gradient Determination

Uniform filler distribution within the specimen is central to mechanical property enhancement. Settling prior to gel causes a gradient of filler across the thickness of the cast plate. Through digital analysis of images of the thin specimen cross-sections, the gradient was determined to be minimal across the thickness of the test specimens. Details of this analysis are found in Appendix D.

Table 4.3: Summary of alumina weight and volume fractions.

Specimen	Bulk W_f	Specimen W_f	Specimen V_f
	(%)		
2P	8.45	8.40	2.92
2F	7.55	4.20	1.42
3F	7.29	6.18	2.12
AF1	5.96	2.16	0.72
AF2	6.35	2.88	0.96
EF1	5.71	2.53	0.84
EF2	6.48	2.71	0.91
EF3	6.38	4.26	1.44

Based on an alumina density of 3500 kg/m^3

Two examples are provided to illustrate the gradient. Figure 4.12 shows a cross-sectional view of the cast plate containing EF3coarse fibres. It reveals how settling of the larger clumps leaves almost no alumina in the central region of the plate from which the specimen would be machined. It is the most extreme case of settling; this plate was not usable for testing specimens because of the paucity of alumina remaining in the central (specimen) region. Overlaid is the curve of pixel gray values across the specimen (obtained from digital analysis), revealing the slight gradient and large settled region. Figure 4.13 shows the other extreme; a more uniform dispersion of spherical particles in the 2P series, along with samples from 2F and 3F specimens.

4.4.3 TEM's of Particle Distribution

A more rigorous analysis was made by sectioning specimens along the thickness and taking TEM micrographs of the alumina dispersion. TEM's were taken at the Biological Science's Microscopy Unit, on a Philips/FEI (Morgagni) TEM-CCD. This was done for specimens of 2P, 2F, 3F, as well as AF1, AF2, EF2 and EF3fine series. Representative micrographs are shown in Figure 4.15 and Figure 4.16 for untreated fibres and Figure 4.14 for untreated spheres.

Series 2 and 3 show a wide range of particle sizes, with clumps ranging up to 40μm in length and a profusion of well-dispersed smaller clumps. Large clumps

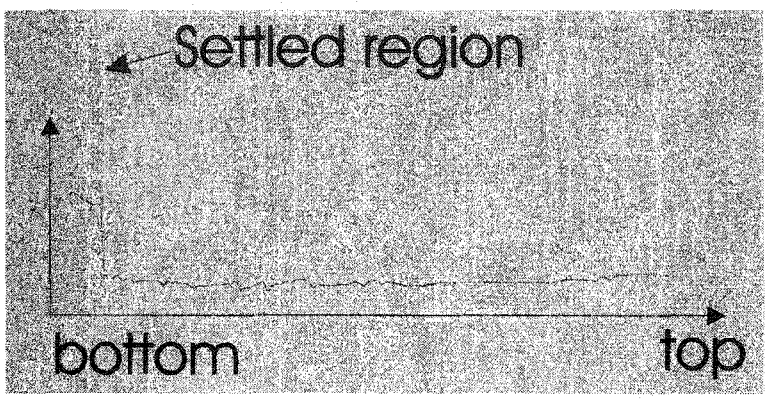

Figure 4.12: Cross sectional view of EF3coarse specimen showing large filler gradient and settled fibre zone.

tend to be circular or slightly elliptical in cross-section.[3] A typical example of these large clumps is taken from series 3F and is shown in Figure 4.17.

Figure 4.18 shows a high magnification view of a smaller clump in series 2F. This clump is representative of medium to small clumps of axially-aligned fibre aggregates. The subregions may be previously aggregated clumps that have flocculated together or simply regions of higher packing factor. Edges of

[3]Lines on the micrographs represent thickness variations caused by the glass microtome knife. The average sample thickness was $\sim$ 45nm. Also, stick-slip cutting through the stiff clumps caused clumps to tear along lines of weakness.

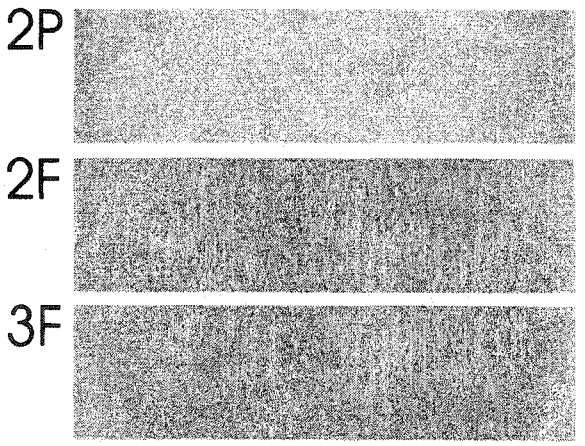

Figure 4.13: Cross sectional view of 2P specimen showing little filler gradient; also shown are series 2F and 3F. Bottom of plates to the right.

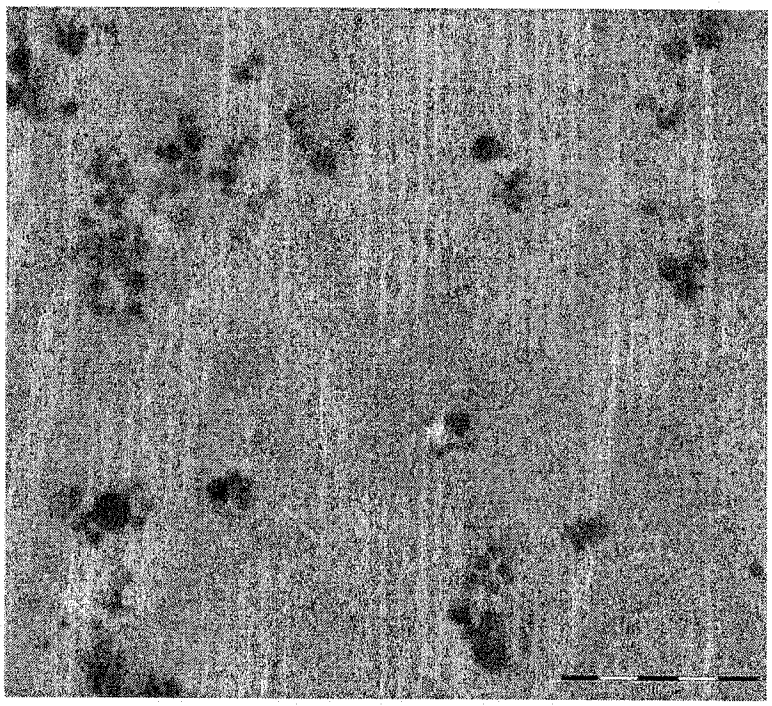

Figure 4.14: TEM image of particle distribution in series 2P, showing small and void-containing clumps of spheres. Magnification = 14k; full bar = $1\mu m$.

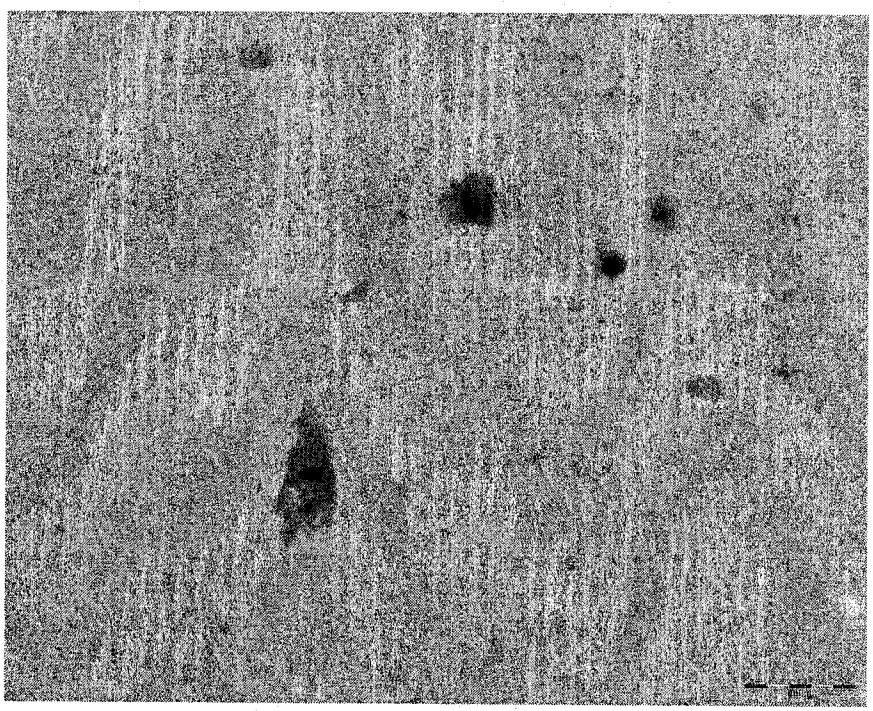

Figure 4.15: TEM image of particle distribution in series 2F.
Magnification = 11k; full bar = $1\mu m$.

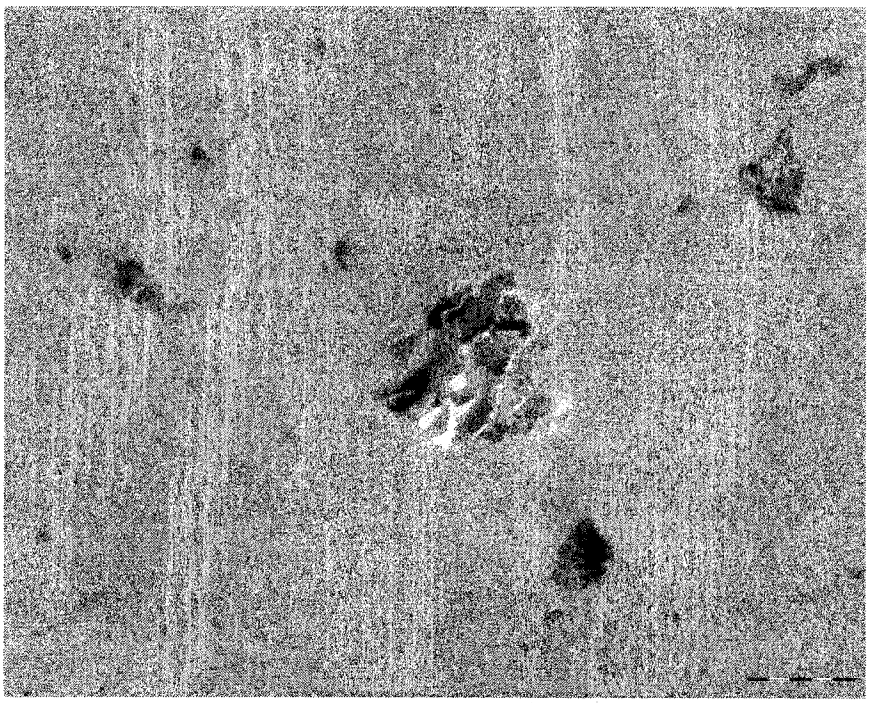

Figure 4.16: TEM image of particle distribution in series 3F.
Magnification = 22k; full bar = $500nm$.

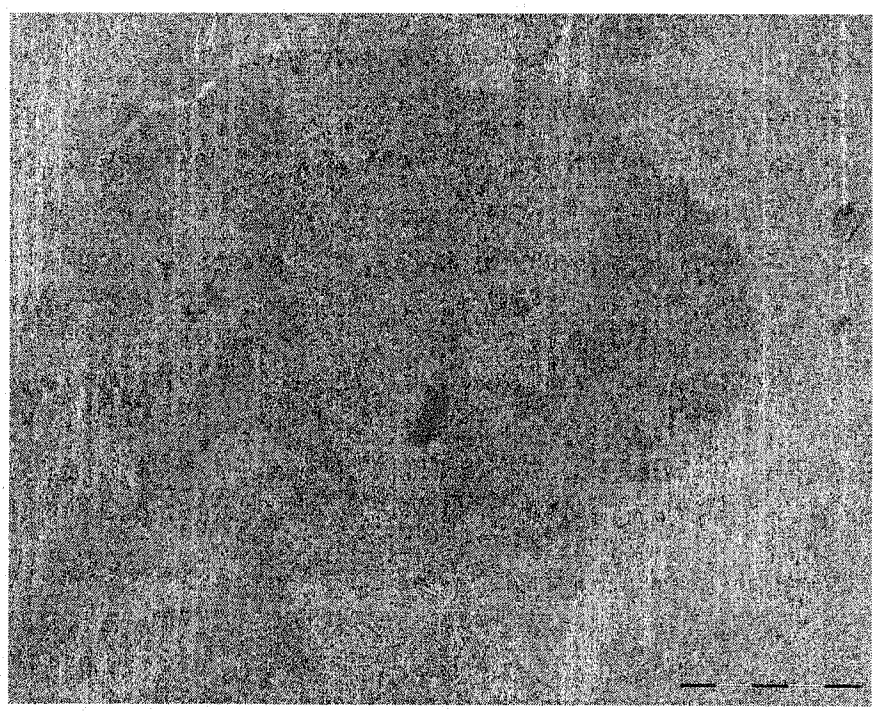

Figure 4.17: TEM image of a large clump in series 3F.
Magnification = 3.5k; full bar = $5\mu m$.

these clumps are fairly smooth and not generally diffuse.

The silane-treated specimens, shown in Figure 4.19 and Figure 4.20, reveal larger, less circular clumps and fewer, well-dispersed and smaller clumps. The clumps appear to be composed of individual fibres and aggregates surrounded by regions of non-matrix material, i.e. a polysiloxane region. The surface treatment has apparently caused adherence of fibres within a polysiloxane matrix; forming a larger, hybrid clump. An extreme example of this is the hybrid clump shown in Figure 4.21, from series EF2. High magnification views of clumps in the treated powder series, as in Figure 4.22 evidence a more diffuse boundary, with "finger-like" fibres protruding into the surrounding material.

An exception to the silane treated distribution is found in series AF2. Figure 4.23 reveals a combination of distributed fibres and larger, though still small and tightly packed, aggregates of fibres. The presence of a wider reinforcing distribution is shown in more detail in Figure 4.24, where the diffuse nature of the siloxane coating is also revealed. This coating represents a broadening of the interphase region between alumina and epoxy.

Figure 4.18: Typical particle clump in series 2F - high magnification. Magnification = 36k; full bar = $500nm$.

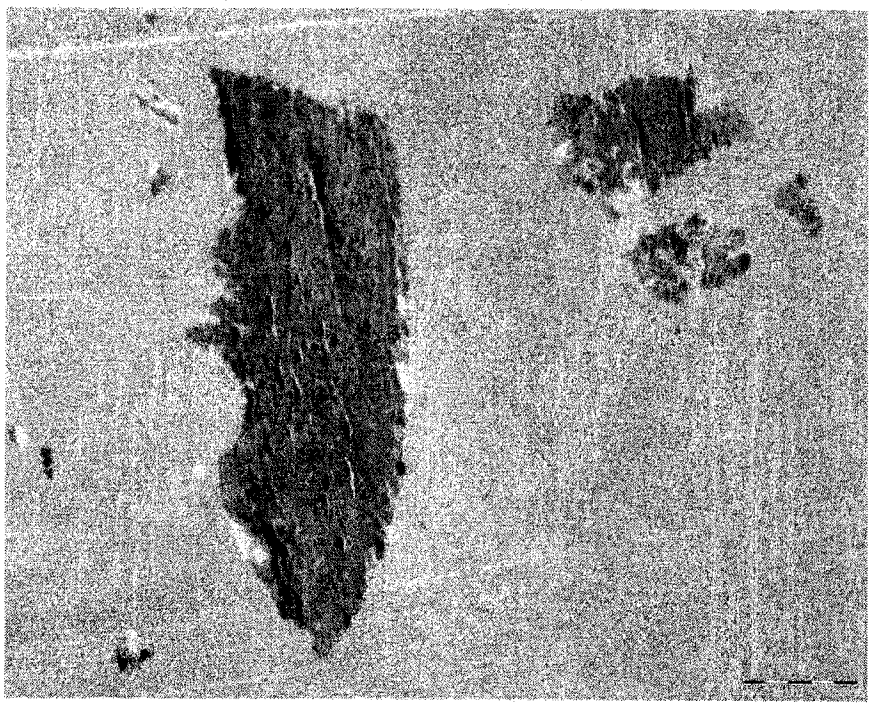

Figure 4.19: TEM image of particle distribution in series AF1. Magnification = 2.2k; full bar = $5\mu m$.

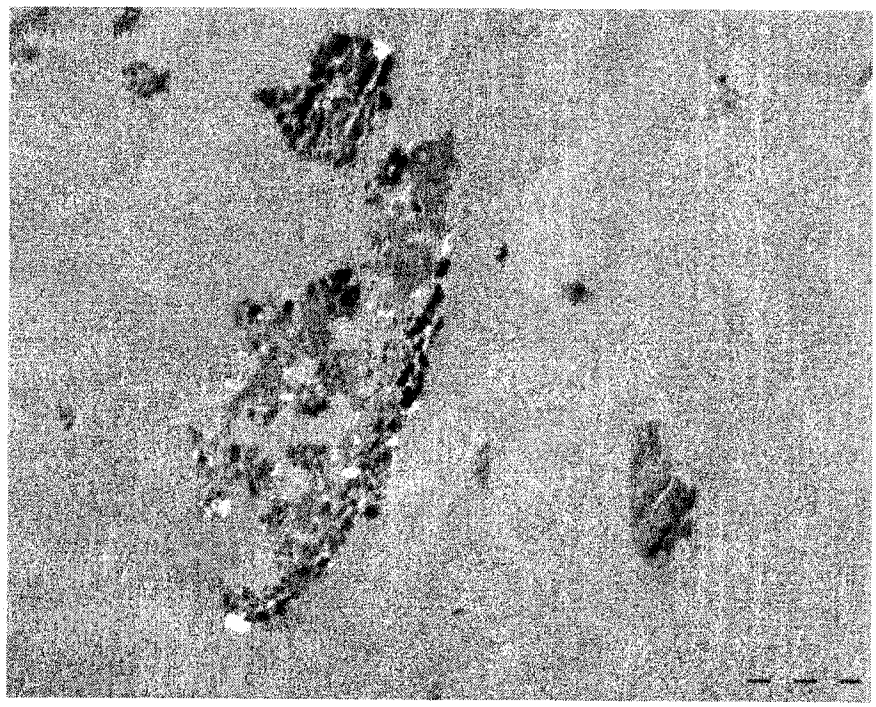

Figure 4.20: TEM image of particle distribution in series EF2. Magnification = 2.2k; full bar = $5\mu m$.

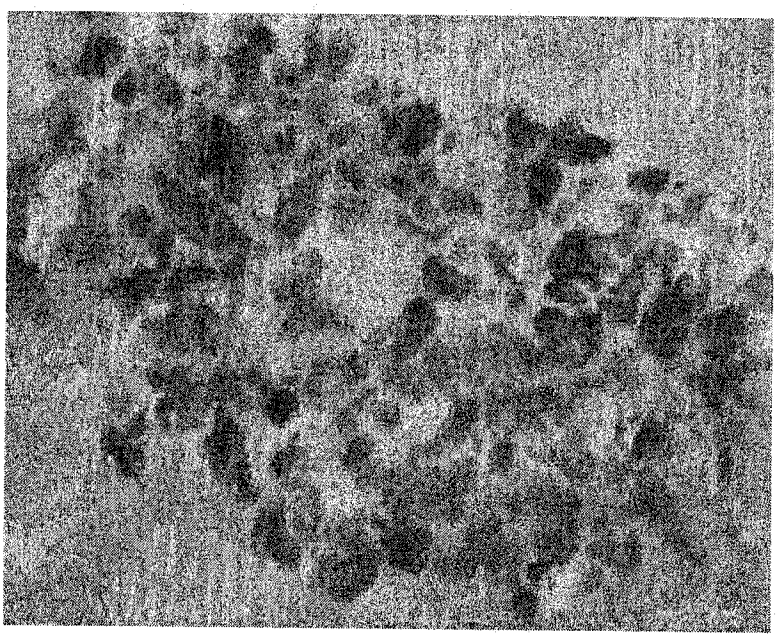

Figure 4.21: Hybrid polysiloxane/alumina fibre clump in series EF2. Note dense aggregates and the contiguous material around them.
Magnification = 7.1k; full bar = $2\mu m$.

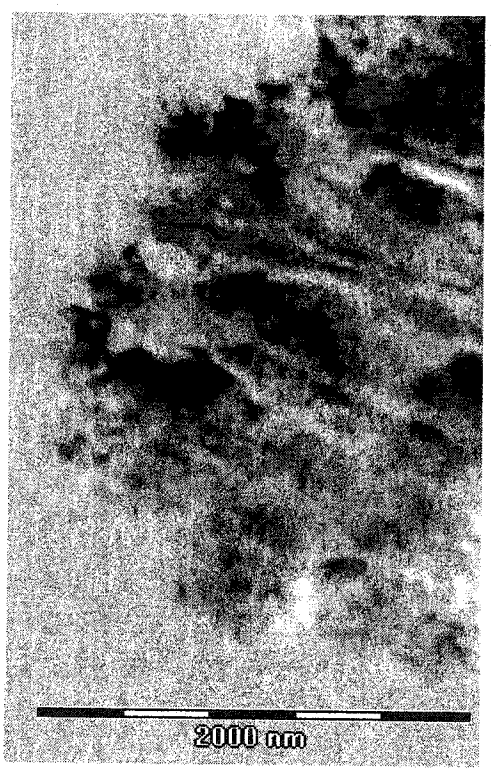

Figure 4.22: Diffuse boundary of fibre clump in series AF1.
Magnification = 5.6k; full bar = $2\mu m$.

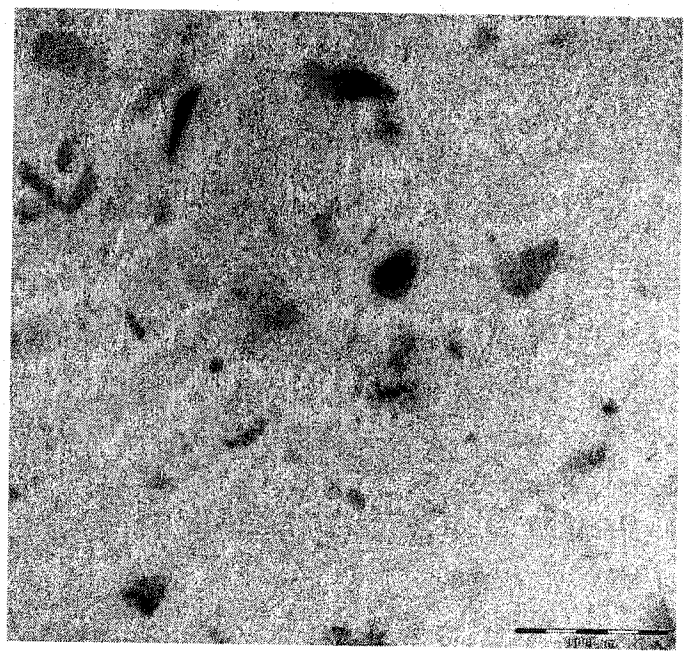

Figure 4.23: Small aggregates and distributed fibres in series AF2. Magnification = 11k; full bar = $1\mu m$.

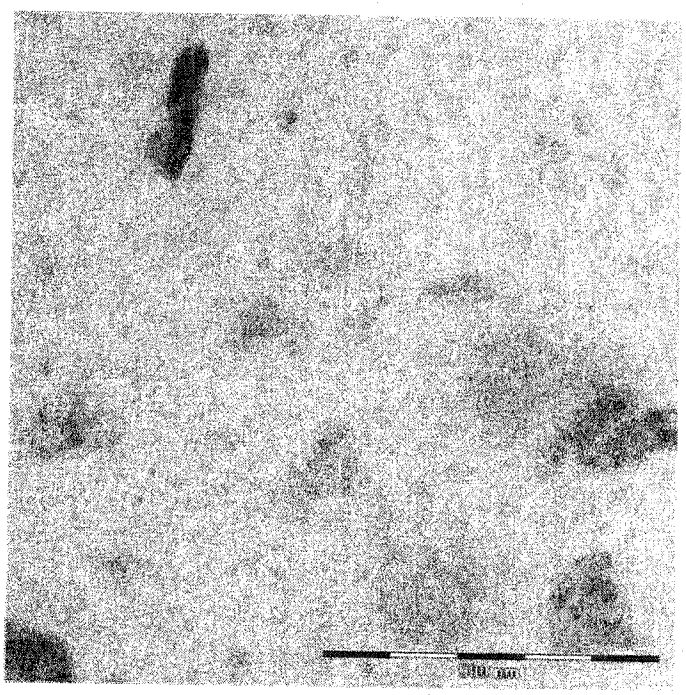

Figure 4.24: Detail of siloxane coated clumps and fibres in series AF2, revealing similarities to both untreated fibre and other treated fibre series. Magnification = 36k; full bar = 500 nm.

4.4.4 Digital Analysis and Quantification

Quantification of particle dispersion in the specimens was made by digitizing the TEM images and performing a 'blob' analysis of clumps, using the program Matrox Inspector. Details of the technique used are provided in the Appendix C. This analysis allows clump size to be calculated from particle pixel area. This is a powerful tool which is coming into vogue in nanoparticle and composite analysis, especially in the area of thin films and colloids[51, 79, 26].

To obtain more accurate results, particle clump size was limited to the region between the largest clumps and taken at lower magnifications.[4] Only this intermediate range is presented in the particle distributions. At least two images of similar magnification were analyzed for each specimen. Three histograms of series 3F particle size distributions are shown in Figure 4.25, for micrographs at 8.9K and 14K magnifications. In this we see that even between the very large clumps ($\sim 30\mu m$) there is a broad range of particle and clump sizes. Though the number of small clumps is great, in terms of volume of fibres the majority of particles are in larger clumps. This distribution is contrasted in Figure 4.26, showing the paucity of clumps between large clumps and the relatively flat overall distribution of the EF2 series. In this case, histograms are of micrographs taken at 2.2K, meaning that fewer small particles should be seen because of the low resolution, though a shift towards smaller clumps should still be seen. In its absence is the knowledge that silane treatment has not provided an enhanced distribution of alumina within the test specimens.

[4]Digital analysis is highly dependent on magnification, contrast between background and foreground and image processing[51]. Magnifications low enough to include the largest clumps make the resolution too poor for small clumps to be seen. Conversely, too high a magnification does not allow enough (or large enough) clumps to be included.

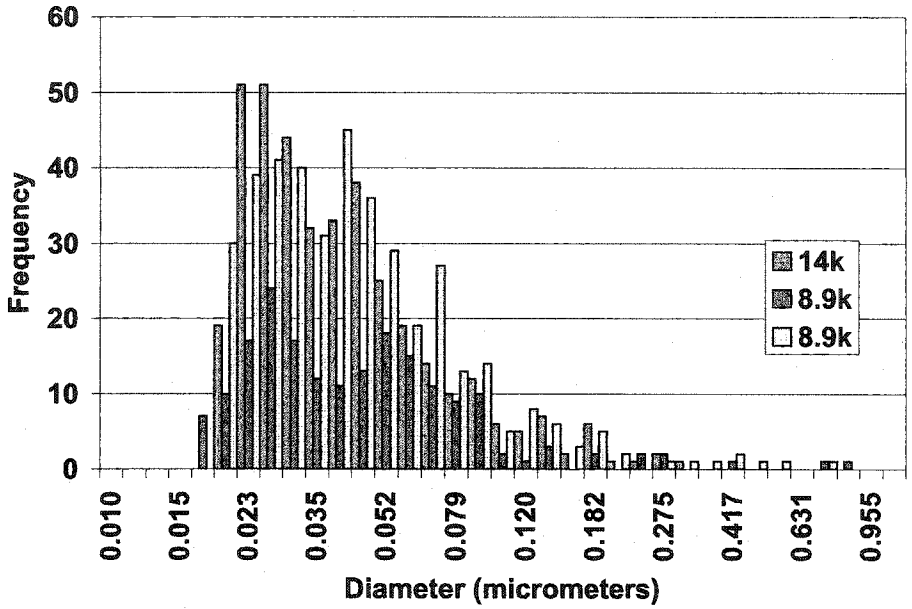

Figure 4.25: Histograms of particle size distribution for 3F TEM's.

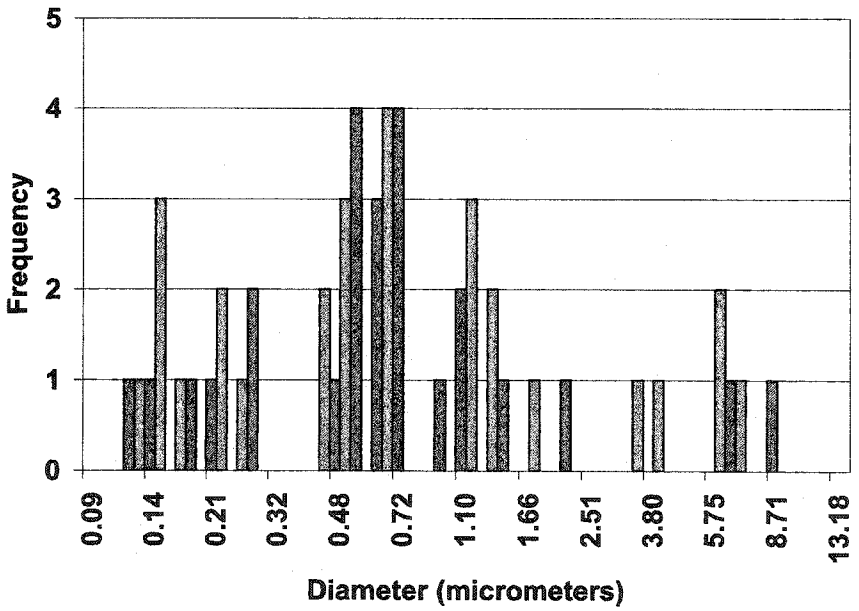

Figure 4.26: Histograms of particle size distribution for EF2 TEM's. Both at 2.2k.

4.5 Tensile Testing

Monotonic tensile tests were conducted for all series, with a minimum of three specimens tested for each series.[5] Stress is calculated based on original specimen cross-sections (engineering stress). A correction is used to account for the changing width between the extensometer teeth. This is a geometric correction using the average width between the extensometer knifes and the center of the specimen.[6] Strain was taken directly from the extensometer; calibrated to 10% and evidencing a linear response up to 15%.

Series 1 testing was conducted to calibrate testing procedures and standardization of test methodology; results are not presented here. (Refer to Appendix G for results.) This testing determined that:

- use of an extensometer for strain measurement was not detrimental to failure strain values, though failure resulted at the knife edges.
- the loading rate of 4.5N/s provided a highly nonlinear response and a higher loading rate was desirable for a more linear initial region.
- cloth patches could protect the specimen edges from early damage from the extensometer knives.
- specimens are sensitive to end-tab bonding.

The tensile stress-strain response is shown for each series: 2F, 2P, 3F in Figure 4.27, Epoxy, AS, ES in Figure 4.28, AF1-2 in Figure 4.29 and EF1-3 in Figure 4.30.[7] Elastic moduli were calculated from the slope of the linear best fit line through the data to 1% strain. A table of the elastic moduli, failure stress and failure strain for every specimen is found in Appendix F (aside from series 1 specimens). An average of the moduli, failure strain, and failure stress values for each series is summarized below in Table 4.4.

[5]Except for series 3F, where only 2 tests were conducted, owing to premature specimen failure.

[6]The difference in area using either of the widths is less than 0.5%.

[7]These values did not take into account specimens failing at the end-tabs; strain values, sensitive to yielding at the end of the cast, or only included if within 25% of the highest value in each series.

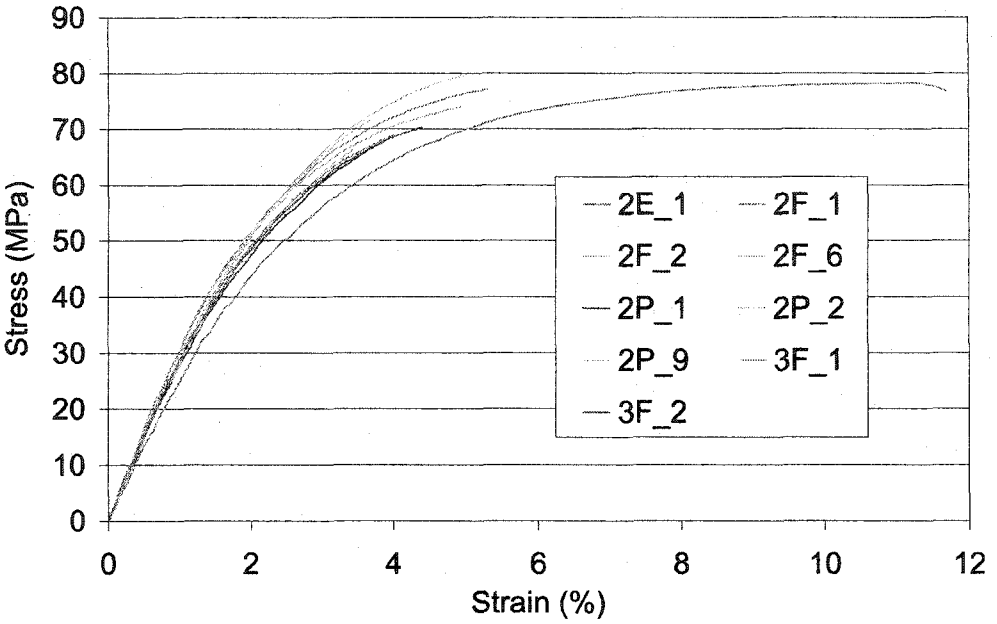

Figure 4.27: Stress-strain response of Series 2 and 3 nanocomposites.

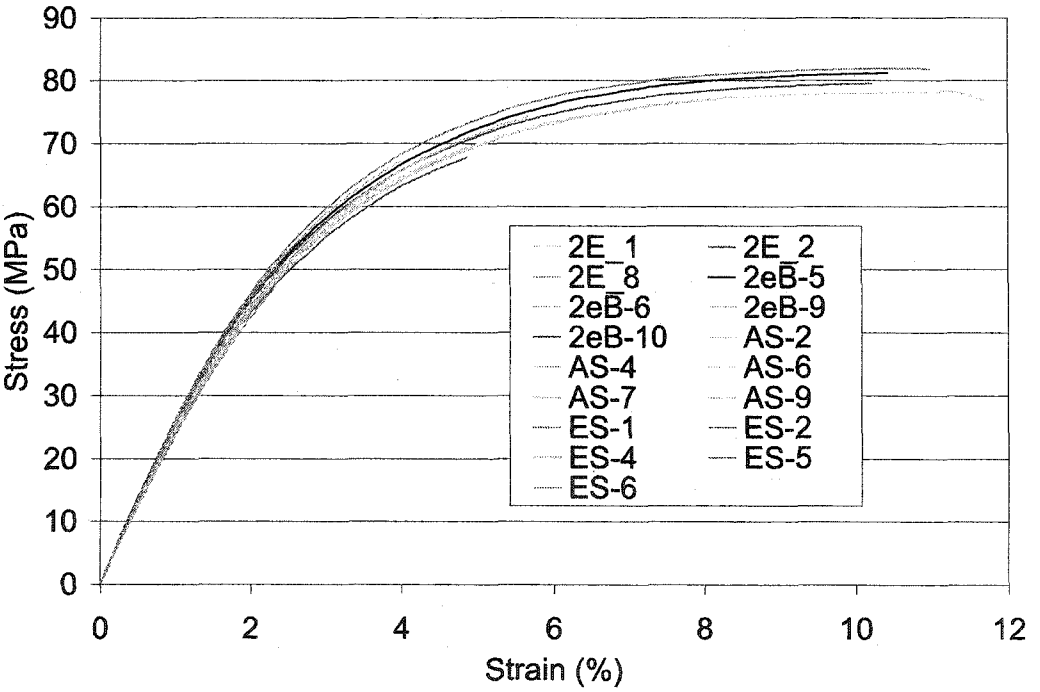

Figure 4.28: Stress-strain response of ES, AS and epoxy specimens.

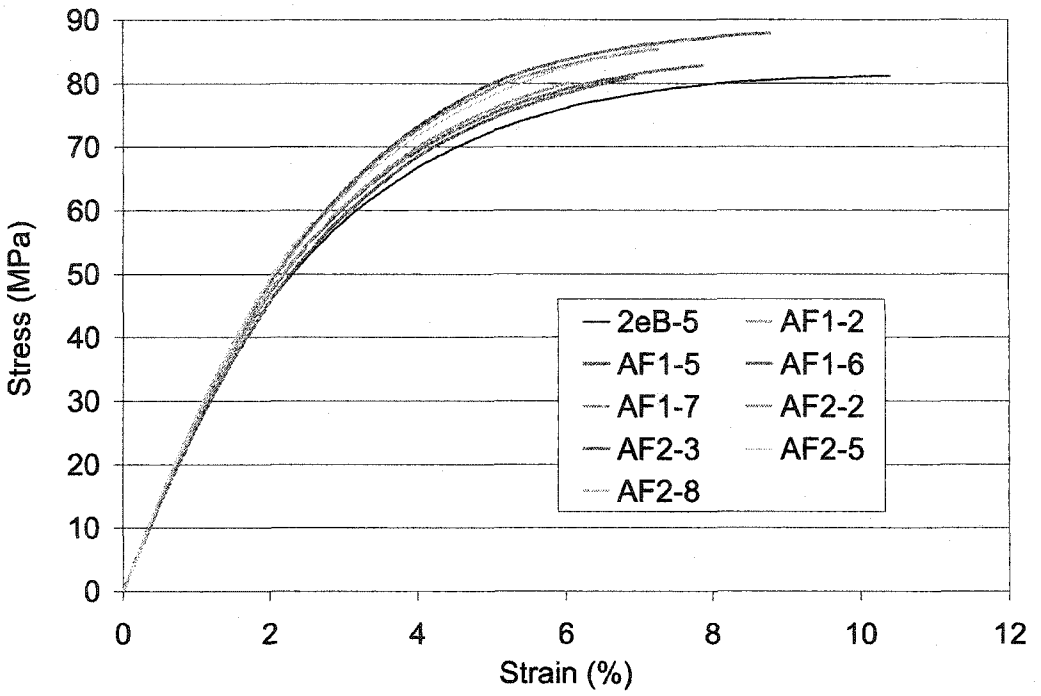

Figure 4.29: Stress-strain response of AF1 and AF2 specimens.

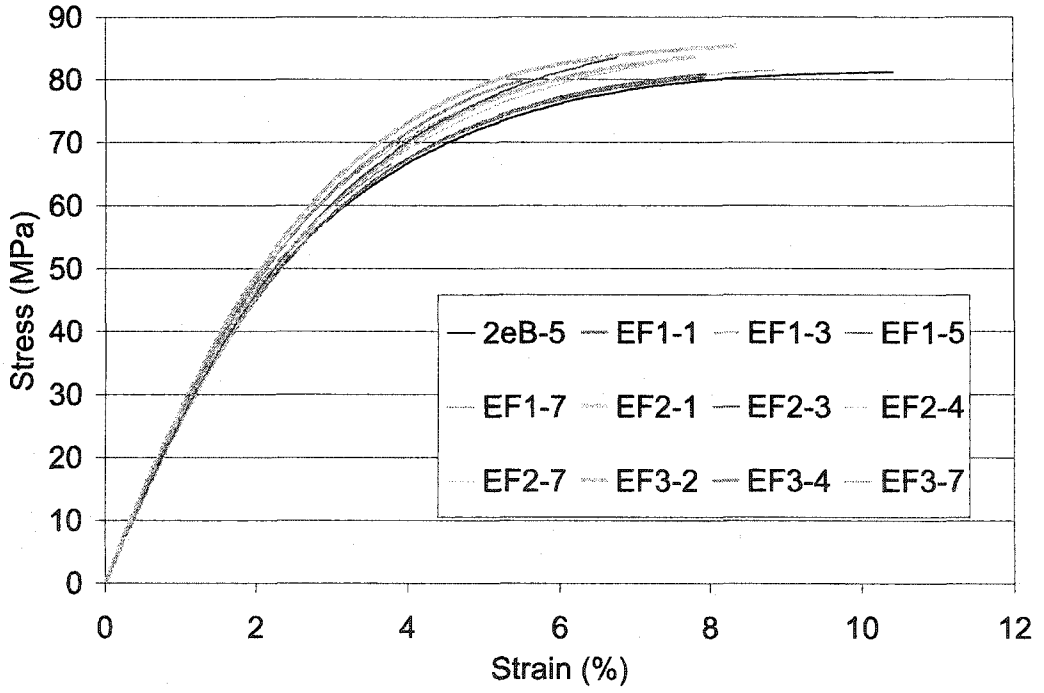

Figure 4.30: Stress-strain response of EF1, EF2 and EF3 specimens.

Table 4.4: Summary of tensile properties.

Series	W_f	E (GPa)	ϵ_f (%)	σ_f (MPa)
Epoxy	x	2.57	10.67	77.99
2P	8.40	2.92	3.80	68.68
2F	4.20	3.07	5.09	76.81
3F	6.18	2.96	4.22	69.66
AS	x	2.54	8.74	76.31
ES	x	2.60	11.00	81.8
AF1	2.16	2.71	6.98	81.34
AF2	2.88	2.79	7.94	86.72
EF1	2.53	2.74	8.26	84.24
EF2	2.71	2.70	7.01	82.50
EF3	4.26	2.81	6.95	80.09

4.6 Compression Testing

A graph of the compressive stress-strain response for pristine-fibre nanocomposite specimens is shown in Figure 4.31. The response is very linear until $\sim 2-4\%$, when buckling commences. The elastic moduli for compression tests are calculated as for the tensile tests, though only the first 0.25% strain is used. As a result of the nonlinear response, use of this lower strain region to determine modulus provides for slightly higher values than in the tensile case. The compressive moduli are provided in Table 4.5.

Table 4.5: Summary of compressive properties.

Series	W_f (%)	Modulus (GPa)	$E/E_{tensile}$
Epoxy	X	2.61	1.02
2P	8.40	2.95	1.01
2F	4.20	3.03	0.99
3F	6.18	3.08	1.04

Continuity of modulus is found in Figure 4.32, where the curve for a series 2E specimen is shown to be smooth and linear through the origin.

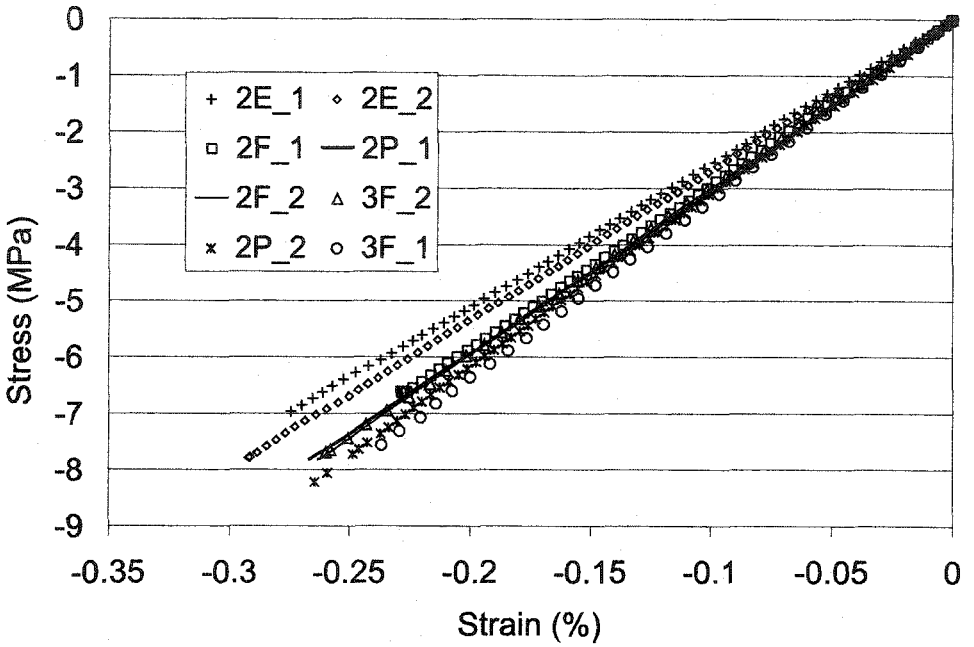

Figure 4.31: Compressive stress-strain response of pristine-fibre nanocomposites.

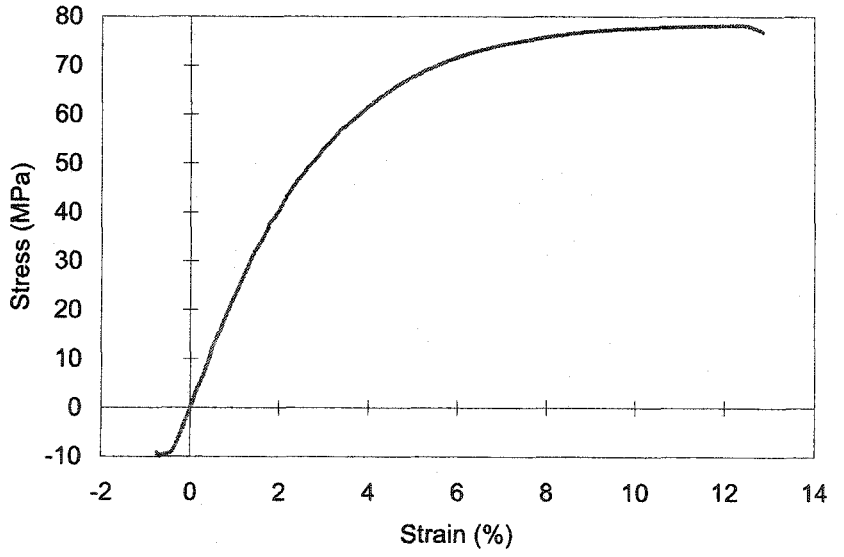

Figure 4.32: Combined tension-compression stress-strain response for a 2E specimen.

4.7 Fracture Testing

Examples of fracture testing load-displacement curves are found below: Figure 4.33 shows load-displacement curves from several untreated fibre series and Figure 4.34 shows some load-displacement curves from treated fibre series. Appendix E presents the load-displacement curves for all tests, separated into series.

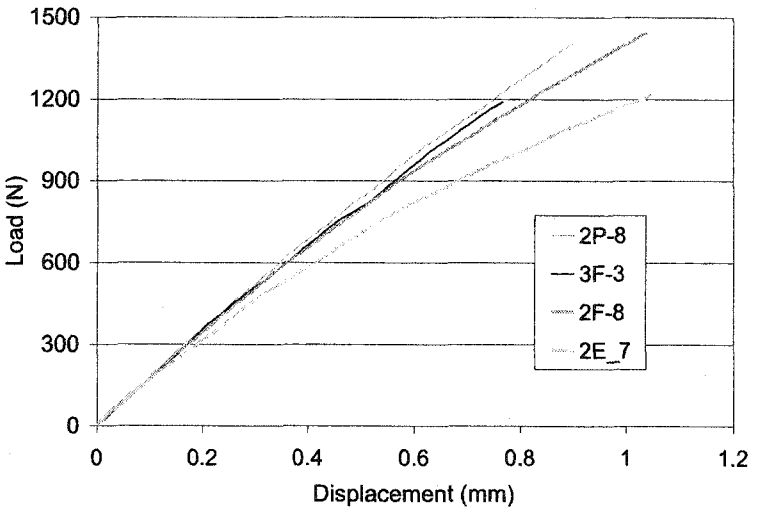

Figure 4.33: Fracture load-displacement curves for 2E, 2P, and 2-3F specimens.

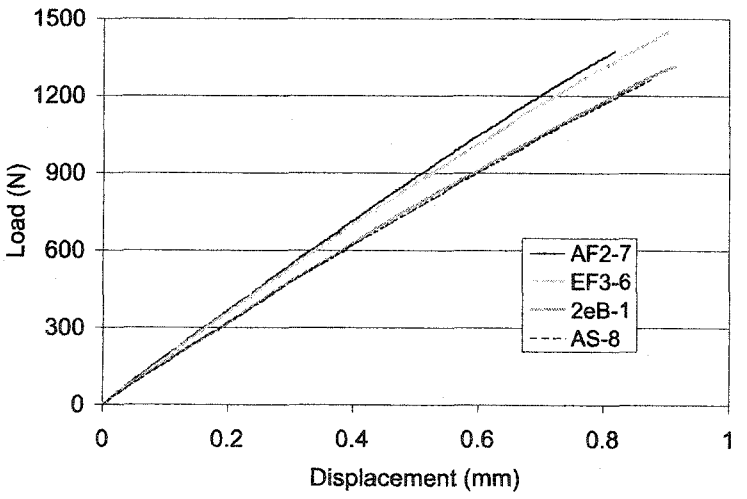

Figure 4.34: Fracture load-displacement curves for treated fibre series.

A summary of the pre-crack lengths and failure loads for all of the fracture tests is provided in Table 4.6.

Table 4.6: Summary of fracture results.

Epoxy	Specimen	2E-4	2E-5	2E-6	2E-7	
	Crack Length (mm)	0.766	1.007	1.053	0.885	
	Failure Load (N)	1269	1108	1149	1216	
	Specimen	2EB-1	2EB-2	2EB-3	2EB-4	
	Crack Length (mm)	0.720	1.165	1.175	1.325	
	Failure Load (N)	1332	1203	1089	1095	
2P	Specimen	2P-4	2P-5	2P-6	2P-7	2P-8
	Crack Length (mm)	0.717	1.007	0.991	1.152	0.727
	Failure Load (N)	1345	1194	1268	1198	1427
2F	Specimen	2F-3	2F-4	2F-5	2F-7	2F-8
	Crack Length (mm)	0.885	0.976	1.307	0.747	0.812
	Failure Load (N)	1223	1268	1194	1203	1463
3F	Specimen	3F-3	3F-4	3F-5	3F-6	
	Crack Length (mm)	0.915	0.885	1.038	0.820	
	Failure Load (N)	1269	1146	1126	670	
AS	Specimen	AS-1	AS-3	AS-8	AS-10	
	Crack Length (mm)	0.687	1.081	0.658	1.067	
	Failure Load (N)	998	1179	1268	1278	
ES	Specimen	ES-3	ES-7	ES-8	ES-9	ES-10
	Crack Length (mm)	1.105	0.853	1.147	0.540	1.269
	Failure Load (N)	1121	1365	1301	1375	1234
AF1	Specimen	AF1-1	AF1-3	AF1-4	AF1-8	AF1-10
	Crack Length (mm)	0.616	1.166	1.152	0.732	1.316
	Failure Load (N)	1170	1388	1142	1416	1113
AF2	Specimen	AF2-1	AF2-4	AF2-6	AF2-7	AF2-9
	Crack Length (mm)	0.631	0.732	1.067	1.119	1.011
	Failure Load (N)	1102	1317	1064	1378	1289
EF1	Specimen	EF1-2	EF1-4	EF1-6	EF1-8	EF1-9
	Crack Length (mm)	0.717	1.316	1.147	0.656	0.959
	Failure Load (N)	1301	1195	1161	1416	1255
EF2	Specimen	EF2-2	EF2-5	EF2-6	EF2-8	
	Crack Length (mm)	0.732	0.534	1.175	1.128	
	Failure Load (N)	1336	1372	1220	1109	
EF3	Specimen	EF3-1	EF3-3	EF3-5	EF3-6	
	Crack Length (mm)	0.766	1.147	1.152	0.686	
	Failure Load (N)	1360	1109	1166	1451	

Chapter 5

Discussion

5.1 Specimen Particle Distribution

Particle distribution is seen (using SEM's and TEM's) to be consistent across the thickness of the specimens. Sections scanned and analyzed digitally reveal only minor gradients from settling. Although somewhat dichotomous, it can be said that there is uniform inhomogeneity. No series has uniformly dispersed alumina, although 2P spheres are most effectively dispersed. This is shown in Figure 5.1.

The distribution can be attributed to a lower initial clump size, a lower particle surface area and weaker attractive particle-particle, forces. All non-reinforced series have similar fracture surfaces and appear equally transparent.

Series 2F TEM's show extensive, well distributed clumps, with interspersed larger clumps of up to $30\mu m$ in diameter. Digital analysis reveals that the D_{50} of the clumps within the specimens (between large clumps) to be $0.075\mu m$, with clumps larger than $\sim 1\mu$m constituting $< 0.25\%$ of the number of clumps, though $> 85\%$ of the clump area. The clumps evidence stronger and closer inter-particle associations (dense, aligned fibres) with larger clumps including occasional small, dense regions, as seen in Figure 4.21. Boundaries between regions of close-packing form potential weaknesses in the larger clumps; the smaller clumps' strength should be higher than that of the large clumps (floccs) or hybrid clumps (aggregates of smaller clumps).

Series 3F TEM's reveal similar behavior, though there are very large ($> 50\mu m$) clumps of apparently flocculated fibres (weakly bonded). The extremes

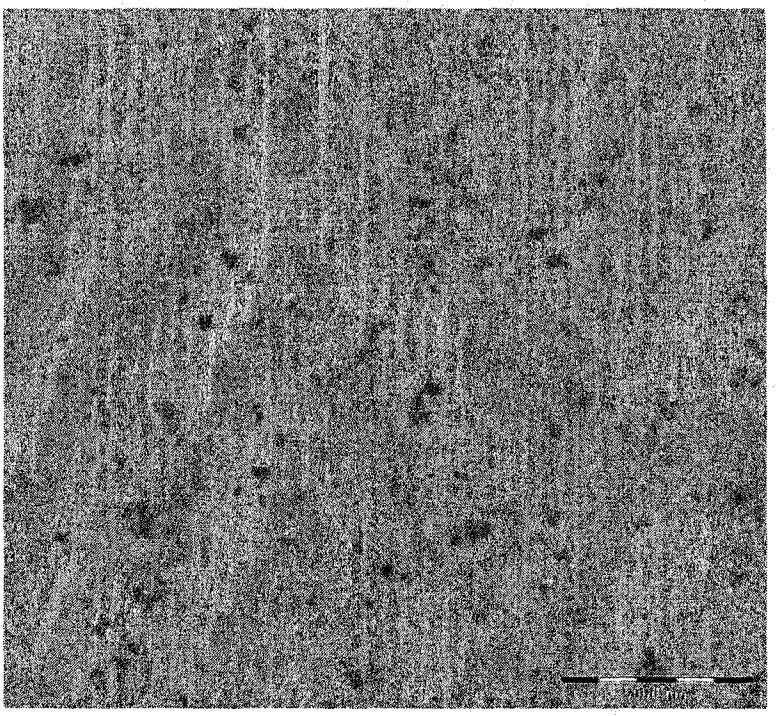

Figure 5.1: Distribution of 2P spheres evidencing increased uniformity. Magnification = 2.2k; full bar = $5\mu m$.

of series 3F are illustrated in Figure 5.2 where two small aggregates of clumps lie beside and within a larger, loosely packed clump. For the clump distribution between large clumps, digital analysis reveals a D_{50} of $\sim 0.050\mu m$, with clumps larger than $\sim 1\mu$m constituting $< 0.1\%$ of the total number of clumps ($> 95\%$ of area). As well, despite the loosely bound nature of particles in large floccs (which could allow greater penetration of matrix and enhanced particle wetting), the smooth boundary between clump and matrix is perhaps a weakness in the composite system. Credence is lent to this in Figure 4.17, where microtoming has pulled the matrix away from the top of the clump. This is seen less often in hybrid clumps, where the major weakness appears to be inter-aggregate bonds. It is not seen as frequently for smaller clumps, whose boundaries appear to be more diffuse.

Micrographs of series 2 and 3 show that mixing has produced a fairly well-dispersed fraction of fibres. Histograms of particle distribution reflect this, with a large fraction of fine particles in evidence. However, the large floccs

reveal a phase segregation within the liquid polymer. Small, densely packed clumps also show that dry agglomerates are retained from before mixing, with poor penetration of the matrix into the agglomerates during wetting. Although settling of clumps (and fibres) reduced the fibre fraction, increased pre-gel mixing of series 3 fibres, following addition of the second epoxy component, may have promoted the retention (and perhaps the creation) of potentially defective flocculates. Filler fraction has been increased at the expense of the quality of filler dispersion.

Silane treated fibres series TEM's (AF1, EF2, EF3) all evidence less uniform dispersion of fibres. Large clumps do not appear to be flocculations, but the aggregates of smaller clumps of higher packing factors. Moreover, these large clumps appear to be tertiary or hybrid clumps with a cohesiveness obtained from the polysiloxane covering of small aggregates. As seen in Figure 4.19 or Figure 4.20, microtoming has not caused extensive separation within the clump (as per series 2 aggregates) or between clump and matrix (as seen in series 3 floccs). For AF1 series analysis, clumps larger than 1μm constitute $> 12\%$ of the total number of clumps and $> 95\%$ of the clump area.

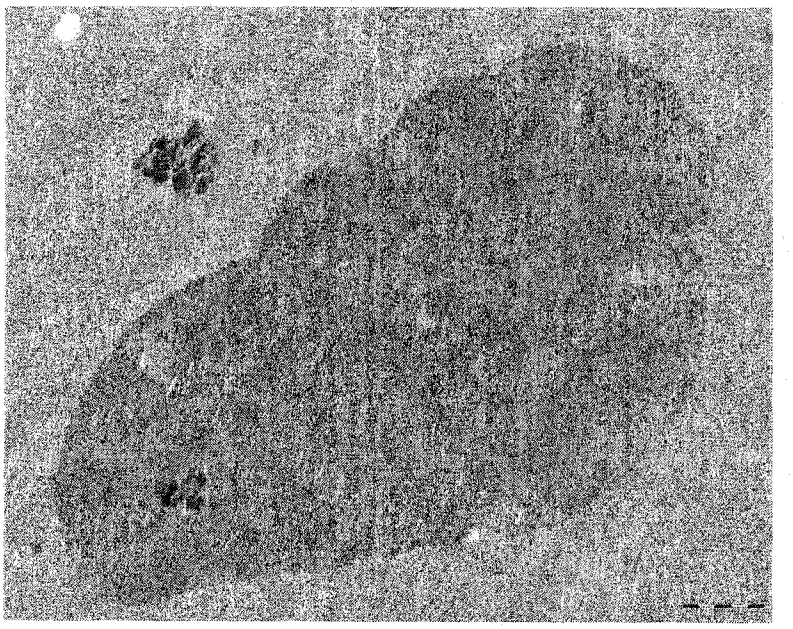

Figure 5.2: Floccs and aggregates in series 3F reveal clumping extremes. Magnification = 4.4k; full bar = $2\mu m$.

This is readily appearent when comparing the histograms of Appendix C, the TEM's shown in Section 4 or below, in Figure 5.3.

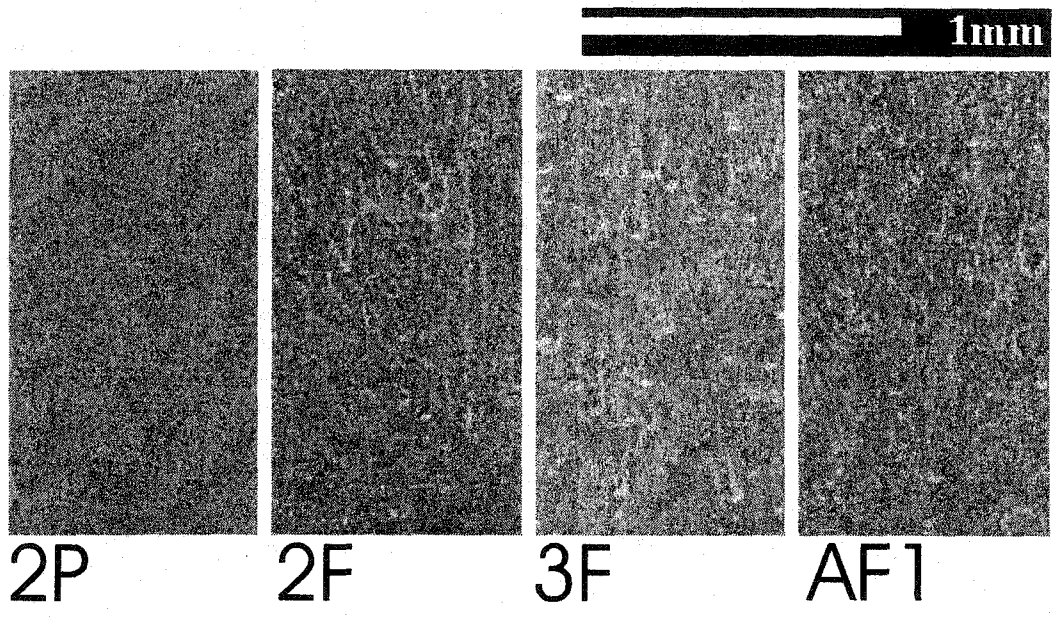

Figure 5.3: Comparison of clumps from SEM's of fracture surfaces. White regions are clumps.

It is difficult to determine if a very well dispersed phase exists in the treated fibre series. It is possible that mixing has caused mono dispersed fibres that cannot be seen, though most evidence points to aggregation of small clumps into larger, hybrid clumps. The drying of treated fibres is perhaps the cause of this, for the drying process allows networking of silane between treated clumps and fibres, solidifying into polysiloxane networks and stronger clumps of larger size. This can be seen as a liquid bridging akin to salt bridging in hydrated (pristine) oxide powders, which form strong clumps. Moreover, dry agglomeration processes can occur in the treated fibre powders, in the period following drying and before incorporation with the matrix.

5.2 Fracture Mechanisms

The fracture surfaces of the nanocomposite specimens provide great insight into the nature of reinforcing of the epoxy matrix. Though these mechanisms

are for monotonic loading (a single cycle), they are indicative of general loading mechanisms.

Before continuing it should perhaps be reiterated that the specimens tested here deviate from the ASTM tensile and fracture standards to alleviate the problems of settling gradients present in thicker specimens and to allow multiple tests to be conducted using one specimen type. The implication of this is that a state of plane stress, not strain, exists in the specimen during loading. Resultantly, a large plastic region exists and the possible impact of edge effects is greater. Though the fracture is assumed to be mainly mode 1, from onset the fracture includes other modes. Despite this, it is emphasized that the aim of this experimentation has been the comparison of the mechanical response of nanocomposites to neat epoxy specimens of the same geometry. Comparison of the values obtained here (particularly for fracture tests), with those of other sources may not necessarily be valid.

Before the fracture values are discussed, though, the mechanisms operating in the nanocomposites are gleaned from SEM fracture micrographs. The fracture surfaces all evidence similar macroscopic features: 1) a rough, stick-slip region of razor blade penetration; 2) a short region of sharp cracking, accompanied by crack arrest lines in the matrix, denoting the extent of this "process" type zone of initial deformation; 3) initiation of fracture under monotonic loading, typically commencing anew from a defect or cluster of agglomerates at the boundary of the sharp-crack zone; 4) propagation of the crack front out to the sides and along the width of the specimen, leaving a smooth, 'mirror-like' zone; and 5) a region of extensive damage involved with fast fracture, along with mixed-mode tearing and feathering, as ligature failure and bending come into play. An example of this is shown in Figure 5.4, where the above features are numbered, with Figure 5.5 providing detail of the pre-crack region. Interpretation of mechanisms is limited to regions 2-4, where the most straightforward analysis can be made.

A general comparison of fracture surfaces for the different series is given in Figure 5.6, all from region '4' of the fracture surfaces. More detailed descriptions are provided below.

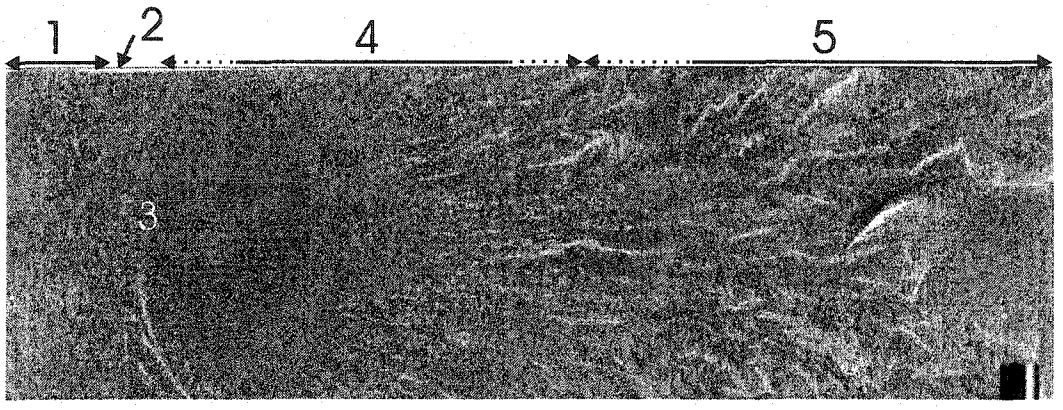

Figure 5.4: General features of the fracture surface; taken from series 2E.

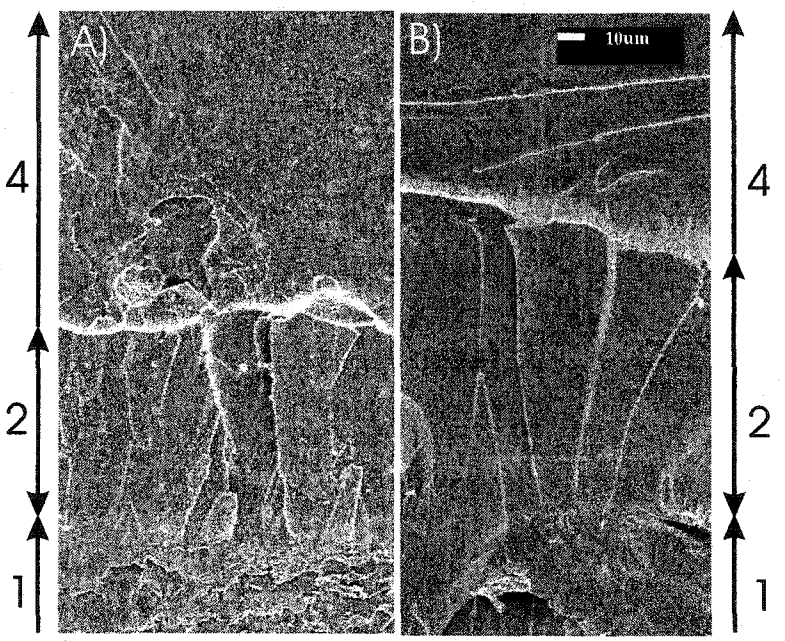

Figure 5.5: Detail of the pre-crack and sharp-crack region of fracture specimens. 'A' is from series 2F and 'B' is from series 2E. Full bar = $10\mu m$.

Unreinforced series show large mirror regions, with river-like ridges in the direction of fracture (Figure 5.7), that coalesce into the larger tears of region '5'. As the crack front moves from fracture origin to the sides of the specimen, a fan-like pattern forms from these ridges (seen above in Figure 5.4).

Spherical particles are seen throughout 2P specimens, resulting in a rough surface; though flaky (Figure 5.8)and with a profusion of void-like holes and poor wetting (Figure 5.9). Larger clumps appear to be weak, though with an

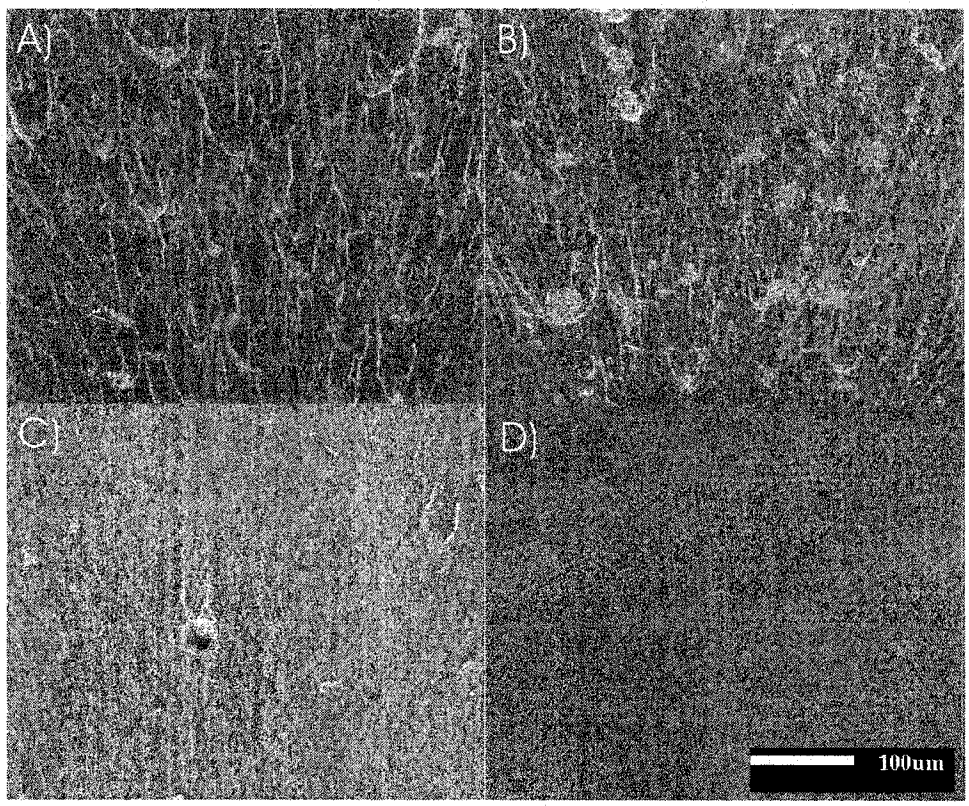

Figure 5.6: A general comparison of fracture surfaces from tested specimens. 'A' is from series AF2, 'B' is from series 3F, 'C' is from series 2P and 'D' is from series ES. Full bar = $100\mu m$.

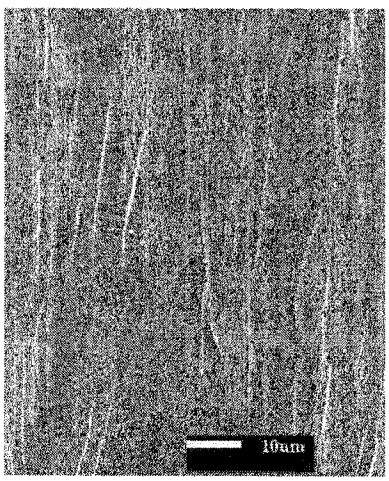

Figure 5.7: River-like ridges in the direction of fracture; neat epoxy. Full bar = $10\mu m$.

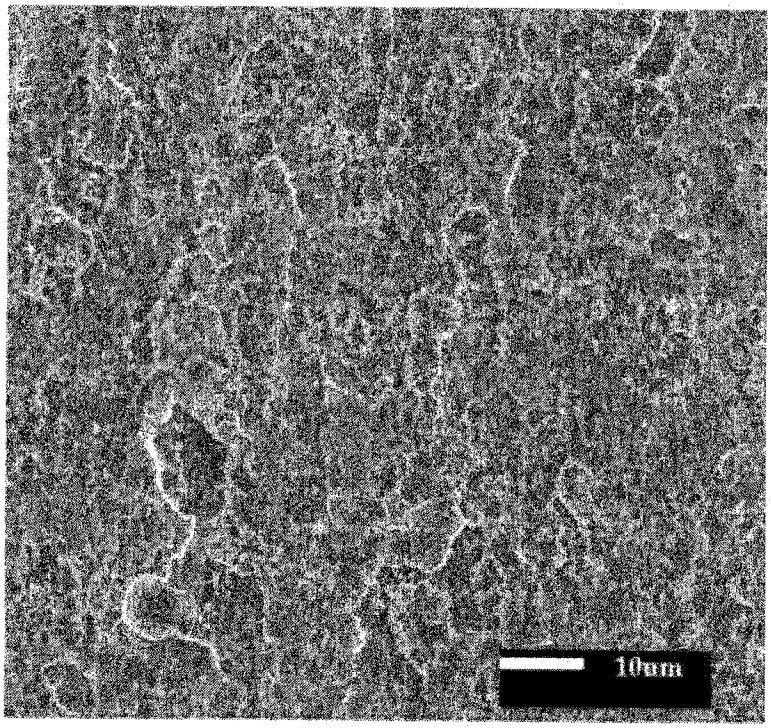

Figure 5.8: Flaky surface of series 2P. Full bar = $10\mu m$.

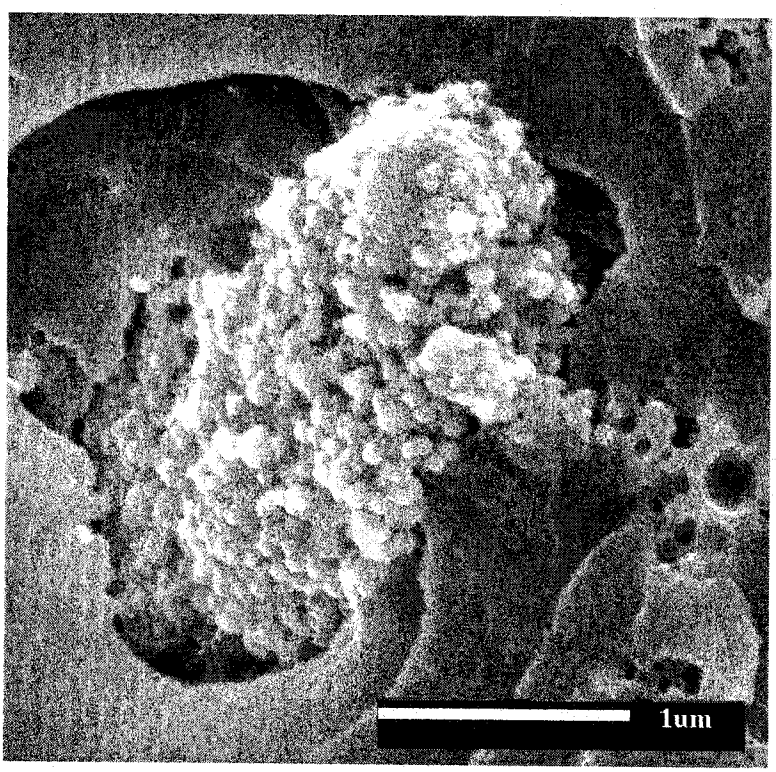

Figure 5.9: Poor wetting and void-like clumps of series 2P. Full bar = $1\mu m$.

occasional strong clump that has debonded and forced the crack front around it rather than through it. Many small de-bonded, single particles are seen; one specimen evidences a $50\mu m$ single sphere still embedded. Large clumps show some pinning mechanisms. This is seen in Figure 5.10

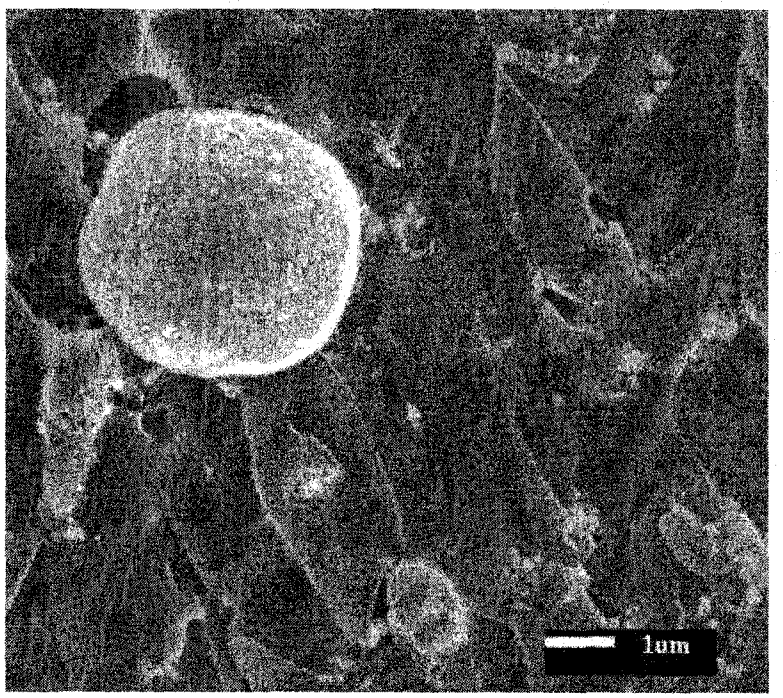

Figure 5.10: Large sphere and small debonded regions in series 2P. Full bar = $1\mu m$.

Untreated fibre series evidence crack front pinning/bowing, with plateaus of material left behind (Figure 5.11). Surfaces are rough, with many river-like ridges on both large and small scales. The clumps are generally well-bonded to the matrix (especially small clumps). Most clumps show smooth fracture and larger clumps in 3F series specimens reveal hollow clumps, as well as both clump debonding and fracture (Figure 5.12).

Evidence is found of clumps fracturing before the arrival of the crack front and secondary crack fronts moving out to meet the main crack. This is seen as hyperbolic ridges around particles and clumps. The wider the hyperbola, the faster the secondary crack front, compared to the main crack[34]. Very fast fracture is revealed by these markings in the brittle specimen 3F-6 (quenched

Figure 5.11: Crack front pinning in seris 2F. Full bar = 10 μm.

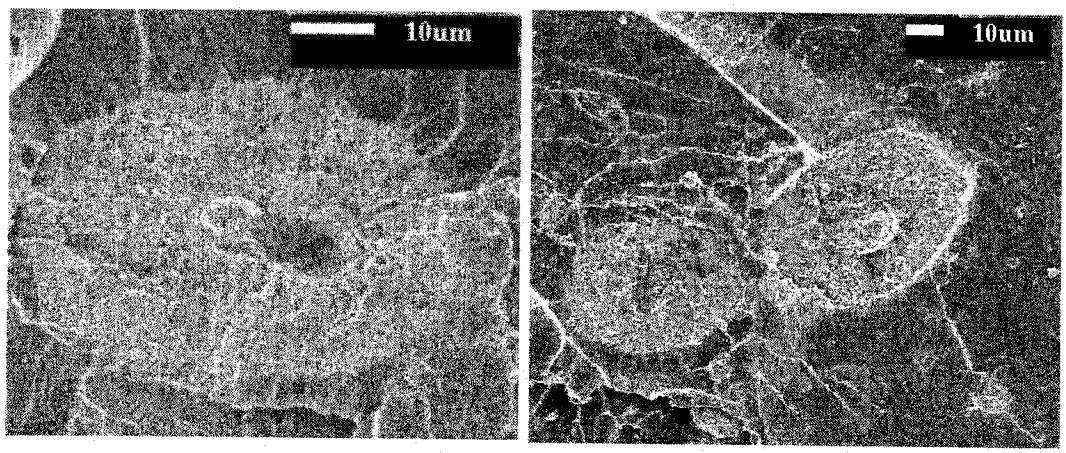

Figure 5.12: Holes in large clumps of series 3F. Full bar = 10 μm.

by cooling it quickly from higher temperature, in air). A comparison of the hyperbolic markings is shown in Figure 5.13. These same defects often have radial ridges (hackles) of shear yielding, which can be seen radiating from the clump in Figure 5.13's 3F-4 specimen.

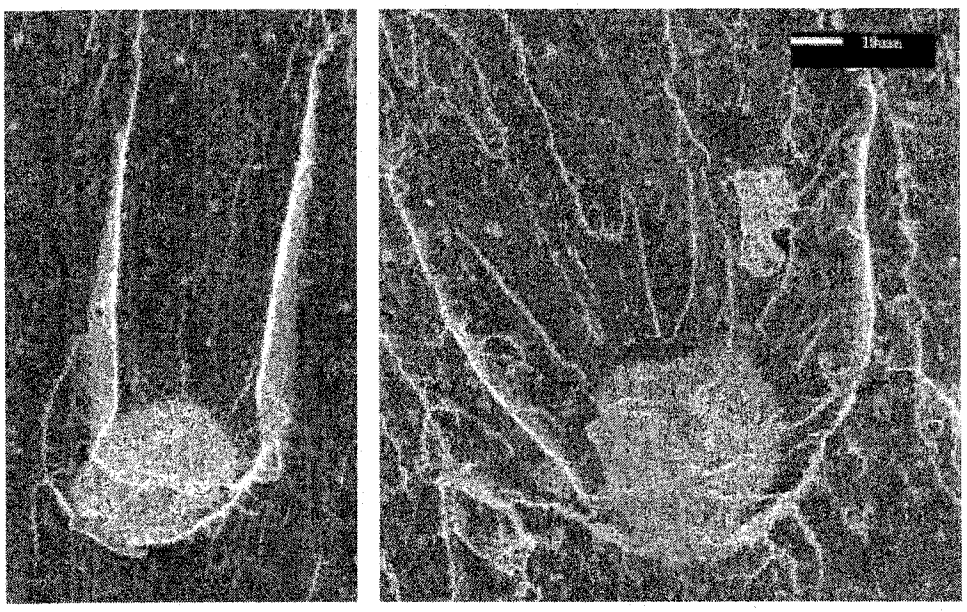

Figure 5.13: A comparison of hyperbolic markings between normal and quenched specimens in series 3F. 3F-6 was quenched and the narrow hyperbolic marks evidence embrittlement. 3F-4 shows evidence of hackles. Full bar = 10 μm for both micrographs.

Silane-treated fibre series have large-scale and extensive crack pinning (Figure 5.14), with larger plateaus of material left behind as evidence of crack deflection. Some clumps have smooth fractures, though most are roughly fractured and more cohesive, as seen in Figure 5.15. Large bowls are found around clumps, though the surfaces are less rough than untreated fibre series, due to a less extensively dispersed alumina phase. The clumps are also well-bonded to the matrix, as shown in Figure 5.16.

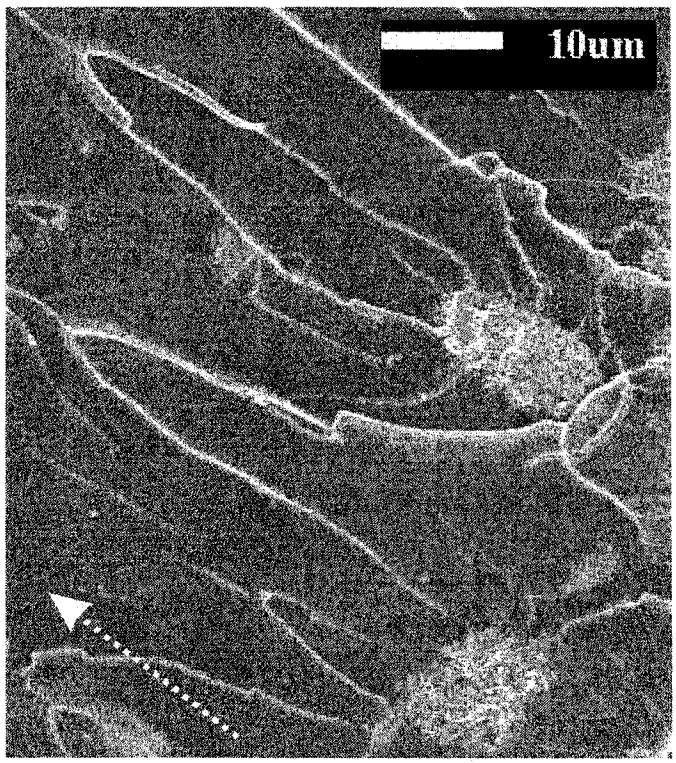

Figure 5.14: Crack pinning in series AF2. Arrow is in the direction of crack propagation. Full bar = $10\mu m$.

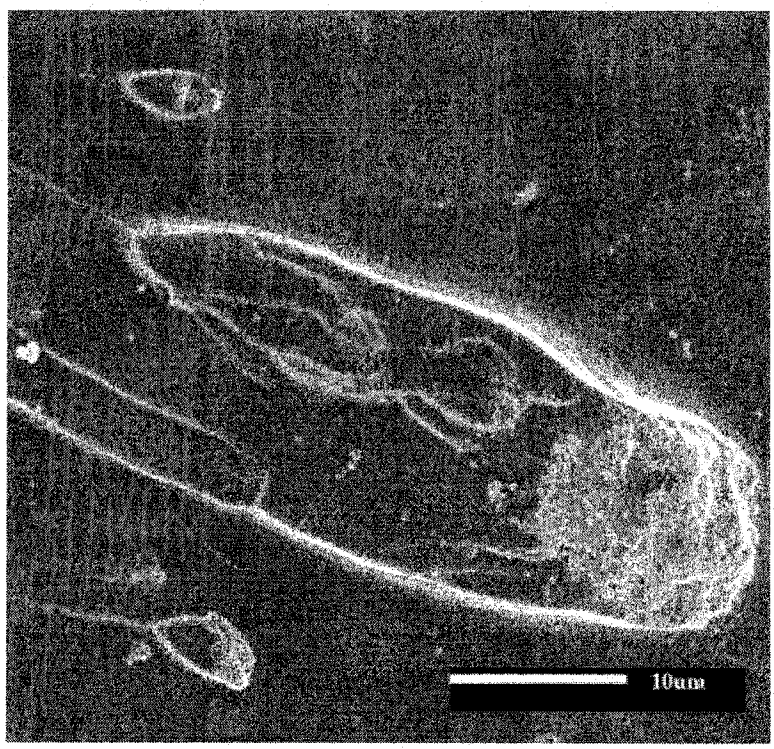

Figure 5.15: Deflection of crack front and crack pinning in series EF3 by a cohesive clump. Full bar = $10\mu m$.

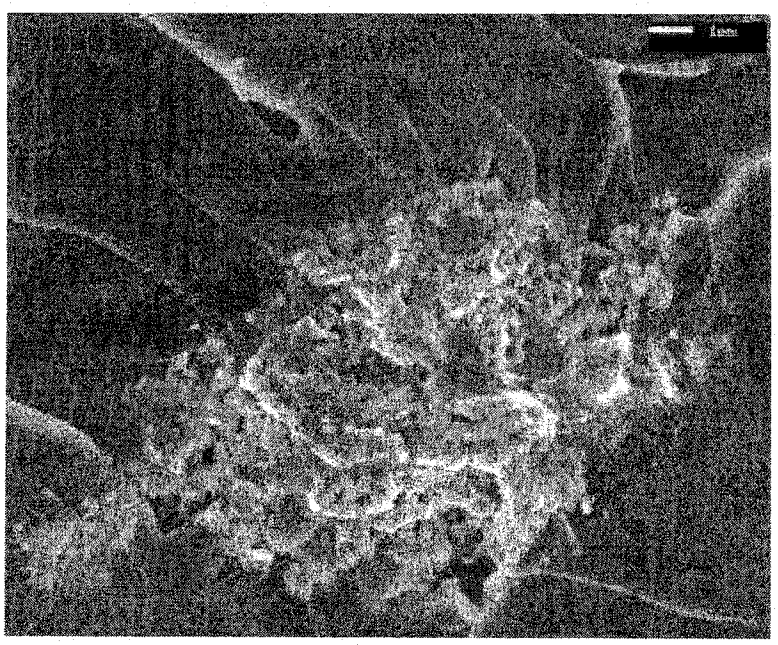

Figure 5.16: A cohesive fibre clump from series AF2; well bonded to the matrix. Full bar = $1\mu m$.

5.3 Tension and Compression Tests

A comparison between the "best" stress-strain response (highest strain) of each series is provided in Figure 5.17. The epoxy and nanocomposite specimens present a highly nonlinear response. All curves have an initial slope[1] that is approximately linear. Failure was always by fast fracture, originating almost exclusively at the extensometer knife edges, with no evidence of necking. Crack branching was frequently seen as the crack tip passed the half-width. Typical examples of failed specimens are found in Figure 5.18.

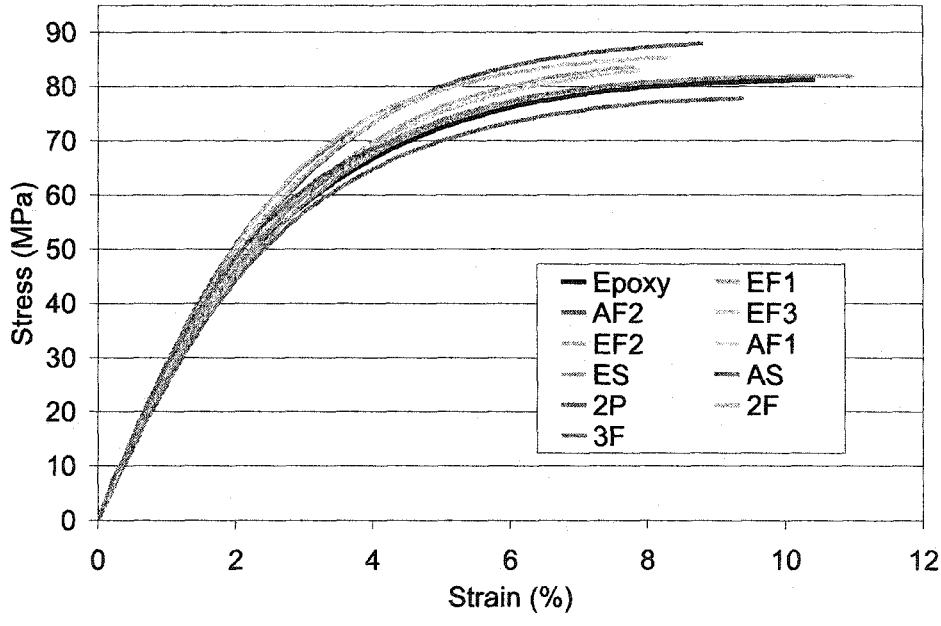

Figure 5.17: Comparison of stress-strain response for nanocomposite and epoxy series.

Neat epoxy shows a more ductile response, with reduced modulus and high strain before failure (at $\sim$ 11%). No yield point is evidenced, though a bi-linear approximation would place it close to 2.5% strain and $\sim$ 70 MPa. Both of the silane-catalyzed, unreinforced epoxies show very similar behavior to neat epoxy, with comparable initial slopes. The amino silane series, AS, has a slightly reduced failure stress and a larger drop in failure strain. The ES

[1] $<$ 0.5% strain, $<$ 30 MPa stress

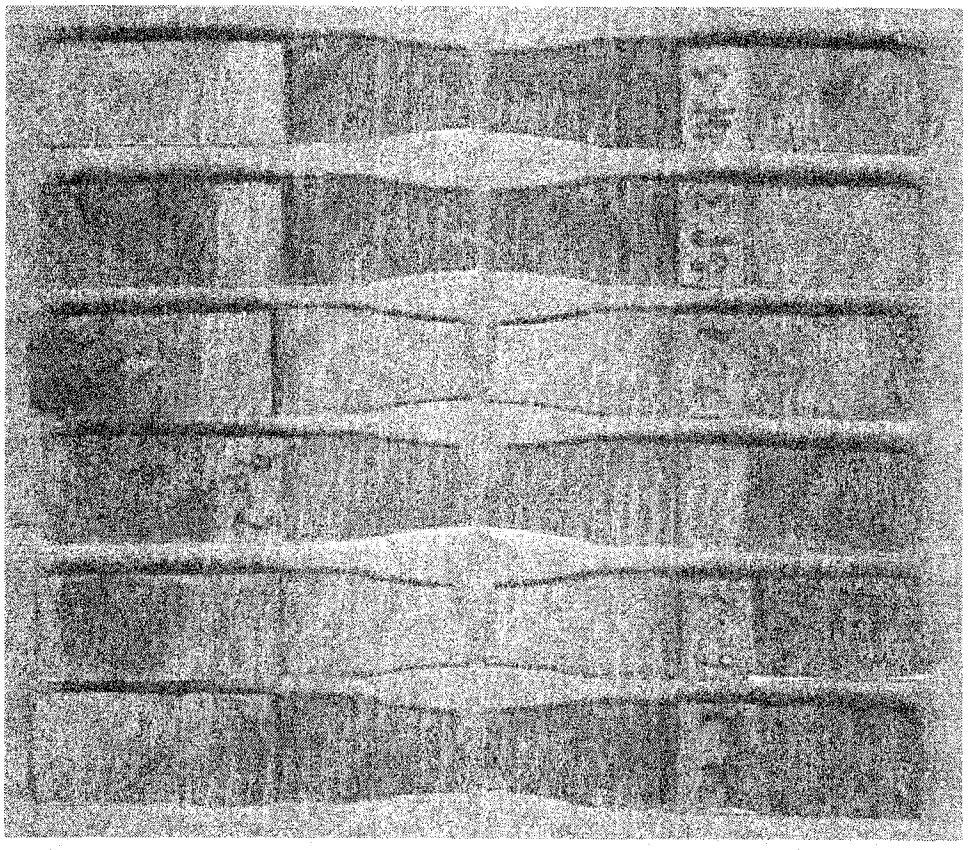

Figure 5.18: Typical examples of failed tensile specimens. All fractures started from 'bottom'. Specimen '7e-2' shows incomplete crack branch on the left hand side of the specimen.

series shows little difference to the neat epoxy, though has a slightly higher failure stress.

Series 2 and 3 nanocomposite have a much higher initial slope than neat epoxy, with comparable strengths, yet failure strains only 1/3 of the neat epoxy specimens.

Treated-fibre series evidence a different trend. Slopes are intermediate between neat epoxy and those of the untreated fibres (though filler fractions are intermediate also). Failure strains are reduced from neat epoxy and ES/AS, but higher than untreated fibre series; in contrast, failure stresses are higher.

To permit a more revealing comparison of the experimental results, the data is first placed in a more tractable format. Comparisons are made with respect to neat epoxy to establish how nano-alumina addition and processing variations have altered the mechanical response.

5.3.1 Modulus

There are a number of trends that can be gleaned from the modulus data. Table 5.1 shows the average modulus for each series, as well as modulus normalized with respect to epoxy.

Table 5.1: Comparison of tensile Young's Moduli.

Series	W_f (%)	E (GPa)	E/E_{epoxy}
Epoxy	x	2.57	1
2P	8.40	2.92	1.13
2F	4.20	3.07	1.19
3F	6.18	2.96	1.15
AS	x	2.54	0.99
ES	x	2.60	1.01
AF1	2.16	2.71	1.05
AF2	2.88	2.79	1.09
EF1	2.53	2.74	1.06
EF2	2.71	2.70	1.05
EF3	4.26	2.81	1.09

The higher W_f's show a much larger increase in modulus than do the fillers

around $2-3\%$. This accords with other nanocomposite studies, revealing an increase in modulus for increasing loadings up to $10-15\%$[24, 4].However, quality of dispersion and integration with the matrix appear to play a decisive role in modulus enhancement.

As mentioned in section 1.7, modulus changes because of the presence of a stiffer phase. The alumina reinforces the polymer chains through physical entanglement, weak hydrogen bonding and stronger covalent bonds. These restrict chain mobility and extensibility. One would expect that the increase in alumina loading from 2F→3F→2P would be accompanied by a comparable increase in modulus. Instead, there is a decrease in modulus. However, as seen in TEM's and SEM's, the 2F and 2P series have a more uniform dispersion than 3F and can therefore more extensively influence matrix deformation. At the same time, fibres have a higher specific surface area than spheres and appear to have integrated better with the matrix than the spherical particles (2P has evidence of voiding, debonding and pull out). Moreover, clumps of fibres appear to have better inter-particle cohesiveness than spherical particle clumps and should be able to carry a higher load before failing. These reasons provide compelling support for the superiority of the 2F series modulus over 3F and 2P series.

In the same vein, though 2F and EF3 series share equal alumina fractions, the higher fraction of fibres in small clumps or uniformly dispersed within the 2F series provide a greater modulus increase compared to the apparently well integrated, though larger clumps in EF3 specimens.

Within the treated-fibre series, little difference is seen, though the higher loading, increased dispersion and enhanced load transfer of the diamino - functionalized alumina (AF2) may account for its higher modulus, as compared with EF2 specimens.

Modeling Modulus

Modeling of modulus for particulate and whisker reinforcement has been approached from a number of directions[2]. Figure 5.19 shows the modulus vs. filler V_f for the experimental data, including the curves of a number of models.

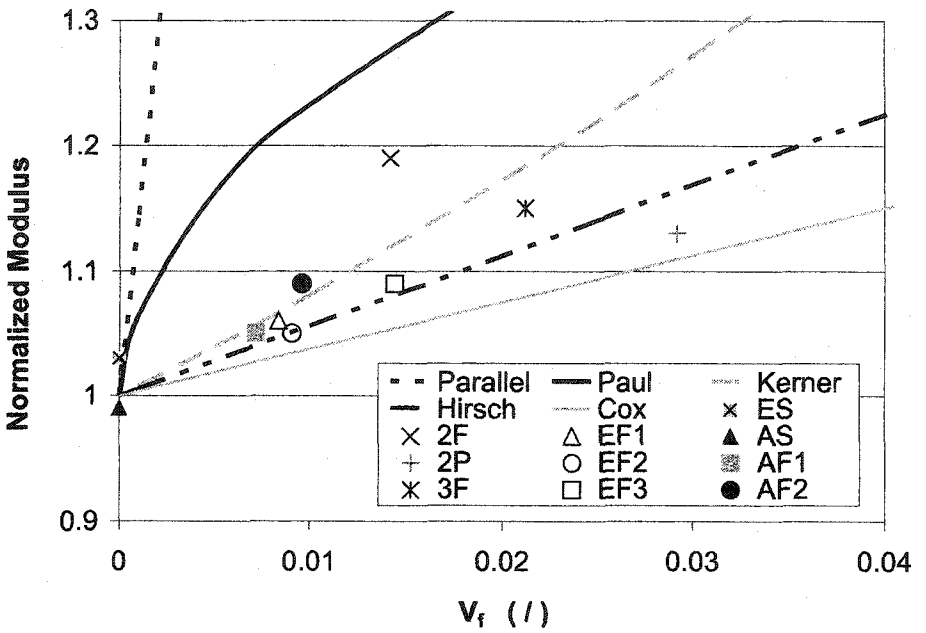

Figure 5.19: Comparison of experimental modulus with various model predictions.

The data is seen to fall below the extreme of the parallel model, shown as Equation 5.1. The series model[2], found in Equation 5.2, is not shown but would provide an extreme lower bound.

$$E_c = E_m V_m + E_f V_f \tag{5.1}$$

$$E_c = \frac{E_f E_m}{E_m V_f + E_f V_m} \tag{5.2}$$

These upper and lower bounds are not very useful predictors of modulus and have greatly oversimplified assumptions of uniform stress or strain. The first reason for this is the discontinuity of reinforcement in this work, especially for the case of the parallel model, which is better suited to model continuous reinforcement. In this experimentation, there exists a range of filler sizes (up to four orders of magnitude), varying interparticle separations and a distribution

[2]The parallel model uses a constant strain assumption (poorly bonded filler), while the constant stress model is the series model (perfectly bonded filler).

of filler shapes and compositions (flocc vs. aggregate vs. single particle). As a result, the stress will be distributed unevenly when the composite is loaded.[3] Furthermore, clumping reduces the effective packing fraction of filler and alters reinforcing phase surface areas. Lastly, bond strengths vary and can be discontinuous. All of these factors influence the amount of load the filler can carry and the extent of its impact on the neat polymer. All affect the resultant modulus.

Modeling variations attempt to incorporate some of these issues. The Hirsch model[2] uses a fraction of each of these series and parallel models and is given as Equation 5.3. By using x=0.045, the curve encompasses the data much better, taking into account that much of the filler is not as well bonded as is assumed in the series model.

$$E_c = (1-x)\frac{E_f E_m}{E_m V_f + E_f V_m} + x(E_m V_m + E_f V_f) \tag{5.3}$$

The Paul model[2] assumes a cubic inclusion embedded in a cubic matrix, where the constituents are in a state of macroscopically homogeneous stress. It over-predicts the modulus at low filler fractions (though it comes closer to other models as $V_f \sim 1$). It is given as

$$E_c = E_m \left(\frac{1 + (m-1)V_f^{2/3}}{1 + (m-1)(V_f^{2/3} - V_f)} \right) \tag{5.4}$$

$$\text{where} \qquad m = E_f / E_m$$

The Cox model[146, 2, 133], Equation 5.5, is for short fibre composites and assumes load transfer by shear, neglecting tensile matrix stresses. The curve in Figure 5.19 under-predicts the modulus, but uses a low orientation factor (q = 0.15) and a length/width ratio of 75/4. It is very sensitive to these two factors. The length to width ratio is probably not conceptually correct for nanocomposites, as the shear mechanism is based on micrometer lengths

[3]Even before loading there will be an uneven distribution, as discussed in Section 1.7.

rather than nano lengths and doesn't take into account the molecular chain structure of the polymer. Also, agglomerates are pervasive in these instances, and are spherical rather than whisker-like.

$$E_c = E_m(1 - V_f) + q\left(1 - \frac{\tanh z}{z}\right) E_f V_f \tag{5.5}$$

$$\text{where} \qquad z = \frac{l}{2r}\sqrt{\frac{E_m}{(1+\nu)E_f ln(\pi/4V_f)}}$$

To account for agglomerates, the Kerner equation [2, 135] was developed.[4] It is given as:

$$E_c = E_m\left(\frac{1 + ABV_f}{1 - B\psi V_f}\right) \tag{5.6}$$

It is based on spherical particles, but incorporates the dependence on modulus with a variable 'B', given as

$$B = \frac{E_f/E_m - 1}{E_f/E_m + A}$$

$$\text{where} \qquad A = \frac{7 - 5\nu_m}{8 - 10\nu_m}$$

and a reduced concentration term, ψ, depending on ϕ_m, the maximum packing factor.

$$\psi = 1 + \frac{V_m}{\phi_m}[\phi_m V_f + (1 - \phi_m)V_m] \tag{5.7}$$

The maximum theoretical packing of spheres is 0.74 and is reduced for non-spherical particles and agglomeration. Vassileva et al.[135] employed this

[4]From Halpin-Tsai.[45]

relation to relate dynamic mechanical behavior of alumina nanocomposites to filler type and loading. Here, the McGee variation[97], Equation 5.7, using a low packing factor ($\phi_m = 0.15$) to incorporate loose packing and agglomeration, provides a good fit of Equation 5.6.[5] Clearly more work needs to be done to incorporate filler-matrix interactions and dispersion non-uniformity in the modeling process.

5.3.2 Failure Stress

Strength enhancement is a function of two competing factors. For strength improvement, the higher strength alumina reduces the load carried by the matrix and greater load transfer is possible with a uniformly dispersed alumina fraction. Some clumps, especially well-bonded aggregates, can also take more load than the matrix and continue to act as reinforcement, though at a micrometer scale. In contrast, strength can be impaired by poorly bonded or flocc containing clumps, that act as voids. These reduce the effective cross-section of the specimen, act as stress concentrators, and are potential sites of fracture initiation that can also attract pre-existing cracks. If in a ductile matrix, these might provide strengthening by diffuse shear initiation and extensive plastic deformation, via cavitation. However, the Epon 826 matrix is instead brittle and increasing the V_f of alumina permits reduced polymer chain mobility and less plastic deformation.

Experimental Results

In this investigation, the differences in the failure stress of the nanocomposites from that of the neat epoxy are all within 15%. They are therefore of limited significance and as a result, only general trends will be discussed. This is depicted below in Figure 5.20 and tabulated in Table 5.2, including normalized values of strength.

One trend is a decrease in strength with increasing alumina reinforcement, for nanocomposites containing untreated alumina. The dispersed fraction of

[5] $\phi_m = 0.632$ for random, loose packing without agglomeration and $\phi_m = 0.370$ for random close packing with agglomeration.

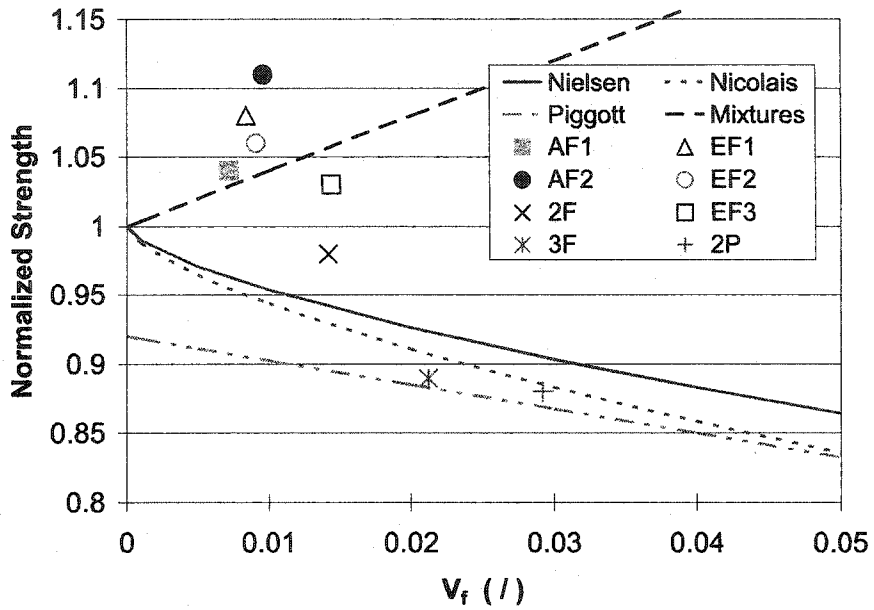

Figure 5.20: Failure strength dependence on alumina volume fraction.

fibres in Series 2F probably provides some reinforcement, as evidenced by SEM's of good matrix interaction, while the overall reduction in strength is likely caused by the increased frequency and size of clumps (potentially critical flaws). Series 3F contains larger and weaker clumps than 2F, and by the same

Table 5.2: Comparison of normalized average failure stresses.

Series	V_f (%)	σ_f (MPa)	$\sigma_f/\sigma_{f-epoxy}$
Epoxy	x	77.99	1
2P	2.92	68.68	0.88
2F	1.42	76.81	0.98
3F	2.12	69.66	0.89
AS	x	76.31	0.98
ES	x	81.80	1.05
AF1	0.72	81.34	1.04
AF2	0.96	86.72	1.11
EF1	0.84	84.24	1.08
EF2	0.91	82.50	1.06
EF3	1.44	80.09	1.03

rationale has a lower strength. Similar arguments could be used for series 2P specimens, though the weakening is more prominent owing to a lack of interaction with the matrix by the larger fraction of better dispersed, but poorly integrated (bonded) particles.

Silane treated fibres series all evidence a slight increase in strength. This contrasts with most particulate reinforcement series[2]. Having little distributed phase, this is primarily a function of the aggregate clumps. The SEM's show cohesiveness and well-bonded interphase regions. The clumps are micrometer- scale features with enhanced load transfer across the silane/ siloxane interphase. The silane (siloxane) can be seen to have altered any number of mechanisms, including decreasing the impact of potential flaws, improving interfacial bonding, decreasing stress concentrations and enhancing load transfer. Series EF3 is possibly less effective in this, because of such extreme phase segregation within larger hybrid clumps (being consequently not as strong as other clumps). Series AF2 is the strongest series, but only contains $\sim$ 2.9 wt.% fibres ($<$ 1% by volume).

Particle size analysis, in Section 4.3, reveals the low clump size of AF2 alumina and also the impact of settling stratification on the size distribution, as per Figure 4.9. The use of settling to stratify the particle distribution after both components of the epoxy resin have been mixed is likely the source of this improvement in strength. This process removes the larger, pre-existing and phase-segregated clumps before gelation occurs, but preventing the agitation-induced floccs of series 3F via continued sonication.

Another possible mechanism is that caused by the presence of the silane itself, for silanes are often used as polymerization catalysts or toughening agents. To separate the impact of the silane from that of the fibre reinforcement, Table 5.3 outlines the improvement in strength for amino-silane treated specimens ($\uparrow\sim$ 3%) and the relative decrease for ethoxy-silane treated specimens ($\downarrow\sim$ 5%) when normalization is made with respect to AS/ES properties.

Table 5.3: Potential impact of silane on failure stress.

Series	V_f (%)	$\sigma_f/\sigma_{f-silane}$	$\sigma_f/\sigma_{f-epoxy}$
AF1†	0.72	1.07	1.04
AF2	0.96	1.14	1.11
EF1‡	0.84	1.03	1.08
EF2	0.91	1.01	1.06
EF3	1.44	0.98	1.03

Normalization made using average values for epoxy and silane-catalyzed epoxies.
† - uses AS strength values ‡ - uses ES strength values

Strength Modeling

As mentioned, strength modeling predicts a decrease in strength for particulate reinforcement. Strength theories apparently do not account well for such small particles or high interfacial areas, nor for the interfacial region – a key to the nanocomposite and composites in general. The models presented in Figure 5.20, which are representative of the types of theory being applied to nanocomposite materials, are now described further.

The Piggott and Leidner model[100], Equation 5.8, is an empirical relation using a stress concentration factor, 'k', and a constant, 'b', to describe the particle-matrix adhesion.

$$\sigma_c = k\sigma_m - bV_f \tag{5.8}$$

Here, k = 0.92 and b = 1.4.

The Nielsen model[96], is a power law equation relating strength decrease to poor bonding and reduced matrix area. Similar to Paul's modulus model, it uses a cubic matrix filled with cubic particles and a stress concentration factor, k = 0.5, as in Equation 5.9.

$$\sigma_c = \sigma_m(1 - V_f^{2/3})k \tag{5.9}$$

The Nicolais and Narkis model[95], is based on uniformly dispersed spher-

ical particles in a cubic matrix. The minimum matrix cross section perpendicular to the applied load is where fracture is assumed and strength is described as

$$\sigma_c = \sigma_m(1 - 1.21V_f^{2/3}) \tag{5.10}$$

Equation 5.9 and Equation 5.10 fall between untreated fibre data points, but ineffectively account for silane treated reinforcement. The last model is the rule of mixtures model, using the strength of the fibres, $\sigma_p = 400$ MPa and $\sigma_m = 80$ MPa for epoxy. It is more appropriate for continuous reinforcement, but does account for strength improvement. It is given as:

$$\sigma_c = \sigma_m V_m + \sigma_p V_f \tag{5.11}$$

5.3.3 Failure Strain

In ductile matrices, failure strain has been increased by delaying the presence of a critical flaw. This has been accomplished by extensive debonding and cavitation-type plastification or the initiation of diffuse shear mechanisms. However, all nanocomposite series in this investigation (involving a brittle matrix) reveal the detrimental impact of inorganic filler addition on failure strain. Strain decreases with increasing V_f, as shown in Figure 5.21, and because this change in property far exceeds that for strength or stiffness ($\Delta\epsilon \approx$ 65% compared with $\Delta E \approx 30\%$ or $\Delta\sigma \approx \pm 15\%$), it represents the most significant impact of alumina addition.

For glass-fibre reinforced epoxies, it is known that matrix cracking is an important initial damage mechanism and a strain of $\sim 3\%$ has been used as a criteria for damage onset[53]. Without the continuous reinforcing phase, damage onset in particulate reinforced composites can quickly accumulate and initiate failure of the specimen. The same restriction of the matrix (and plastic deformation mechanisms) by the alumina that enhances the stiffness also causes anti-plastification or embrittlement[135] and lower failure strains. Even with a

well-dispersed phase, the chain restriction and potential increase in cross-link density of brittle alumina addition only further reduces plastic deformation.

Untreated alumina addition causes the greatest reduction in failure strain with increased V_f. This decrease parallels that of strength, though failure strain is further reduced - to as little as one-third of that of neat epoxy. It is clear that poor bonding and the large clumps in these series negatively impact the strain. The retained powder agglomerates act as stress concentrations and frequently contain flaws. Silane treatment to increase clump cohesiveness and matrix integration supports this; at similar alumina loadings, a large difference is seen between 2F and EF3 specimens. The modification of the powder has not caused plastification, yet it has reduced the size and extent of flaws, and limits the reduction in failure strain. Within the treated powder series, failure strain still decreases with increasing V_f, though not to the same extent as untreated alumina series.

Further, it is noted that in the silane catalyzed series (AS/ES) the presence of amino-silane has greatly reduced the failure strain from that of the neat

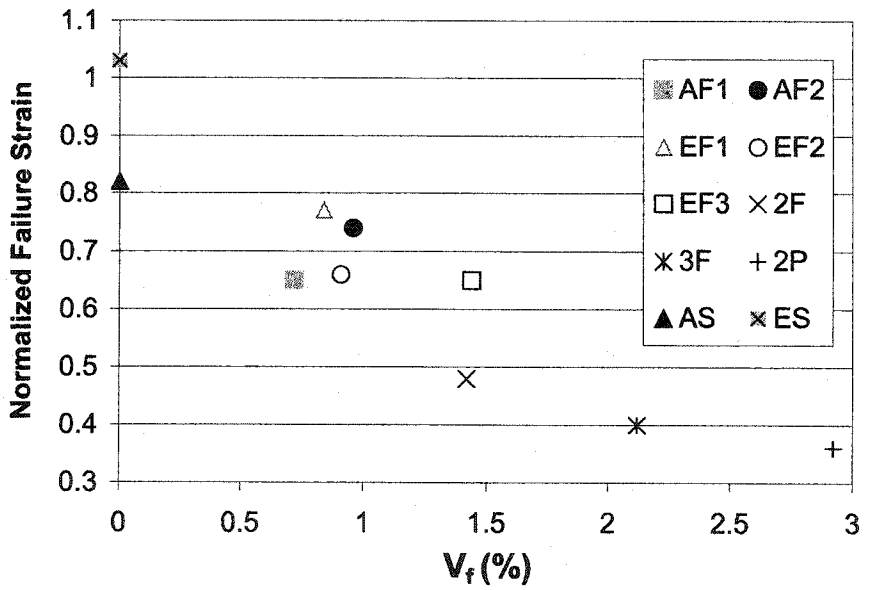

Figure 5.21: Failure strain dependence on alumina volume fraction.

epoxy (−18%), whereas the ϵ_f for epoxy-silane is slightly enhanced (+3%). If the presence of amino-silane on cross-link density or plastification of the matrix is so great, it could be that the negative impact of the fibres is less the cause of this decrease in failure strain than that of the silane itself. To isolate the impact of the fibres on failure strain, without the influence of the silane (although flaws, changing cross-link density and thermal residual stresses make these values extremely inter-related), one can normalize strain values for treated-fibres series with AS or ES values, as was done for strength. A comparison of these two normalization strategies is shown in Table 5.4.

Table 5.4: Comparison of normalized average failure strains.

Series	V_f (%)	ϵ_f (%)	$\epsilon_f/\epsilon_{f-epoxy}$	$\epsilon_f/\epsilon_{f-silane}$
Epoxy	-	10.67	1	-
2P	2.92	3.80	0.36	-
2F	1.42	5.09	0.48	-
3F	2.12	4.22	0.40	-
AS	-	8.74	0.82	-
ES	-	11.00	1.03	-
AF1	0.72	6.98	0.65	0.80†
AF2	0.96	7.94	0.74	0.91
EF1	0.84	8.26	0.77	0.75‡
EF2	0.91	7.01	0.66	0.64
EF3	1.44	6.95	0.65	0.63

Normalization made using average strain for epoxy and AS or ES series.
† - uses AS strain values ‡ - uses ES strain values

The greatest change is seen for AF1 and AF2, where strain reduction has decreased and represents a relatively minor consequence of alumina addition compared to untreated and poorly bonded series (3F, 2P). In particular, along with its enhancement in strength, AF2 appears to be a relatively successful nanocomposite series due to its higher failure strain. Advances in dispersion (reducing clumping), and an improved surface treatment could achieve enhancements much closer to those of in-situ and alumoxane incorporated nanocomposites already synthesized by chemically based routes[4, 137].

It is interesting to note that the failure strain decreases while tensile mod-

ulus increases. The apparent discrepancy lies in the differences in the mechanisms by which property change occurs. For modulus, the filler influences chain mobility in the elastic range, while strain often involves more complex and plasticity oriented mechanisms. As well, the failure process relys on stength characteristics of the filler, hence the flaw spectrum of aggregates plays a role not considered in modulus determination.

5.4 Fracture and Toughness

Similar to other properties, the toughness is a compromise between toughening/strengthening mechanisms, and those of stiffening/embrittlement. Toughness is calculated based on the linear elastic fracture mechanics principles of the stress intensity factor, K. The stress intensity factor is related to crack length and far-field stress as[20]:

$$K = kY\sigma\sqrt{a} \tag{5.12}$$

where the shape function, Y, accounts for the crack length to specimen width ratio:

$$Y = 1.12\sqrt{\pi} - 0.41\frac{a}{W} + 18.7(\frac{a}{W})^2 - 38.48(\frac{a}{W})^3 + 53.85(\frac{a}{W})^4$$

and 'k' is a stress concentration factor, accounting for a narrowed and constant curvature gauge section, and is used because this particular shape function is for constant width in the gauge length. Here, k = 1.34 is used.

Figure 5.22 shows the calculated toughness as a function of crack length for untreated fibres and Figure 5.23 shows the calculated toughness as a function of crack length for treated fibres.

The toughness reveals a crack-length dependence, with increasing values for increasing crack length. As well, much scatter is seen in the data. Since K_{epoxy} is also seen to increase with crack length, Figure 5.24 and Figure 5.25 present toughness normalized with respect to neat epoxy to help alleviate this dependence.[6]

[6]Values are based on linear fits to the toughness data and it is these fits that are normalized with respect to each other, at each crack length.

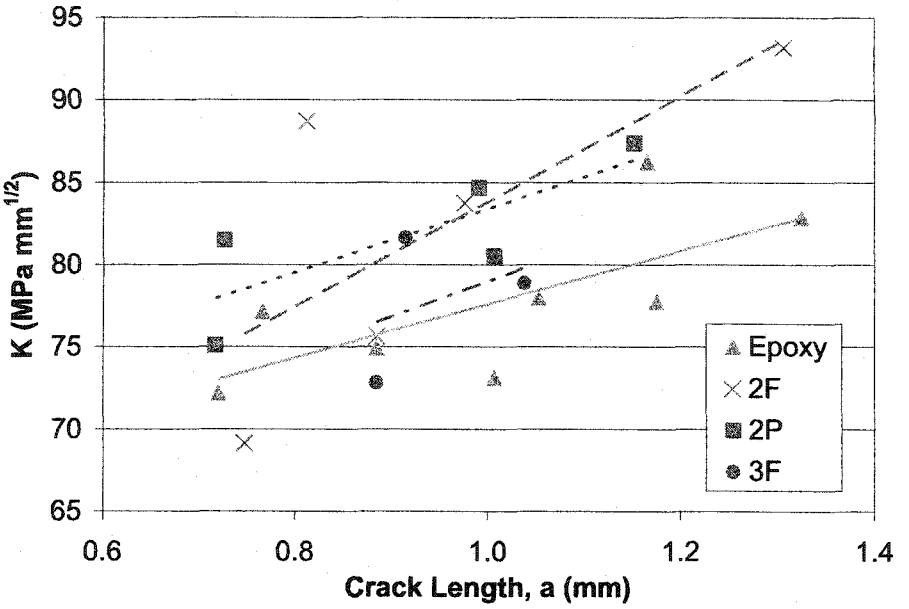

Figure 5.22: Variation of calculated toughness with crack length (untreated).

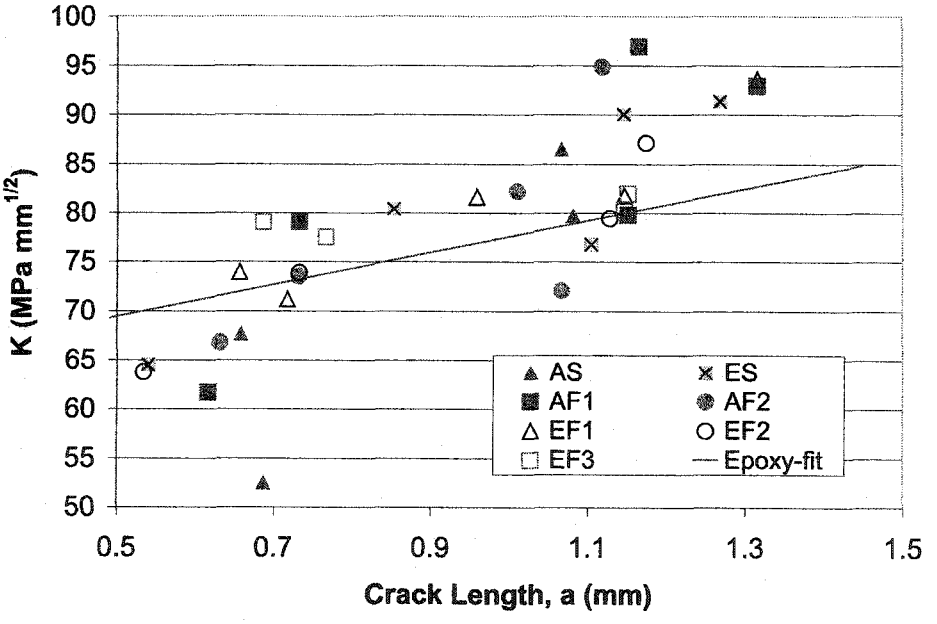

Figure 5.23: Variation of calculated toughness with crack length (treated).

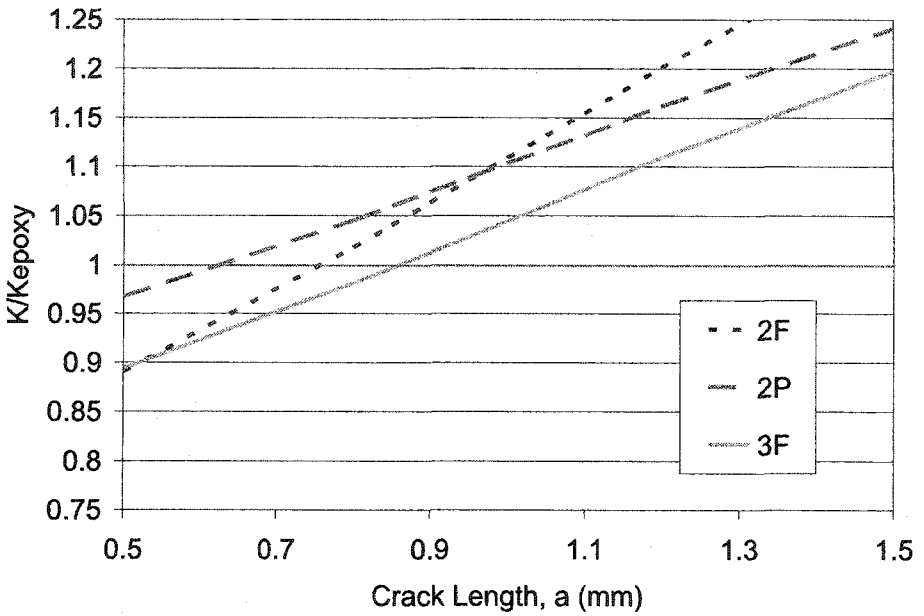

Figure 5.24: Increase in relative toughness with crack length (untreated).

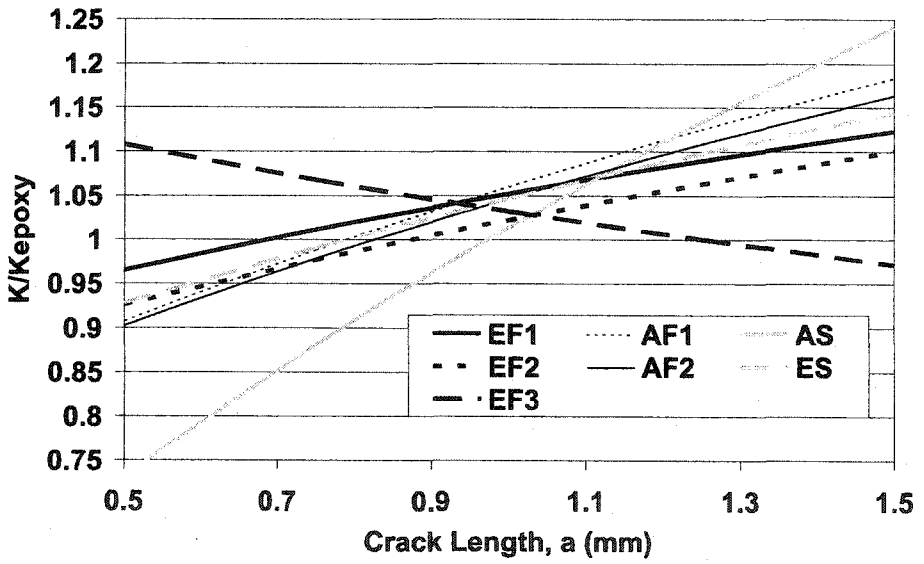

Figure 5.25: Changes in relative toughness with crack length (treated).

If toughness is regarded as more accurate for crack lengths approaching those of the ASTM standard (D 5045), toughness enhancements are seen for

all series above 1 mm, except for EF3. The largest increase is for 2F, followed by 2P, the silane treated alumina series and then 3F.

From SEM's of fracture surfaces, treated-fibre series would be expected to show the largest toughness improvement, based on the presence of off-crack plane mechanisms (crack deflection, particle/clump debonding) and extensive in-plane crack pinning. This is not supported by the calculated toughness, as series with more uniformly distributed alumina present more enhancement. This is especially so for 2P specimens, where little evidence of crack front pinning and only minor changes in surface roughness are present.

As the calculated toughness is a construct, a more primary evaluation of toughening is employed; namely, the area under the load-displacement curves or the tensile stress-strain curves. The area represents the energy required for fracture and parallels the calculated "fracture" toughness, which can be related to an energy criterion by the relation G $\propto K^2/E$ for linear elastic cases. More generally, it can be considered the strain energy density required for fracture. The strain energy density can then be given as:

$$\int_0^{\epsilon_f} \sigma d\epsilon \quad which\ is \quad \approx \frac{1}{2}\sigma\epsilon$$

In the case of area toughness, calculation is made numerically, using a trapezoidal integration procedure.[7]

Area data closely follows with calculated toughness, though with the opposite slope; a decreasing area with crack length is found. This is shown in Figure 5.26. Figure 5.27 shows the average of each series plotted against W_f.

Independence of crack length would be expected from K_{IC} values if this was a plane-strain case. The largest microstructural features are $\sim 50\mu m$ in diameter and the crack (and sharp-crack regions) are of equal or larger size than this. Hence, it would be expected that the crack length is sufficient for K_{IC} relations to be valid. However, in comparison to measurement of K_{IC} as specified by ASTM D 5045, a/W is not within the required range (a/W $< 10\%$), though the crack length is of the order of the thickness (a/t $\sim 40\%$).

[7]Load-displacement data is input to Matlab as vectors and the "trap{$\bar{d}$,$\bar{P}$}" command used to obtain the area.

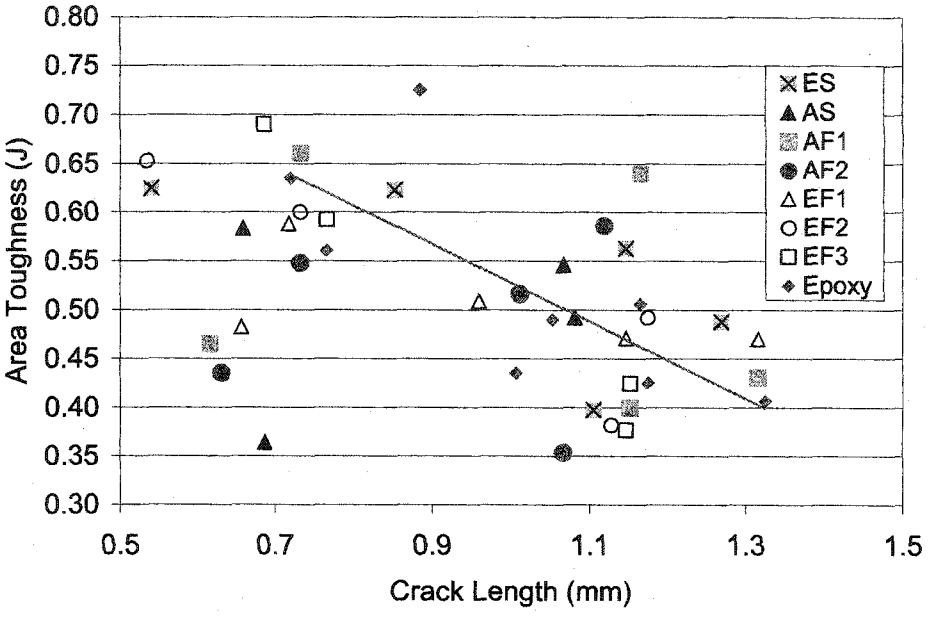

Figure 5.26: Variation of fracture curve area toughness with crack length.

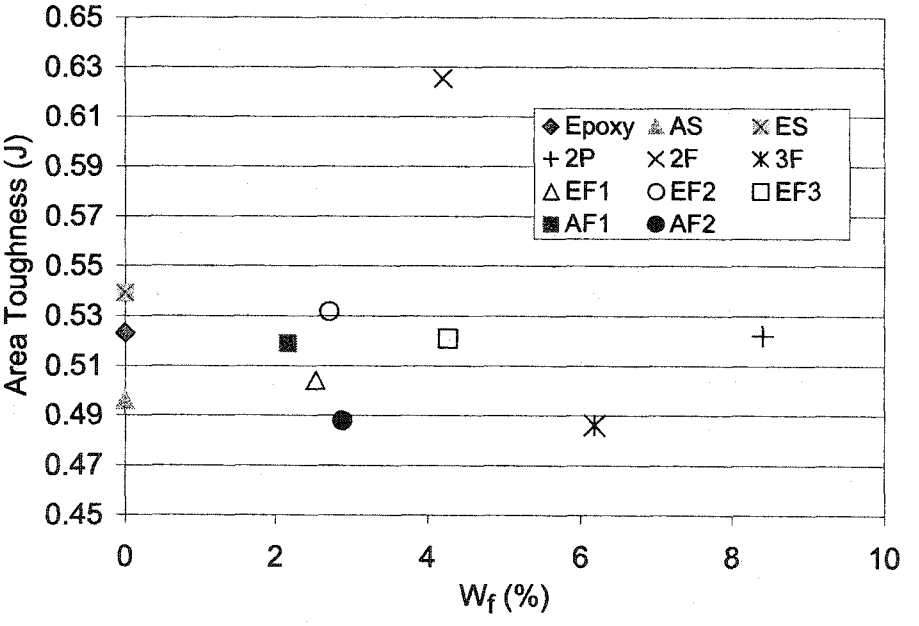

Figure 5.27: Variation of average fracture curve area toughness with W_f.

However, here we have a general toughness parameter, not K_{IC}. The potential impact of edge effects in this instance is great, as is the multi-modal fracture under plane-stress. Another criterion may provide a more consistent relation.

The latter of the energy criteria is calculated as the area under the stress-strain curves. These values are shown in Table 5.5.

Table 5.5: Average stress-strain curve area.

Series	W_f (%)	Area (MPa%)
Epoxy	0	668
2P	8.40	155
2F	4.20	266
3F	6.18	191
AS	0	507
ES	0	719
AF1	2.16	398
AF2	2.88	499
EF1	2.53	510
EF2	2.71	431
EF3	4.26	351

Although the higher stresses in the nanocomposite series serve to increase the area, overall area reduction (and toughness) is driven down by decreasing failure strains. As previous studies of inorganic filler addition have shown decreasing toughness, these trends make more sense than the results of calculated toughness. Moreover, the reduction in toughness makes intuitive sense when considering that the brittle epoxy is being 'toughened' by a stiff, relatively low toughness ceramic. Works using more ductile matrices have shown ductility increase with nano-clay addition[8], though only if the clay is in an exfoliated state, for the matrix plasticity allows beneficial mechanisms (cavitation, increased plastic flow) to operate.

Agglomerates in the epoxy have a major impact on toughness. As shown in Figure 5.13, there is evidence that agglomerate defects play a role in fracture. Here, the hackles radiating from the clump illustrate the shear yeild associated with fracture within the clump before crack front approach, followed by a

secondary crack front moving out from the defective clump to meet the main crack front. The hyperbolic lines around clumps in previous micrographs also show this[22, 34].

Plotting stress-strain area vs. filler fraction, the impact of reduced failure strain on toughness is seen. (Figure 5.28) An exponential curve fit to the data shows good agreement.

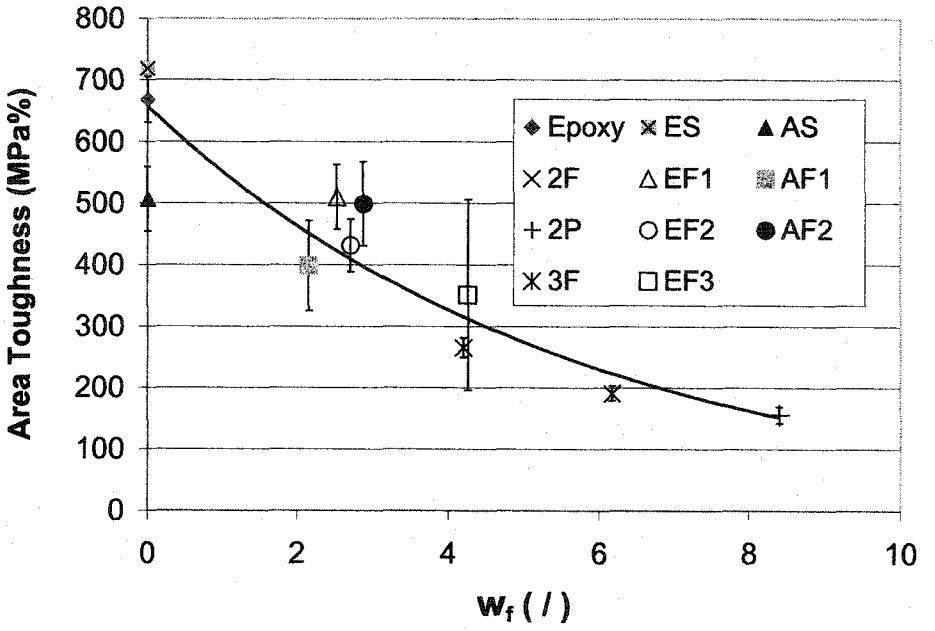

Figure 5.28: Variation of average stress-strain area toughness with W_f. Error bars represent the range in values used to average the data.

5.5 Further Modeling Implications

Predicting polymer properties has typically relied on the assumption of a continuum in the material. This has provided excellent results for many materials, based on meso or micrometer scale features. These continuity assumptions usually involve assumptions of isotropy or homogenization of anisotropy to facilitate the modeling. Incorporation of micro (particulate) or micro-meso (long fibres) materials increases the difficulty of analysis, but continuum assumptions can generally be made within each constituent. Homogenization is possible, as with the assumption of orthotropic plies in laminate composites (ie., classical laminate theory). For mono-dispersed inorganic fillers, additional "phases" (having a range of properties) can be used to homogenize the material for modeling purposes. Similarly, flaws can be modeled with a fracture mechanics based approach, though most flaws are idealized as uniformly shaped defects in or between homogeneous phases[93, 128]. For example, imperfect wetting of micrometer-scale spheres in a rigid matrix can be modeled in this manner[83, 21, 33]. Though retaining their theoretical basis, these models could more closely approximate real materials by incorporating distributional variations in defects using statistical flaw spectra, as has been done for pristine polymers[125].

In fact, the current investigation shows this problem of inhomogeneity can be significant and that the synthesis of polymer nanocomposites concomitantly influences subsequent efforts at modeling material properties. For nanocomposites, modeling is truly a scale issue. Previous discussion has shown that the polymer modulus can be well modeled at the macroscale, with isotropic assumptions accounting in various ways for nonuniform dispersion. This, however, tends to divorce the model from the mechanics of the problem through a convenient constant. At the same time, strength is predicted to decrease, though this is clearly not the case for silane-treated alumina addition. Addition of a non-uniformly distributed second phase causes variations in modulus and strength, and provides a spectrum of local stress-strain states throughout the macro-level polymer. Similarly, damage initiation and propagation is gener-

ally dependent on dispersion and the interfacial regions between constituents, owing to large property gradients at these boundaries.

This work has further shown that there is a great range in distribution of reinforcement, spanning several orders of magnitude. This provides an enormous variation in interactions between constituents that one model type may not be able to adequately incorporate. Within the distributed phase there is a variation in material properties corresponding to different clump morphologies (flocced vs. agglomerated, packing factor, etc.) and material constituents (i.e., presence of a siloxane network within the clump). Further, constituent properties do not necessarily follow macroscale laws pertaining to modulus or Poisson's ratio, and can be completely different from the macroscale values[127]. This is potentially the case with ceramics, where critical flaw size is linked to grain size. A number of assumptions may be invalidated if the particle is below this scale. Similarly, the reinforcing, coupling and matrix constituents for nanocomposites have comparable primary dimensions. At the molecular level, interfacial regions do not exist in the continuum sense and if nanoscale particles are truly mono-dispersed, there is no longer a distinction between phases. For adequate modeling, this nano-scale material inhomogeneity must be taken into account, in addition to the macro-scale inhomogeneities related to macro/meso dispersion.

Enhancement of computing power is permitting the application of numerical analysis to transcend the continuum assumptions by focusing on material response at the constituent molecular level. An example of this is an investigation of chain kinetics in polymer deformations[148]. Currently these analyses are still primitive and the simulations involve low orders of polymer molecules or a few macromolecules. In the future, these nano scale and sub-nano scale analyses can potentially lend credence to larger-scale continuum assumptions[25].

Chapter 6

Conclusions

The synthesis of a composite material is a marriage of the diverse properties of its constituents to create a new material of enhanced or altered properties. However, just as the individual components provide meritorious attributes for use by engineers, so too do the use of these components place limitations on the manner in which they can be combined and the efficacy of their integration. Polymer/ceramic nanocomposites are exemplary in this respect, owing to the benefits of high strength and stiffness particles, and the possibility of near-homogeneous integration with the polymer matrix. Yet, the mechanical properties of the filler are a result of a different chemical system, which inhibits such facile processing when employing a plastic matrix. Moreover, the nano scale size and associated large specific surface areas present a significant challenge to nano scale dispersion of ceramic within the polymer system in the face of pre-existing agglomeration.

A number of methods exist to ameliorate these problems, perhaps the most successful of which are the chemical alteration of the ceramic during synthesis and the in-situ synthesis using colloidal techniques. These permit the possibility of chemical integration of ceramic within the polymer and removes such problems as the re-dispersing of the ceramic in another medium. Other approaches involve selection of more compatible reinforcing or matrix materials. These permit different processing techniques and bring into play more forgiving constituent properties (i.e., synthesis via melt processing, higher initial ductility, etc.). However, these issues cannot be sidestepped if modification of

the polymer system, already chosen for specific attributes, is the aim.

In the present work, the mechanical properties of alumina particle/epoxy nanocomposites have been investigated and the processing of this composite has been related to the mechanical properties. A number of significant observations can be made with respect to the impact of material inhomogeneity and processing variations on elastic and fracture behaviors.

- The agglomeration of dry nanoparticles is inevitable. Though the size of agglomerates can be reduced by ultrasonic processing, agglomerates will still exist in the polymer nanocomposite. These will consist of weak floccs of small particle clumps and individual particles, stronger aggregates of densely packed particles and hybrid agglomerates of smaller clumps.

- Settling of particles results after cessation of mixing. Large clumps settle faster. Settling can stratify the particle size distribution and cause retention of smaller particles, but can also reduce the weight fraction. Gradients of particles and clumps can become significant in thicker specimens.

- Spherical particles have weaker clumps and appear to have poor integration within the matrix, compared with the fibre form of the alumina powder.

- Silane treatment has been unsuccessful at enhancing the particle dispersion, but has improved clump strength and provided better powder-matrix integration.

- Strength enhancement has been demonstrated at even low particle loadings. Untreated powders have apparently weaker clumps that are potential defects, lowering strength; smaller clumps and potentially stronger clumps are seen to be less detrimental to material properties.

- Modulus increases with weight fraction, though this increase is less influenced by enhanced dispersion than by improved matrix integration.

- Restriction of ductility (embrittlement) is the most significantly impacted property; higher loadings cause greater reduction in failure strain. Failure strain correlates with defect size and particle-clump strength.
- Digital analysis provides a potentially powerful tool for morphological and distribution analysis, though a standardized approach must be employed.
- Filler distribution non-uniformity and filler morphological inhomogeneity both play key roles in material properties. They should be incorporated into the modeling of nanocomposites.

Chapter 7

Future Work

This investigation was based on the premise that alumina addition could extend the failure envelope of glass fibre wound epoxy pipes by delaying matrix cracking. It has progressed through the challenge of powder dispersion, the complexities of surface treatment and landed in the miasma of the mechanical response of nanocomposites with inhomogeneities. Much work, of a directed and organized manner, remains:

- Further characterization of the powder structure is needed. This includes effects of surface hydration and the strength of agglomerates. Differences in structure between spherical and fibre clumps, and the agglomeration mechanisms that cause them would be useful.

- Having established the nature of basic processing concerns, further testing should be conducted using ASTM standard specimens, particularly for fracture tests.

- In-situ particle dispersion using ultrasonic processing should be conducted in conjunction with rigorous evaluations and modeling.

- In conjunction with clump breakdown and dispersion should be a segue into the means by which infiltration of clumps by components of the epoxy occurs.

- Related to this is the practical concern of mixing particles in a lower viscosity fluid (such as methanol) that is chemically suited to mixing of

alumina and incorporation with the epoxy (and later evaporated).

- Silanization should be conducted more rigorously and the nature of the surface treatment better characterized to allow deeper understanding of clumping (i.e. polysiloxane clumps, hybrids).
- One should better understand settling and clumping to allow higher loadings of filler and comparison of series having equal W_f's.
- Embrace the opportunity presented by digital analysis tools for dispersion and morphological characterization; use of statistical analysis can be made.
- Pursue hybrid nanocomposites incorporating rubber to stimulate different mechanisms or employ rubber alone to enhance toughness by extension of failure strain rather than failure stress.
- Look into other mechanical properties such as wear, impact response or viscoelasticity.

Bibliography

[1] M. Abboud, M. Turner, E. Guguet, and M. Fontanille. Pmma-based composite materials with reactive ceramic fillers. part 1 chemical modification and characterization of ceramic particles. *Journal of Materials Chemistry*, v7, n8:1527–1532, 1997.

[2] S. Ahmed and F.R. Jones. A review of particulate reinforcement theories for polymer composites. *Journal of Material Science*, 25:4933–4942, 1990.

[3] M. R. Alexander, G. E. Thompson, and G. Beamson. Characterization of the oxide/hydroxide surface of aluminium using x-ray photoelectron spectroscopy: A procedure for curve fitting the o 1s core level. *Surface and Interface Analysis*, 29:468–477, 2000.

[4] M. Alexandre and P. Dubois. Polymer-layered silicate nanocomposites: Preparation, properties and uses of a new class of materials. *Materials Science and Engineering*, 28:1–63, 2000.

[5] T. Allen. *Particle Size Measurement.* Chapman and Hall, London, 1974.

[6] L. O. Andersson, J. Sunder, S. Persson, and L. Nilsson. Optimizing mixing performance through filler dispersion control. *Rubber World*, March:36–45, 79, 1999.

[7] R. Andrews, D. Jacques, M. Minot, and T. Rantell. Fabrication of carbon multiwall nanotube/polymer composites by shear mixing. *Macromolecular Materials and Engineering*, 287:395–403, 2002.

[8] B. J. Ash, J. Stone, D. F. Rogers, L. S. Schadler, R. W. Wiegel, B. C. Benicewicz, and T. Apple. Investigation into the thermal and mechanical behavior of pmma/alumina nanocomposites. In *Filled and Nanocomposite Polymer Materials, Vol. 661*, Warrendale, PA, 2001. Materials Research Society Symposium Proceedings, MRS.

[9] M. Avella, M. E. Errico, S. Martelli, and E. Martuscelli. Preparation methodologies of polymer matrix nanocomposites. *Applied Organometallic Chemistry*, 15:435–439, 2001.

[10] H. R. Azimi, R. A. Pearson, and R. W. Hertzberg. Role of crack tip shielding mechanisms in fatigue of hybrid epoxy composites containing rubber and solid glass spheres. *Journal of Applied Polymer Science*, 58:449–463, 1995.

[11] M. Baiardo, E. Zini, and M. Scandola. Flax fibre-polyester composites. *Composites Part A: Applied Science and Manufacturing*, 35:703–710, 2004.

[12] V. Balakrishna. Influence of alumina particle additions on the mechanical properties and fracture features of glass-epoxy composites. *Journal of Materials Science Letters*, 11:1154–1156, 1992.

[13] F. Bauer, V. Sauerland, H.-J. Glaesel, H. Ernst, M. Findeisen, E. Hartmann, H. Langguth, B. Marquardt, and R. Mehnert. Preparation of scratch and operation resistant to polymeric nanocomposites by monomer grafting onto nanoparticles,3a effect of filler particles and grafting agents. *Macromolecular Materials and Engineering*, 287:546–552, 2002.

[14] C. M. Bertelsen and F. J. Boerio. Linking mechanical properties of silanes to their chemical structure: An analytical study of γ-gps solutions and films. In K. L. Mittal, editor, *Silanes and Other Coupling Agents: Volume 2*, chapter 1, pages 41–54. VSP BV, Utrecht, Netherlands, 2000.

[15] Y. Brechet, J. Y. Cavaille, E. Chabert, L. Chazeau, R. Denievel, L. Flandin, and C. Gauthier. Polymer based nanocomposites: Effect of filler-filler and filler-matrix interactions. *Advanced Engineering Materials*, v3, n8:571–577, 2001.

[16] D. M. Brewis. Introduction. In D. M. Brewis, editor, *Surface Analysis and Pretreatment of Plastics and Metals*, chapter 1, pages 1–10. Applied Science Publishers Ltd., Englewood, N.J., 1982.

[17] D. Briggs. Chemical analysis of polymer surfaces. In D. M. Brewis, editor, *Surface Analysis and Pretreatment of Plastics and Metals*, chapter 4, pages 73–94. Applied Science Publishers Ltd., Englewood, N.J., 1982.

[18] D. Briggs. *Surface Analysis of Polymers by XPS and Static SIMS*. Cambridge University Press, Cambridge, UK, 1999.

[19] L. G. Britcher, K. Kehoe, and J. G. Matisons. Direct spectroscopic measurements of adsorption of siloxane polymers onto glass fiber surfaces. In K. L. Mittal, editor, *Silanes and Other Coupling Agents: Volume 2*, chapter 1, pages 99–114. VSP BV, Utrecht, Netherlands, 2000.

[20] D. Broek. *Elementary Engineering Fracture Mechanics*. Kluwer Academic Publishers, Boston, 1982.

[21] M. B. Bush. The interaction between a crack and a particle cluster. *International Journal of Fracture*, 88:215–232, 1997.

[22] W. J. Cantwell and A. C. Roulin-Moloney. Fractography and failure mechanisms of unfilled and particulate filled epoxy resins. In A. C. Roulin-Moloney, editor, *Fractography and Failure Mechanisms of Polymers and Composites*, chapter 7, pages 233–290. Elsevier Applied Science, London, 1989.

[23] Y. M. Cao, J. Sun, and D. H. Yu. Preparation and properties of nano-al_2o_3 particles/polyester/epoxy resin ternary composites. *Journal of Applied Polymer Science*, 83:70–77, 2002.

[24] A. Cateni, S. Ignelzi, S. Mollica, S. M. Zebarjad, and A. Lazzeri. Polymer nanocomposites: The effects of surface interactions and particle size on fracture toughness. From: EUROMECH Colloqium 438 - Constitutive

Equations for Polymer Microcomposites; Center for Materials Engineering, http://iki.boku.ac.at/euromech/abstracts/Lazzeri.pdf, 2002.

[25] E. Chabert, R. Dendievel, C. Gauthier, and J. Y. Cavaille. Prediction of the elastic response of polymer based nanocomposites: A mean field approach and a discrete simulation. *Composites Science and Technology*, 64:309–316, 2004.

[26] P. Charoensirisomboon, T. Inoue, S. I. Solomko, G. M. Sigalov, and M. Weber. Morphology of compatibilized polymer blends in terms of particle size-asphericity map. *Polymer*, 41:7033–7042, 2000.

[27] T. Choudhury and F. R. Jones. The interaction of resole and novolak phenolic resins with γ-aminopropyltriethoxysilane treated e-glass surface: A high resolution xps and micromechanical study. In K. L. Mittal, editor, *Silanes and Other Coupling Agents: Volume 2*, chapter 1, pages 79–97. VSP BV, Utrecht, Netherlands, 2000.

[28] Dow Corning. Silanes chemistry primer. Dow Corning Website: www.dow.com, 2003.

[29] Dow Corning. Dow liquid epoxy resins. Dow Corning Website: www.dow.com/epoxy/products/p-liquid.htm, 2004.

[30] ASTM D5045. Standard test method for plane-strain fracture toughness and strain energy release rate of plastic materials. *Annual Book of ASTM Standards*, Vol. 08.03:352–360, 2002.

[31] ASTM D638. Standard test method for tensile properties of plastics. *Annual Book of ASTM Standards*, Vol. 08.01:46–59, 2002.

[32] I. M. Daniel and O. Ishai. *Engineering Mechanics of Composite Materials.* Oxford University Press, Oxford, 1994.

[33] M. E. J. Dekkers and D. Heikens. Stress analysis near the tip of a curvilinear interfacial crack between a rigid spherical inclusion and a polymer matrix. *Journal of Materials Science*, 20:3865–3872, 1985.

[34] W. Doll. Fractography and failure mechanisms of amorphous thermoplastics. In A. C. Roulin-Moloney, editor, *Fractography and Failure Mechanisms of Polymers and Composites*, chapter 10, pages 387–436. Elsevier Applied Science, London, 1989.

[35] J. B. Donnet. Nano and microcomposites of polymers elastomers and their reinforcement. *Composites Science and Technology*, 63:1085–1088, 2003.

[36] E. Dorre and H. Hubner. *Alumina: Processing, Properties, and Applications.* Springer-Verlag, Berlin, 1984.

[37] ASTM E399. Standard test method for plane-strain fracture toughness of metallic materials. *Annual Book of ASTM Standards*, Vol. 03.01:451–482, 2002.

[38] C. A. Harper (ed.). *Handbook of Ceramics, Glasses and Diamonds: Advanced Ceramics and Composites*, chapter 4, pages 4.1–4.46. McGraw Hill, New York, 2001.

[39] T. Eklund, J. Backman, P. Idman, A. E. E. Norstrom, and J. B. Rosenholm. Investigation of the adsorption of mono- and bifunctional silanes from toluene onto porous silica particles and from aqueous solutions onto e-glass fibers. In K. L. Mittal, editor, *Silanes and Other Coupling Agents: Volume 2*, chapter 1, pages 55–78. VSP BV, Utrecht, Netherlands, 2000.

[40] F. Ellyin. *Fatigue Damage, Crack Growth and Life Prediction.* Chapman & Hall, London, 1997.

[41] D. Ensminger. *Ultrasonics: The Low- and High-Intensity Applications.* Marcel Dekker, Inc., New York, 1973.

[42] A. G. Evans. Strength of brittle materials containing second phase dispersions. *Philosophical Magazine*, 26 (6):1327–, 1972.

[43] M.J. Folkes. *Short Fibre Reinforced Thermoplastics.* Research Studies Press, Chichester, U.K., 1982.

[44] F. M. Fowkes. Dispersion of ceramic powders in organic media. In G. L. Messing, K.S. Mazdiyansni, J. W. McCauley, and R. A. Haber, editors, *Advances in Ceramics, Vol. 21: Ceramic Powder Science*, chapter 3, pages 411–422. The American Ceramic Society, Inc., Westerville, Ohio, 1987.

[45] J. R. Fried. *Polymer Science and Technology.* Prentice Hall, New Jersey, 1995.

[46] J. O. Glanville. *General Chemistry for Engineers.* Prentice Hall, Upper Saddle River, N.J., 2001.

[47] D. J. Green, P. S. Nicholson, and J. D. Embury. Crack shape studies in brittle porous materials. *Journal of Materials Science*, 12 (5):987–989, 1977.

[48] M. Green, T. Kramer, M. Parish, J. FOx, R. Lalananadham, W. Rhine, S. Barclay, P. Calvert, and H. K. Bowen. Chemically bonded organic dispersants. In G. L. Messing, K.S. Mazdiyansni, J. W. McCauley, and R. A. Haber, editors, *Advances in Ceramics, Vol. 21: Ceramic Powder Science*, chapter 3, pages 449–466. The American Ceramic Society, Inc., Westerville, Ohio, 1987.

[49] W. Gutowski, S. Li, L. Russell, C. Filippou, P. Hoobin, and S. Petinakis. Effect of suface-grafted molecular brushes on the adhesion performance of bonded polymers and composite interfaces. *Composite Interfaces*, 9(1):89–133, 2002.

[50] B. S. Hayes, M. Nobelen, A. K. Dharia, J. C. Seferis, and J. Nam. Development and analysis of nano-particle modified prepreg matrices. In *33rd International SAMPE Technical Conference; Advancing Affordable Materials Technology.*, Seattle, WA, United States, November 5-8 2001. International-SAMPE-Technical-Conference. v 33 2001, p 1050-1059, SAMPE.

[51] Andreas Heilmann. *Polymer Films with Embedded Metal Nanoparticles.* Springer, Berlin, 2001.

[52] R. Hogg. Flocculation phenomenon in fine particle dispersions. In G. L. Messing, K.S. Mazdiyansni, J. W. McCauley, and R. A. Haber, editors, *Advances in Ceramics, Vol. 21: Ceramic Powder Science*, chapter 3, pages 467–481. The American Ceramic Society, Inc., Westerville, Ohio, 1987.

[53] Y. Hu. *Multiaxial Behavior and Viscoelastic Constitutive Modeling of Epoxy Polymers.* PhD thesis, University of Alberta, Edmonton, Alberta, 2002.

[54] A. Y. Huang and J. C. Berg. Gelation of liquid bridges in spherical agglomeration. *Colloids and Surfaces A*, 215:241–252, 2003.

[55] T. Hueckel, B. Loret, and A. Gajo. Expansive clays as two-phase, deformable, reactive continua: Concepts and modeling options. In Di Maio, Hueckel, and Loret, editors, *Chemo-Mechanical Coupling in Clays; From Nano-scale to Engineering Applications*, chapter 2, pages 105–120. Swets & Zeitlinger, Lisse, 2002.

[56] J. Y. Huh, J. P. Parakka, and D. E. Nikles. Use of silane coupling agents as dispersion promoters for iron particles in solventless magnetic tape coating formulations. In K. L. Mittal, editor, *Silanes and Other Coupling Agents: Volume 2*, chapter 1, pages 141–148. VSP BV, Utrecht, Netherlands, 2000.

[57] M. Hussain, A. Nakahira, and K. Niihara. Mechanical property improvement of carbon fiber reinforced epoxy composites by al_2o_3 filler dispersion. *Materials Letters*, 26 (3):185–191, 1996.

[58] H. F. Irving and R. L. Saxton. Mixing of high viscosity materials. In V. W. Uhl and J. B. Gray, editors, *Mixing: Theory and Practice*, chapter 8, pages 192–197. Academic Press, New York and London, 1967.

[59] R. O. James. Characterization of colloids in aqueous systems. In G. L. Messing, K.S. Mazdiyansni, J. W. McCauley, and R. A. Haber, editors, *Advances in Ceramics, Vol. 21: Ceramic Powder Science*, chapter 3, pages 349–410. The American Ceramic Society, Inc., Westerville, Ohio, 1987.

[60] B. Z. Jang. *Advanced Polymer Composites: Principles and Applications.* ASM International, Materials Park, OH, 1994.

[61] D. D. Johnson and H. G. Sowman. Ceramic fibres. In C. A. Dostal, editor, *Engineered Materials Handbook. Vol. 1: Composites*, chapter 1, pages 192–197. ASM International, Metals Park, Ohio, 1988.

[62] R. E. Johnson and W. H. Morrison. Ceramic powder dispersion in non-aqueous systems. In G. L. Messing, K.S. Mazdiyansni, J. W. McCauley, and R. A. Haber, editors, *Advances in Ceramics, Vol. 21: Ceramic Powder Science*, chapter 3, pages 323–348. The American Ceramic Society, Inc., Westerville, Ohio, 1987.

[63] D. Karpuzov. X - ray photoelectron spectroscopy (xps). ACSES Website, Chemical and Material Engineering, University of Alberta, www.ualberta.ca/ ACSES/ACSES2/ XPS.htm, 2003.

[64] A. K. Kaw. *Mechanics of Composite Materials.* CRC Press, Boca Raton, 1997.

[65] G. Kickelbick. Concepts for the incorporation of inorganic building blocks into organic polymers on a nanoscale. *Progress in Polymer Science*, 28:83–114, 2003.

[66] G. Kickelbick and U. Schubert. Organic functionalization of metal oxide nanoparticles. In M. I. Baraton, editor, *Synthesis, Functionalization and Surface Treatment of Nanoparticles*, chapter 6, pages 91–102. American Scientific Publishers, Stevenson Ranch, California, USA, 2003.

[67] G. M. Kim and D. H. Lee. Feg-esem investigation of micromechanical deformation processes in ultrafine monospherical sio_2 particle-filled polymer composites. *Journal of Applied Polymer Science*, 82:785–789, 2001.

[68] G. M. Kim, D. H. Lee, B. Hoffmann, J. Kressler, and G. Stoppelmann. Influence of nanofillers on the deformation process in layered silicate/polyamide-12 nanocomposites. *Polymer*, 42:1095–1100, 2001.

[69] Y. K. Kim, A. F. Lewis, S. B. Warren, P. K. Patra, P. Calvert, P. Singhal, S. Kota, D. Nam, Y. Yoshioka, W. Kelsey, and C. Harjanto. Nanocomposite fibers. National Textile Center Annual Report: http://www.ntcresearch.org/pdf-rpts/AnRp00/m00-d08.pdf, 2001.

[70] W. D. Kingery, H. K. Bowen, and D. R. Uhlmann. *Introduction to Ceramics.* John Wiley & Sons, New York, 1976.

[71] X. Kornmann. Polymer - layered silicate nanocomposites. Internet at: www.insmat.co.uk /iom/oranisations/ escm/newsletter4/ nanocomposites.pdf Contact at: xavier. kornmann@empa.ch (Switzerland), 2003.

[72] F. D. Kuchta, P. J. Lemstra, A. Keller, L. F. Batenburg, and H. R. Fischer. Materials with improved properties from polymer-ceramic nanocomposites. In *Organic/Inorganic Hybrid Materials II, Vol. 576*, San Francisco, California, April 1999. Materials Research Society Symposium Proceedings, MRS.

[73] K. A. Kusters, S. E. Pratsinis, S. G. Thoma, and D. M. Smith. Ultrasonic fragmentation of agglomerate powders. *Chemical Engineering Science*, 48(24):4119–4127, 1993.

[74] K. A. Kusters, S. E. Pratsinis, S. G. Thoma, and D. M. Smith. Energy-size reduction laws for ultrasonic fragmentation. *Powder Technology*, 80:253–263, 1994.

[75] C. C. Landry, N. Pippe, M. R. Mason, A. W. Apblett, A. N. Tyler, A. N. MacInnes, and A. R. Barron. From minerals to materials: Synthesis of alumoxanes from the reaction of boehmite with carboxylic acids. *Journal of Material Chemistry*, v5, n2:331–341, 1995.

[76] F. F. Lange. Interaction of a crack front with a second-phase dispersion. *Philosophical Magazine*, 22 (179):983–, 1970.

[77] K. Lau, S. Shi, and H. Cheng. Micro-mechanical properties and morphological observation on fracture surfaces of carbon nanotube composites pre-treated at different temperatures. *Composites Science and Technology*, 63:1161–1164, 2003.

[78] B. Lawn. *Fracture of Brittle Solids.* Cambridge University Press, Cambridge, 1993.

[79] M. G. Lazarraga, J. Ibanez, M. Tabellout, and J. M. Rojo. On the aggregation process of ceramic $LiSn_2P_3O_{12}$ particles embedded in teflon matrix. *Composite Science and Technology*, 64:759–765, 2004.

[80] C. S. Lee, J. S. Lee, and S. T. Oh. Dispersion control of fe_2o_3 nanoparticles using a mixed type of mechanical and ultrasonic milling. *Materials Letters*, 4215:1–4, 2002.

[81] J. Lee and A. F. Yee. Inorganic particle toughening i: Micro-mechanical deformations in the fracture of glass bead filled epoxies. *Polymer*, 42:577–588, 2001.

[82] J. Lee and A. F. Yee. Inorganic particle toughening ii: Toughening mechanisms of glass bead filled epoxies. *Polymer*, 42:589–597, 2001.

[83] Chingshen Li and F. Ellyin. Short crack trapping/untrapping in particle-reinforced metal-matrix composites. *Composite Science and Technology*, 52:117–123, 1994.

[84] D. Li, X. Zhang, G. Sui, D. Wu, J. Liang, and X. Yi. Toughness improvement of epoxy by incorporating carbon nanotubes into the resin. *Journal of Materials Science Letters*, 22:791–793, 2003.

[85] D. Lin-Vien, N. B. Colthup, W. G. Fateley, and J. G. Grasselli. *The Handbook of Infared and Ramen Characteristic Frequencies of Organic Molecules.* Academic Press, Boston, 1999.

[86] K. Lozano and E. V. Barrera. Nanofiber-reinforced thermoplastic composites. i. thermoanalytical and mechanical analyses. *Journal of Applied Polymer Science*, 79:125–133, 2001.

[87] R. R. Maccani. Characteristics crucial to the application of engineering plastics. In C. A. Dostal, editor, *Engineered Materials Handbook. Vol. 2: Engineering Plastics*, chapter 2, pages 68–73. ASM International, Metals Park, Ohio, 1988.

[88] I. J. McColm. *Ceramic Science for Materials Technologists.* Leonard Hill, New York, 1983.

[89] Wayne Moffat. Personal communication with; Spectral Services, June 2004.

[90] R. J. Morgan and J. E. O'Neal. Structural parameters affecting the brittlenss of polymer glasses and composites. In R. D. Deanin and A. M. Crugnola, editors, *Toughness and Brittleness of Plastics*, chapter 2, pages 8–16. American Chemical Society, Atlantic City, N.J., 1976.

[91] T. M. Mower and A. S. Argon. Experimental investigations of crack trapping in brittle heterogeneous solids. *Mechanics of Materials*, 19:343–364, 1995.

[92] J. W. Muskopf. *Ullmann's Encyclopedia of Industrial Chemistry (Online).* Wiley - VCH Verlag GmbH & Co., KGaA, www.mrw. interscience.wiley.com/ ueic/articles/a09_547, June 15, 2000.

[93] J. A. Nairn. Fracture mechanics of composites with residual stresses, traction-loaded cracks, and imperfect interfaces. *Journal of Applied Mechanics*, 64:804–810, 1997.

[94] C. B. Ng, L. S. Schadler, and R. W. Siegel. Synthesis and mechanical properties of tio_2-epoxy nanocomposites. *NanoStructured Materials*, 12:507–510, 1999.

[95] L. Nicolais and M. Narkis. *Polymer Engineering and Science*, 11:194, 1971.

[96] L. E. Nielsen. Simple theory of stress-strain properties of filled polymers. *Journal of Applied Polymer Science*, 10:97, 1966.

[97] L. E. Nielsen and R. F. Landel. *Mechanical Properties of Polymers and Composites.* Marcel Dekker, New York, 1994.

[98] D. A. Norman and R. E. Richardson. Rigid-particle toughening of glassy polymers. *Polymer*, 44:2351–2362, 2003.

[99] M. V. Parish, R. R. Garcia, and H. K. Bowen. Dispersion of oxide powders in organic liquids. *Journal of Materials Science*, 20:996–1008, 1985.

[100] M. R. Piggott and J. Leidner. Misconceptions about filled polymers. *Journal of Applied Polymer Science*, 18:1619, 1974.

[101] C. Pirlot, I. Willems, A. Fonseca, J. B. Nagy, and J. Dehalle. Preparation and characterization of carbon nanotubes/polyacrylonitrile composites. *Advanced Engineering Materials*, 4(3):109–114, 2002.

[102] E. P. Plueddemann. Present status and research needs in silane coupling. In H. Ishida, editor, *Interfaces in Polymer, Ceramic and Metal Matrix Composites*, chapter 1, pages 17–34. Elsevier, New York, 1988.

[103] Resolution Performance Products. Resin system for filament winding and rtm. www.resins.com, 2003.

[104] J. Y. Qian, R. A. Pearson, V. L. Dimonie, and M. S. El-Aasser. Synthesis and application of core-shell particles as toughening agents for epoxies. *Journal of Applied Polymer Science*, 58:439–448, 1995.

[105] Jr. R. D. Nelson. *Dispersing Powders in Liquids.* Elsevier, New York, 1988.

[106] D. G. Rance. Thermodynamics of wetting: From its molecular basis to technological application. In D. M. Brewis, editor, *Surface Analysis and Pretreatment of Plastics and Metals*, chapter 6, pages 121–152. Applied Science Publishers Ltd., Englewood, N.J., 1982.

[107] W. Ranney, S. E. Berger, and J. G. Marsden. Silane coupling agents in particulate mineral filled composites. In E. P. Plueddemann, editor, *Composite Materials, Vol. 6: Interfaces in Polymer Matrix Composites*, chapter 5, pages 135–147. Academic Press, New York and London, 1974.

[108] Y. Rao, A. Takahashi, and C. P. Wong. Di-block copolymer surfactant study to optimize filler dispersion in high dielectric constant polymer-ceramic composite. *Composites Part A: Applied Science and Manufacturing*, 34:1113–1116, 2003.

[109] M. Ratzsch. The influence of the interface in polymer composites. In H. Ishida, editor, *Interfaces in Polymer, Ceramic and Metal Matrix Composites*, chapter 4, pages 425–432. Elsevier, New York, 1988.

[110] J. S. Reed. *Introduction to the Principles of Ceramic Processing.* John Wiley & Sons, New York, 1988.

[111] B. W. Rosen and N. F. Dow. Overview of composite materials analysis and design. In C. A. Dostal, editor, *Engineered Materials Handbook. Vol. 1: Composites*, chapter 4, pages 175–181. ASM International, Metals Park, Ohio, 1988.

[112] H. Rotstein and R. Tannenbaum. Polymer metal nanocluster composites. In M. I. Baraton, editor, *Synthesis, Functionalization and Surface Treatment of Nanoparticles*, chapter 7, pages 103–125. American Scientific Publishers, Stevenson Ranch, California, USA, 2003.

[113] J. G. Ryu, P. S. Lee, H. Kim, and J. W. Lee. Ultrasonic degradation of polypropylene and its application for the development of pp based copolymer and nanocomposite. *Korea-Australia Rheology Journal*, v13, n2:61–65, 2001.

[114] C. Sanchez, G. J. de A. A. Soler-Illia, F. Ribot, T. Lalot, C. R. Mayer, and V. Cabuil. Reviews: Designed hybrid organic-inorganic nanocomposites from functional nanobuilding blocks. *Chemistry of Materials*, v13, n10:3074–3076, 2001.

[115] J. C. Santamarina, K. A. Klein, A. Palomino, and M. S. Guimaraes. Micro-scale aspects of chemical-mechanical coupling: Interparticle forces and fabric. In Di Maio, Hueckel, and Loret, editors, *Chemo-Mechanical Coupling in Clays; From Nano-scale to Engineering Applications*, chapter 1, pages 47–60. Swets & Zeitlinger, Lisse, 2002.

[116] S. H. Schaafsma, P. Vonk, P. Segers, and N. W. F. Kossen. Description of agglomerate growth. *Powder Technology*, 97:183–190, 1998.

[117] H. Schmidt. Nanoparticles by chemical synthesis, processing to materials and innovative applications. *Applied Organometallic Chemistry*, 15:331–343, 2001.

[118] H. K. Schmidt, M. Mennig, R. Nonninger, P. W. Oliveira, and H. Schirra. Organic-inorganic hybrid materials processing and applications. In *Organic/Inorganic Hybrid Materials II, Vol. 576*, San Francisco, California, April 1999. Materials Research Society Symposium Proceedings, MRS.

[119] D. J. Shanefield. *Organic Additives and Ceramic Processing: With Applications in Powder Metallurgy, Ink and Paint.* Kluwer Academic Publishers, Boston, 1995.

[120] D. Shi, S. X. Wang, W. J. van Ooij, L. M. Wang, J. G. Zhao, and Z. Yu. Uniform deposition of ultra-thin polymer films on the surfaces of al_2o_3 nanoparticles by a plasma treatment. *Applied Physics Letters*, 78 (9):1243, 2001.

[121] G. M. Sigalov, J. Ibuki, T. Chiba, and T. Inoue. Method of effective ellipses for digital image analysis of size, shape, orientation, and interparticle distances in polymer blends: Application to a study of polyamide 6/polysulfone reactive blending. *Macromolecules*, 30:7759–7767, 1997.

[122] Sigma-Aldrich. Product information: Ftir - condensed phase. Internet at: www.sigmaaldrich.com (Aldrich products #440167, #104884), October, 2003.

[123] R. P. Singh, M. Zhang, and D. Chan. Toughening of a brittle thermosetting polymer: Effects of reinforcement particle size and volume fraction. *Journal of Materials Science*, 37:781–788, 2002.

[124] P. Somasundaran and T. Chen. Nanocomposite particles for the preparation of advanced nanomaterials. In *Surface Controlled Nanoscale Materials for High Value Added Applications, Vol. 501, 1997 Fall Symposium: Boston, MA*, Warrendale, PA, 1998. Materials Research Society Symposium Proceedings, MRS.

[125] S. S. Sternstein and J. Rosenthal. A flaw spectrum theory for multiple flaw failure in solid polymers. In R. D. Deanin and A. M. Crugnola, editors, *Toughness and Brittleness of Plastics*, chapter 4, pages 35–42. American Chemical Society, Atlantic City, N.J., 1976.

[126] H.J. Sue, P.M. Puckett, and J.L. Bertram. Toughening of engineering thermosets via new toughening mechanisms; v 69-1 p 277-284. In *Proceedings of the 1995 ASME International Mechanical Engineering Congress and Exposition. Part 1 (of 2). San Francisco, CA, USA*, New York, NY, USA, 1995. ASME Materials Division, ASME.

[127] C. T. Sun and H. Zhang. Size-dependent elastic constants of materials at nano scale. *Journal of Applied Physics*, v93, n2:1212–1218, 2003.

[128] J. Sung and P. S. Nicholson. Inclusion-initiated fracture model for ceramics. *Journal of the American Ceramic Society*, 73:639–644, 1990.

[129] K. S. Suslick and G. J. Price. Applications of ultrasound to materials chemistry. *Annual Reviews of Materials Science*, 29:295–326, 1999.

[130] F. Tepper. Nano size alumina fibers (html). Argonide Corporation document, Found on the internet in 2002 at: www.argonide.com/ ceramic_fibres.html, 2001.

[131] F. Tepper. Nano size alumina fibers (pdf). Updated Argonide Corporation document containing more extensive information. Found on the internet in 2004 at: www.argonide.com/ particles2001.pdf, 2001.

[132] S. G. Thoma, M. Ciftcioglu, and D. M. Smith. Determination of agglomerate strength distributions, part 1. calibration via ultrasonic forces. *Powder Technology*, 68:53–61, 1991.

[133] G. G. Tibbetts and J. J. McHugh. Mechanical properties of vapor-grown carbon fiber composites with thermoplastic matrices. *Journal of Materials Research*, 14:2871–2880, 1999.

[134] J. Tirosh, W. Nachlis, and D. Hunston. Strength behavior of toughened polymers by fibrous (or particulate) elastomers. *Mechanics of Materials*, 19:329–342, 1995.

[135] E. Vassileva and K. Friedrich. Epoxy/alumina nanoparticle composites. 1. dynamic mechanical behavior. *Journal of Applied Polymer Science*, 89:3774–3785, 2003.

[136] C. R. Veale. *Fine Powders: Preparation, Properties and Uses.* Applied Science Publishers, Ltd., Barking, Essex, England, 1972.

[137] C. T. Vogelson, Y. Koide, , and A. R. Barron. Fibre reinforced epoxy resin composite materials using carboxylate - alumoxanes as cross - linking agents. In *Nanophase and Nanocomposite Materials III, Vol. 581; Nov-Dec. 1999, Boston, MA*, Warrendale, PA, 2000. Materials Research Society Symposium Proceedings, MRS.

[138] C. T. Vogelson, Y. Koide, L. B. Alemany, and A. R. Barron. Inorganic - organic hybrid and composite resin materials using carboxylate - alumoxanes as functionalized cross - linking agents. *Chemistry of Materials*, 12:795–804, 2000.

[139] B. Y. Wei, S. L. Ho, F. Y. Chen, and H. M. Lin. Optimization of process parameters for preparing wo_3/polyacrylonitrile nanocomposites and the associated dispersion mechanism. *Surface and Coating Technologies*, 166:1–9, 2003.

[140] B. Wetzel, F. Haupert, and M. Q. Zhang. Epoxy nanocomposites with high mechanical and tribological performance. *Composite Science and Technology*, 63:2055–2067, 2003.

[141] J. D. Wolodko. *Biaxial Fatigue and Leakage Characteristics of Fibre Reinforced Composite Tubes.* PhD thesis, University of Alberta, Edmonton, Alberta, 1998.

[142] M. Wong, M. Paramsothy, X. J. Xu, Y. Ren, S. Li, and K. Liao. Physical interactions at carbon nanotube-polymer interface. *Polymer*, 44:7757–7764, 2003.

[143] C. L. Wu. Deformation characteristics of nano-silicate filled polypropylene composites. *Polymer and Polymer Composites*, v11, n7:559–562, 2003.

[144] A. F. Yee, W. V. Olszewski, and S. Miller. Plane strain and the brittleness of plastics. In R. D. Deanin and A. M. Crugnola, editors, *Toughness and Brittleness of Plastics*, chapter 8, pages 97–111. American Chemical Society, Atlantic City, N.J., 1976.

[145] A. F. Yee and R. A. Pearson. Fractography and failure mechanisms of rubber modified epoxide resins. In A. C. Roulin-Moloney, editor, *Fractography and Failure Mechanisms of Polymers and Composites*, chapter 8, pages 291–350. Elsevier Applied Science, London, 1989.

[146] J. Zeng, B. Saltysiak, W. S. Johnson, D. A. Schiraldi, and S. Kumar. Composites part b: Engineering. *Surface and Interface Analysis*, 35:173–178, 2004.

[147] J. Zhao. Dispersion of carbon nanotubes and their polymer composites. Unpublished Literature Review, from the University of Cincinnati; www,eng.uc.edu/~gbeaucag/classes/Nanopowders /CarbonBased-NanoPowders/ZhaoCarbonNanoTubeComposite.doc, 2001.

[148] A.J. Zhu and S. S. Sternstein. Nonlinear viscoelasticity of nanofilled polymers: Interfaces, chain statistics and properties recovery kinetics. *Composties Science and Technology*, 63:1113–1126, 2003.

Appendix A

Determination of Required Silane Mass

The surface area covered by one silane molecule is $SA_{molecule} = 0.6\ nm^2$.
The molar mass, MM_{AS}, of the amino-silane is 222 g/mol.
Avogadro's number, AN, is 6.02214 x10^{23}particles/mol.
The surface area of monodispersed alumina, SA_f is $500 - 700$ m^2/g.

The specific surface area covered by the silane, SA_s is given by:

$$SA_s = SA_{molecule}\frac{AN}{MM_{ES}}$$

The mass of silane required, M_s, is given as:

$$M_s = \frac{SA_f M_f}{SA_s}$$

Hence, for the amino-silane, the approximate required mass is:

$$M_s = \frac{\sim 500 M_f}{\sim 1500} \approx 1/3 M_f$$

The calculations for the ethoxy-silane are almost identical; using the molar mass, $MM_{ES} = 236$ g/mol.

Appendix B

Preparation of Silane for Surface Modification

The silanes are stored in airtight glass jars to maintain an oxygen- and water-free environment. These containers were further stored in a desiccating jar with a dry, nitrogen environment. This is seen in Figure B.1, where the silane jars are in red. Nitrogen is supplied to the desiccating jar from an existing nitrogen purging apparatus (Figure B.2)using the plastic hose (arrow) that also is used to pressurize the silane jars during silane removal.

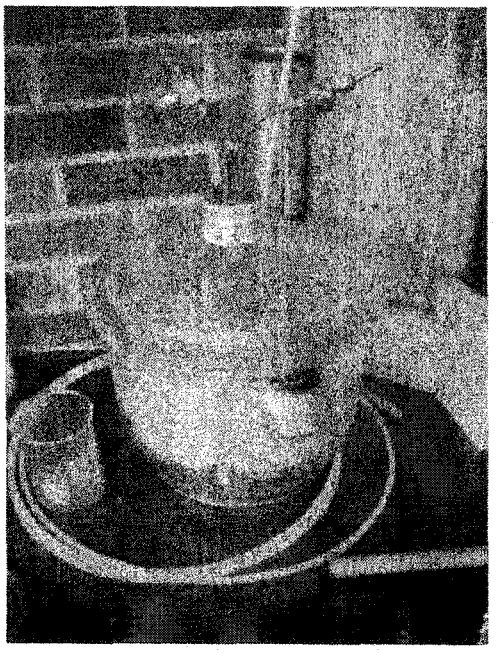

Figure B.1: Storage of the silane containers.

The silane is extracted from the bottles through the rubber septum of the container top. During this procedure, the silane bottle is held in a clamp in the fume hood. A short needle needle, attached to a nitrogen hose, is inserted into the top of the silane jar, through the septum. This needle supplies the dry nitrogen to the jar, to push the silane out. A second, longer, flexible stainless

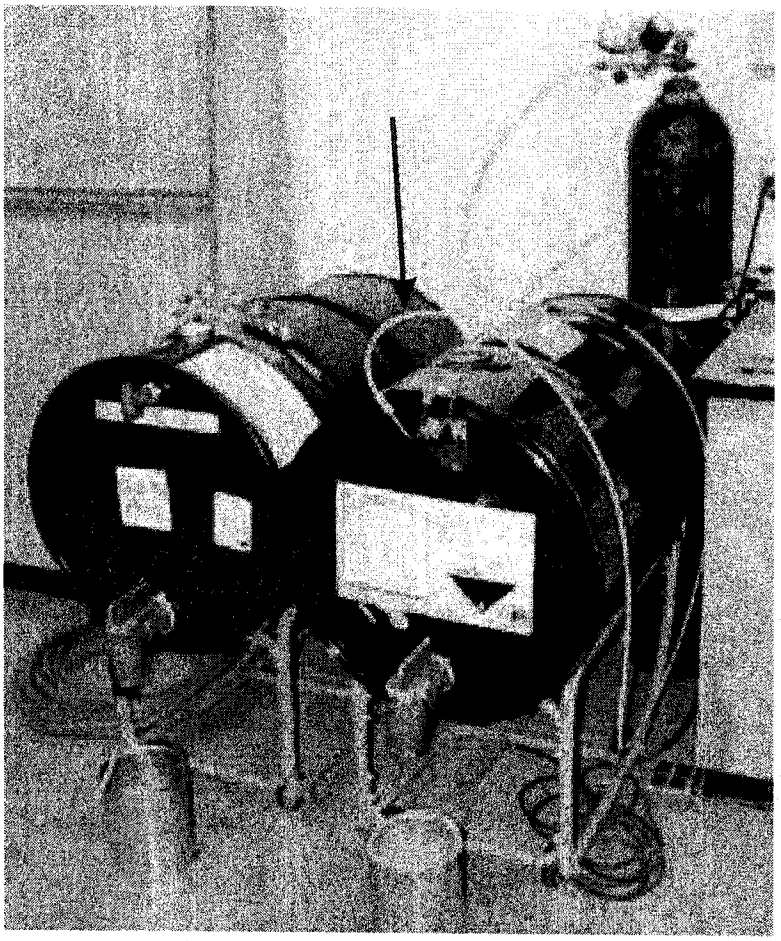

Figure B.2: Barrels containing epoxy and hardener; nitrogen storage, with arrow pointing out plastic distribution tube.

steel needle is then inserted, to which is attached a 10 mL syringe (Luer-lock). The needles are shown in Figure B.3. Prior to insertion, both needles are dryed at a temperature of $> 165°C$ for longer than two hours. Needles are flushed with nitrogen during cooling.

Figure B.3: Needles used for silane extraction.

The silane is drawn from the container into a syringe by supplying nitrogen at a pressure of approximately 5 PSI. Needles are only used for one withdrawal (1 insertion and removal). Needles are held in place using a lab stand with clamps. Care is taken to avoid contact with the silane: gloves, lab coat and organic vapor respirator are worn. Silane is then measured (mass) and put into the mixing container, as shown in Figure B.4. After extraction all tools are cleaned with water, methanol and acetone and allowed to air dry.

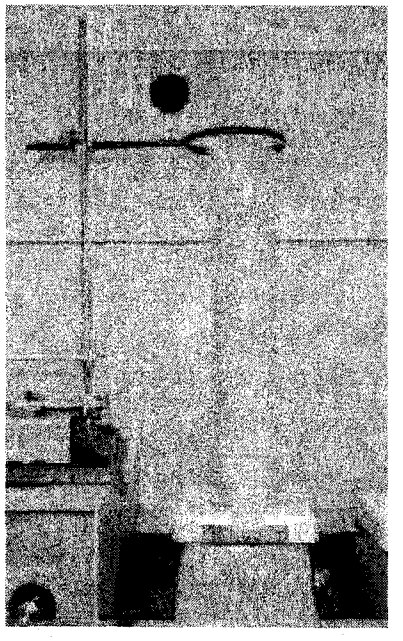

Figure B.4: Example of silane and powder mixing setup.

Appendix C

Digital Analysis of TEM Particle Distribution

Digital analysis was performed using the program Matrox Inspector. TEM images were converted to a 16-bit unsigned format. All images were filtered using the "smooth 5x5" function to sharpen edges and reduce pixel variation. This was monitored using a measurement line drawn across the image, an example of which is found in Figure C.2. This shows dark regions as little pixel values and white regions as high pixel values. This procedure was also done to allow an average background pixel value and an average clump pixel value to be determined.

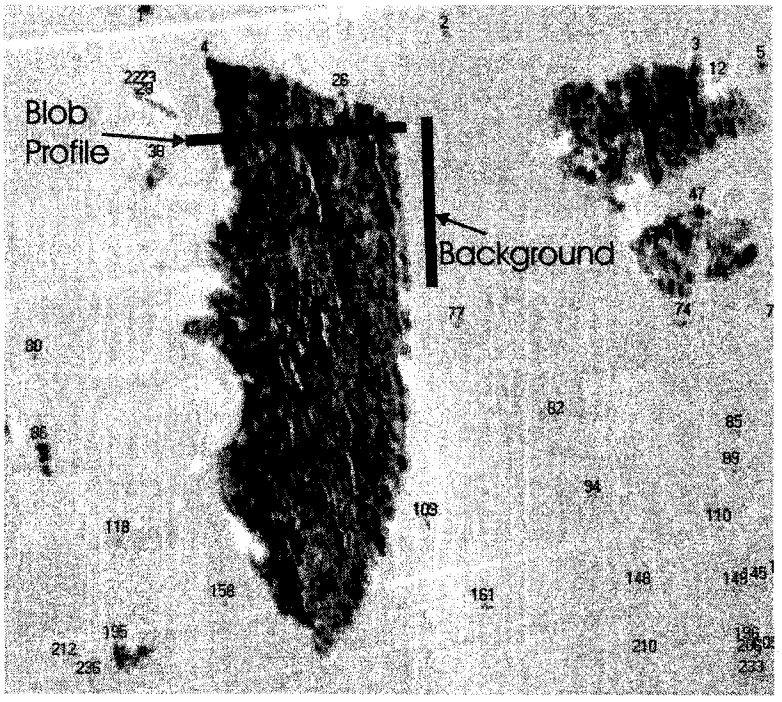

Figure C.1: Example of blob analysis.

A "blob" analysis was conducted, where clumps were considered to be composed of pixels having a grey value below a certain threshold (segmentation

value). With these images, this threshold was set to no greater than 80% of the background value. The difference between clump and background pixel values is illustrated in Figure C.3, where a line test is made across the large clump in Figure C.1. Care was taken to avoid analysis of pictures containing large variations in contrast, for this varied the background pixel values and skewed results by preventing a common segmentation threshold to be used. The clumps touching the edges were not included. A minimum pixel area was used and set at between 10 and 20 pixels. This was done to limit selection of minor variations as clumps. Due to this limitation, based on resolution, the analysis can only detect part of the actual distribution of particles and particle clumps – between the minimum resolution and below the largest clump that fits in the image.

Clumps were numbered and values (area, elongation, average pixel value, etc.) were calculated. This is shown in Figure C.1. Data was exported to Microsoft Excel and area values sorted into the bin ranges used for laser diffraction size determination.

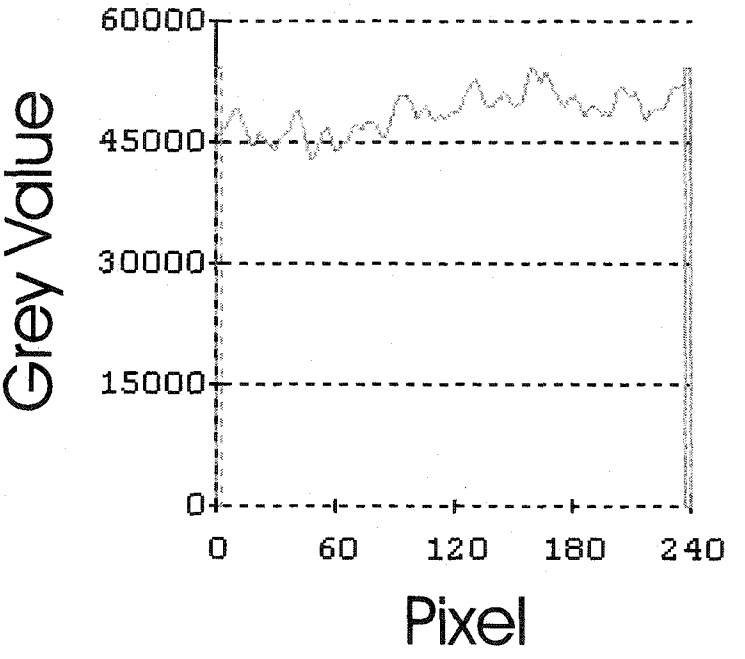

Figure C.2: Background pixel variation along test line. Shown with an arrow in Figure C.1.

Multiple analysis were completed in this fashion and are graphed on one curve (for each specimen) and reflect the general number of clumps of a particular size that exist between the largest of clumps in the specimen. Histograms of the remaining TEM's are found below in Figure C.4, Figure C.5 and Figure C.6.

Since digital analysis was found as a tool subsequent to obtaining all of the images, TEM's were not taken to allow systematic comparison between specimens. Future work should take advantage of this tool, though caution should be employed in its application (as with finite element analysis and other such tools).

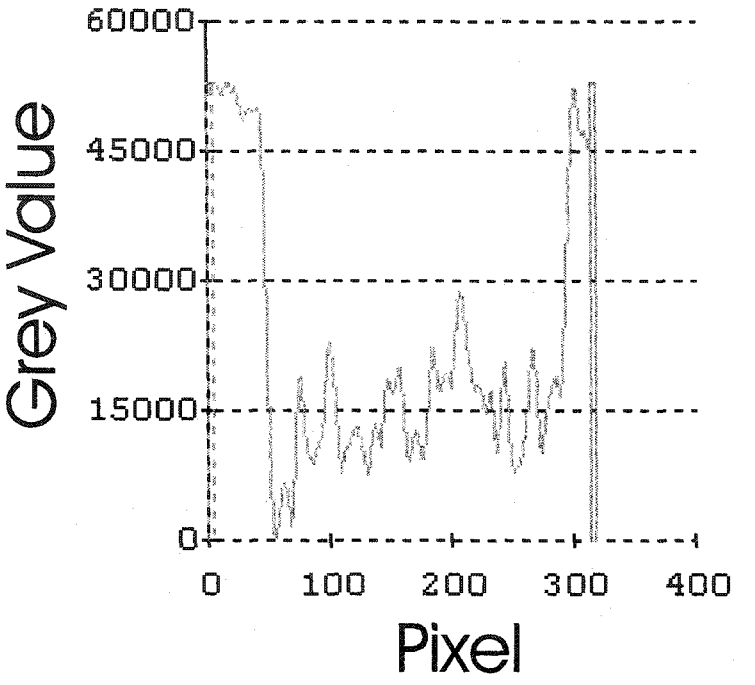

Figure C.3: Pixel variation across clump, using a test line. Low values in the center region indicate a clump.

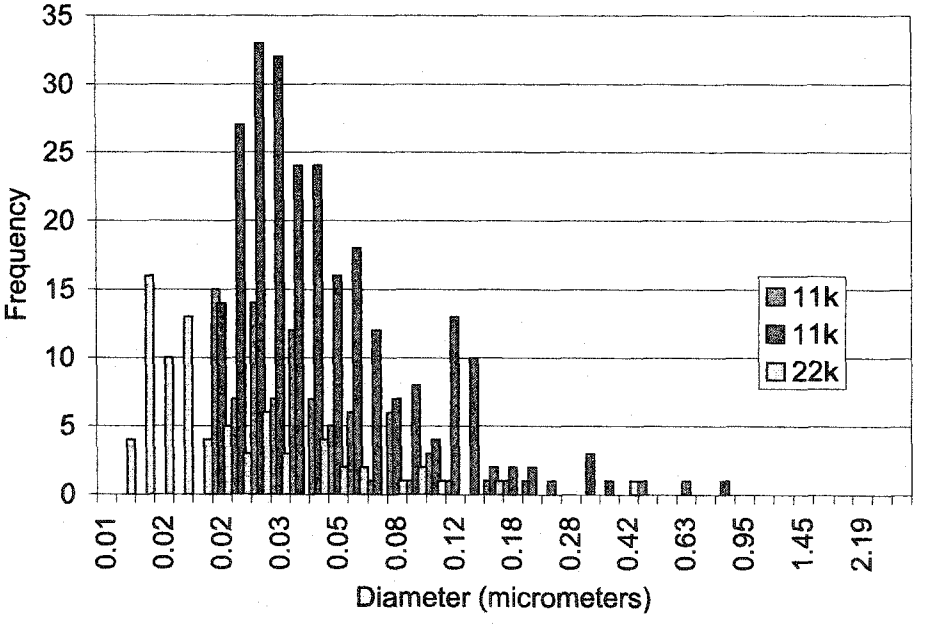

Figure C.4: Histograms of particle size distribution for 2F TEMs.

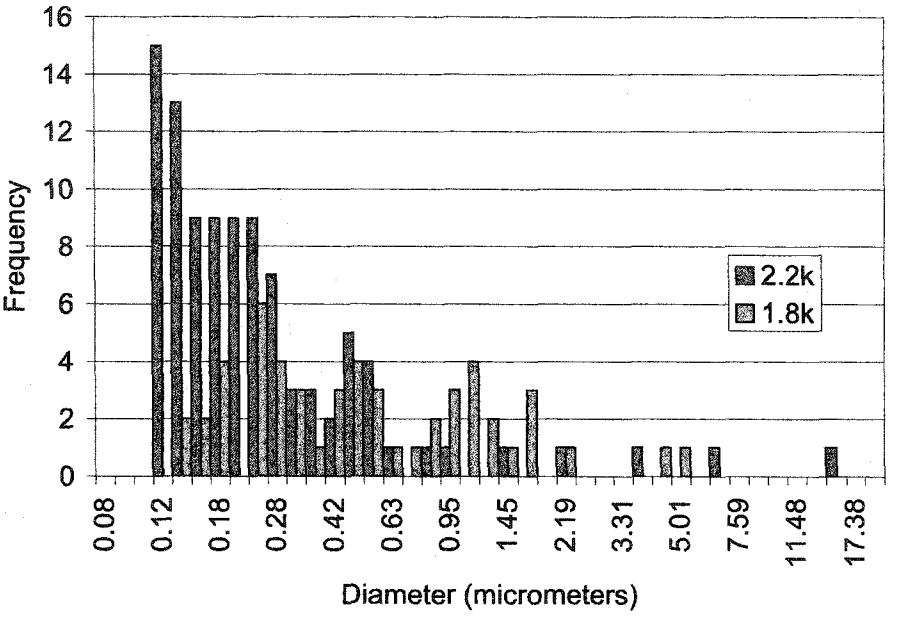

Figure C.5: Histograms of particle size distribution for AF1 TEMs.

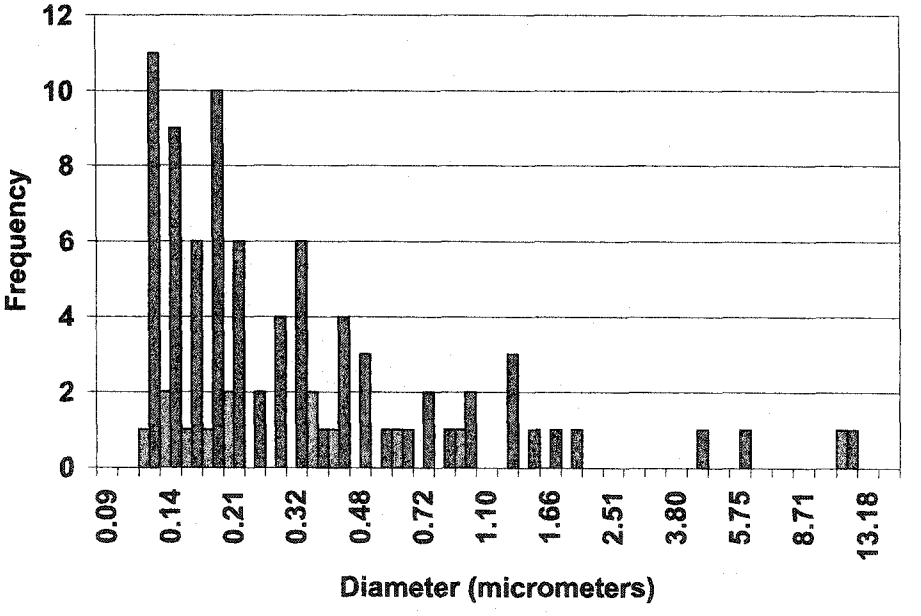

Figure C.6: Histograms of particle size distribution for EF3 TEMs.

Appendix D

Filler Gradient

Cross sections of plate were obtained following manufacture of the specimens, in order to establish the gradient of filler across the plate and through the eventual thickness of test specimens. All the samples were taken perpendicular to the length of the specimens and at the same distance from the plate edge. Samples were "potted" in Cold-Cure epoxy and cured. The potted samples were polished perpendicular to the sample, up to 600 grit, on a circular disk polisher. Disks, with a thickness of approximately 2mm, were cut off the potted samples to allow better light transmission through the sample during imaging. Similar polishing was completed on the back side of the thinly cut sections. These were then scanned at a minimum resolution of $4800x4800$ d.p.i. on a flatbed scanner, with a white background. Visual confirmation of gradient was made and quantification provided with digital analysis, employing the program 'Matrox Inspector'.

Below are images of the scanned sections. Overlayed are pixel values, as described in Appendix C.

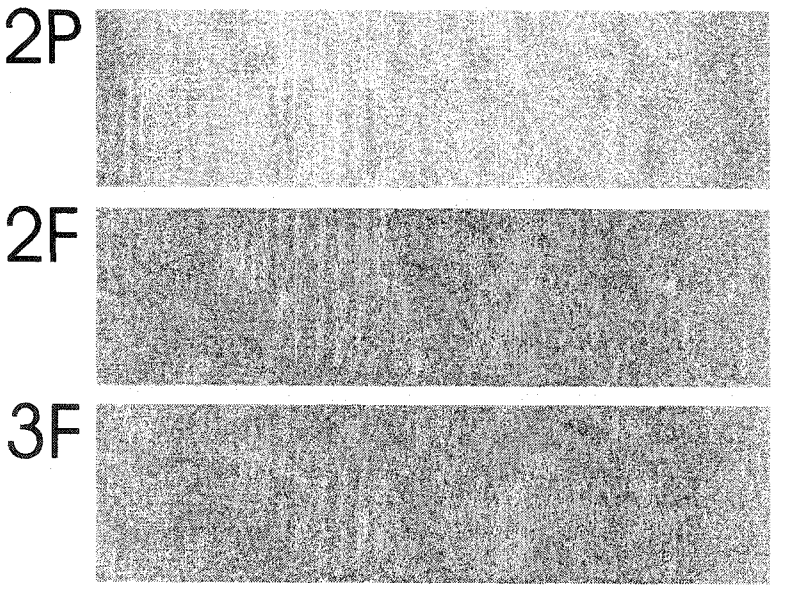

Figure D.1: Scanned sections of Series 2 and 3 specimens.

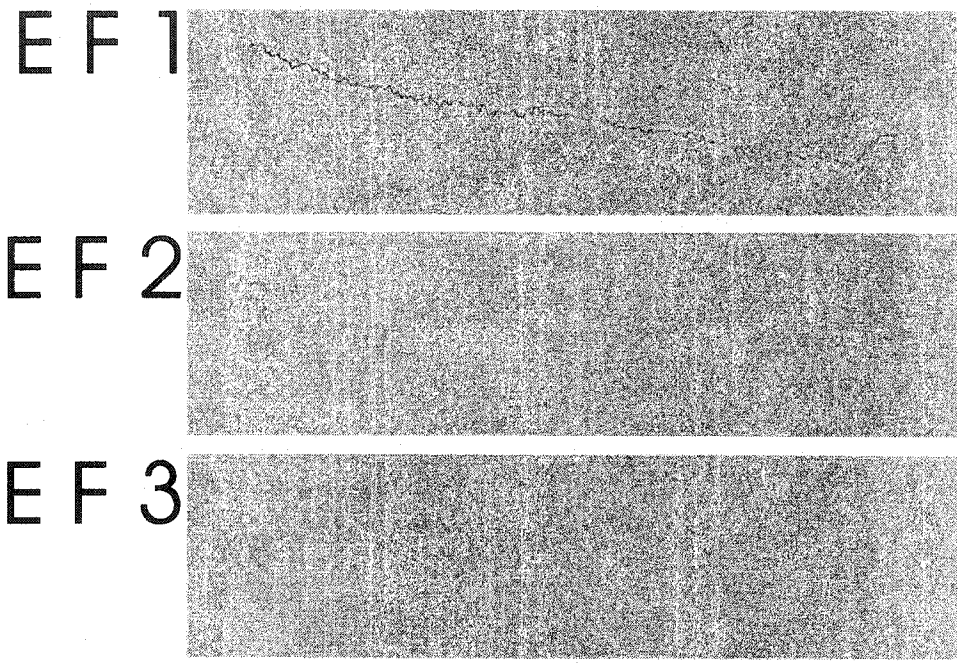

Figure D.2: Scanned sections of EF1, EF2 and EF3 specimens. The bottoms are to the right.

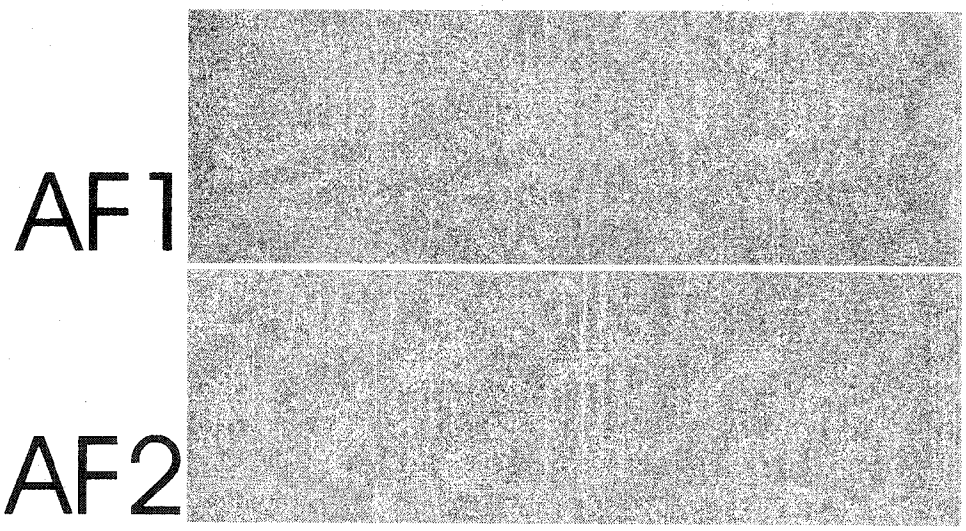

Figure D.3: Scanned sections of AF1 and AF2 specimens.

Appendix E

Load-Displacement Curves for Fracture Testing

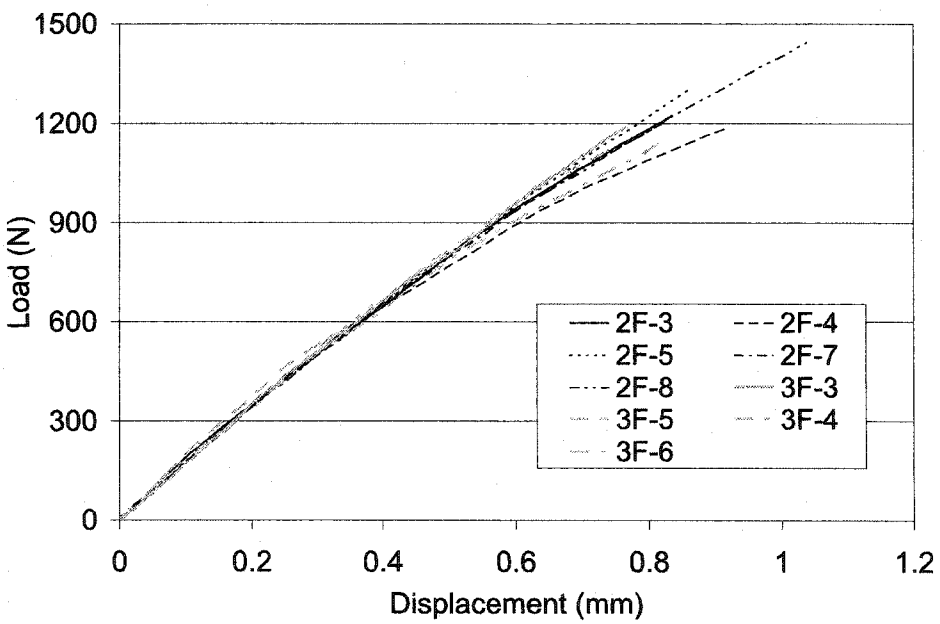

Figure E.1: Fracture load-displacement curves for series 2-3F specimens.

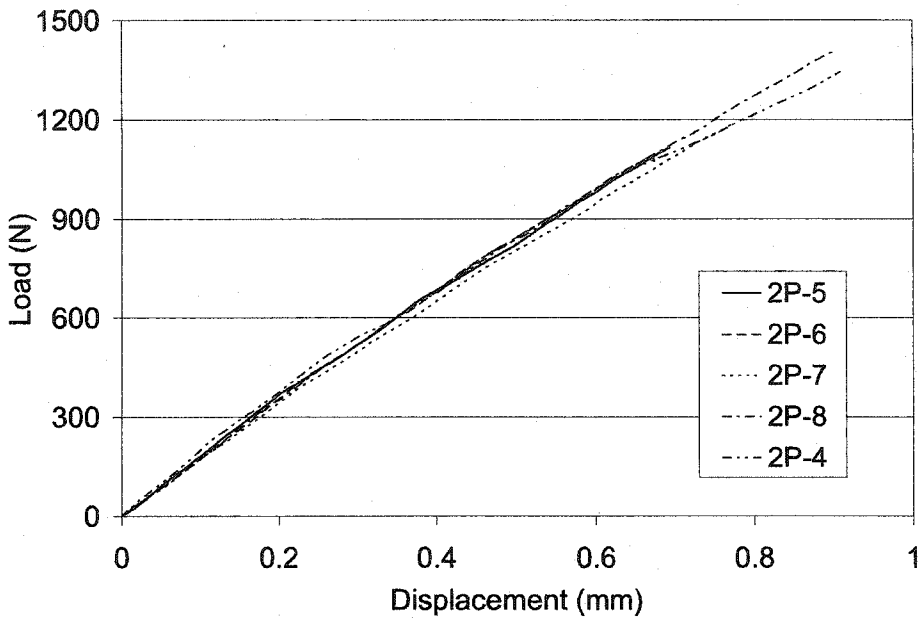

Figure E.2: Fracture load-displacement curves for series 2P specimens.

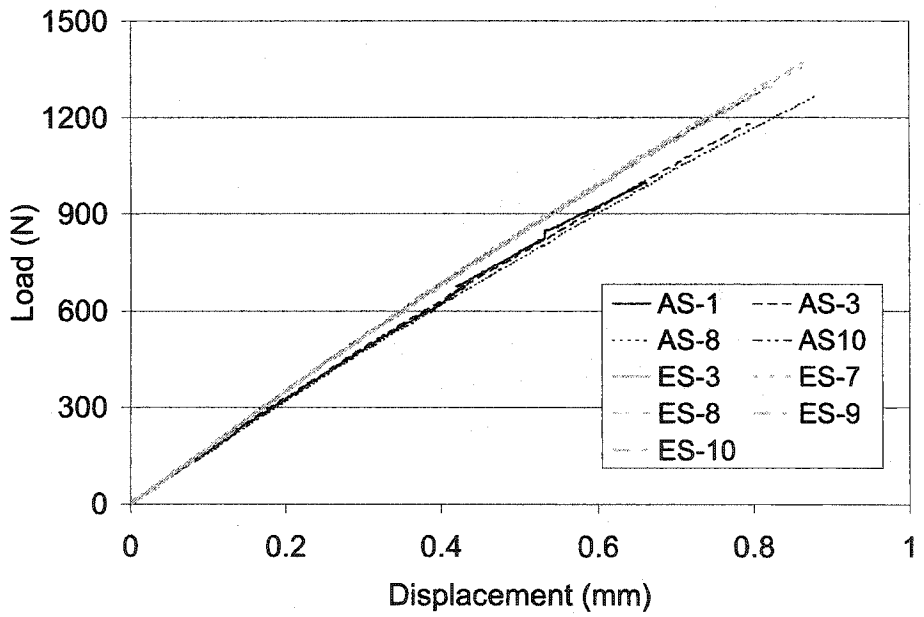

Figure E.3: Fracture load-displacement curves for AS/ES specimens.

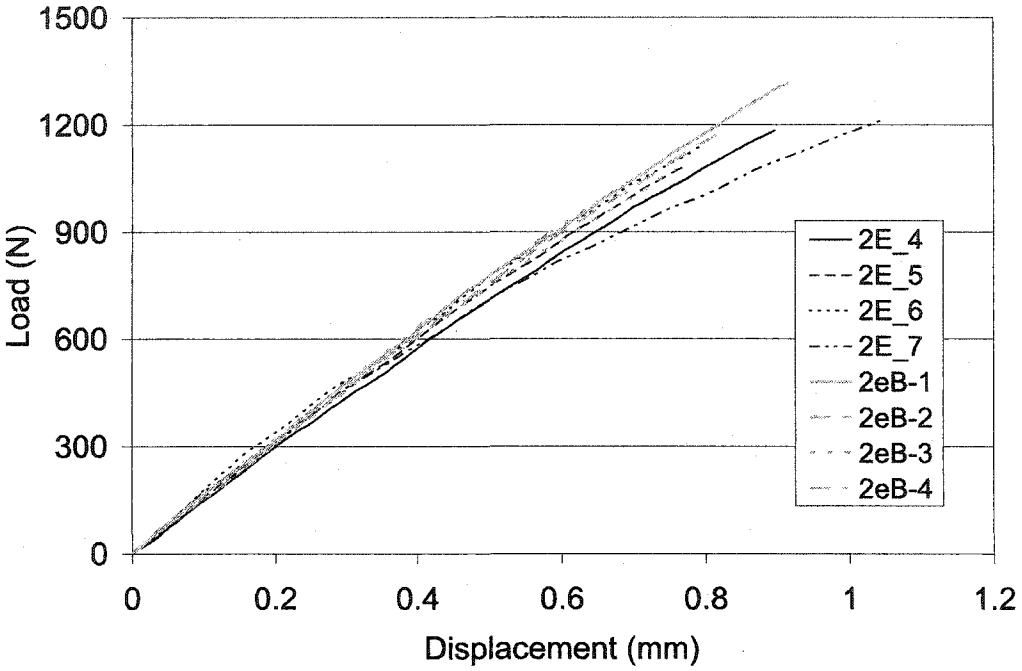

Figure E.4: Fracture load-displacement curves for Epoxy specimens.

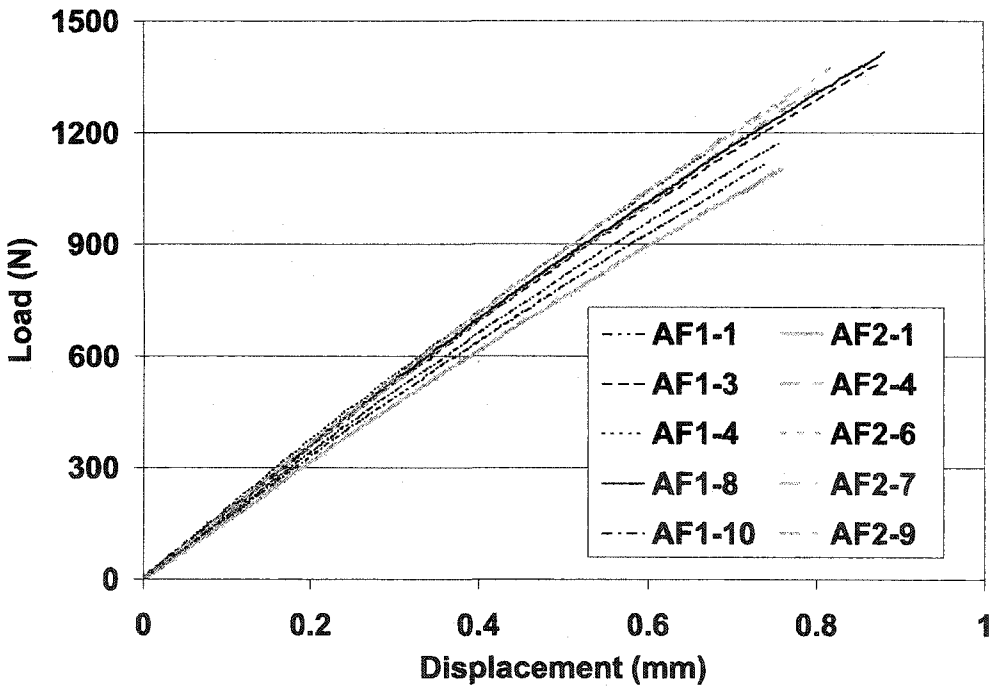

Figure E.5: Fracture load-displacement curves for AF1-2 specimens.

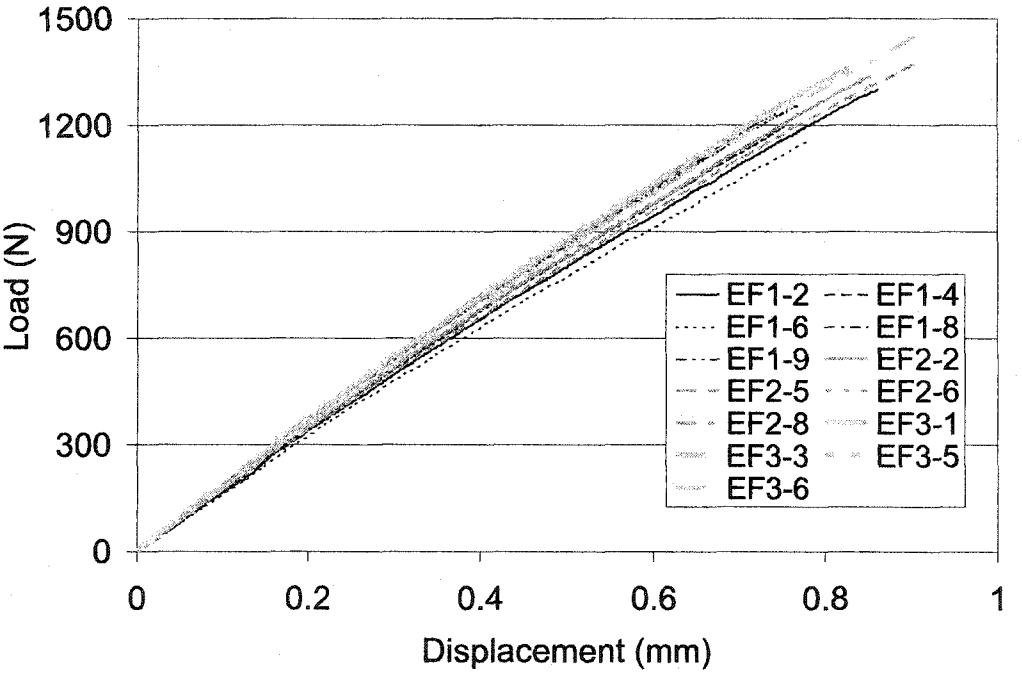

Figure E.6: Fracture load-displacement curves for EF1-3 specimens.

Appendix F

Stress Strain Curve Data Summary

Table F.1: Summary of average Young's Modulus, failure stress and failure strain, and S/S curve area for treated fibre series.

Specimen	Modulus (GPa)	σ_f (MPa)	ϵ_f (%)	Curve Area (MPa%)	Comment
AF1-2	2.70	64.93	3.62	141.49	ETF
AF1-5	2.66	80.95	6.96	391.21	
AF1-6	2.75	82.87	7.90	474.77	
AF1-7	2.74	80.19	6.08	328.58	
AF2-2	2.79	85.35	7.29	441.95	
AF2-3	2.80	87.93	8.82	578.73	
AF2-5	2.79	86.89	7.71	475.85	
AF2-8	2.83	58.24	2.58	84.75	ETF
EF1-1	2.76	85.37	7.95	491.42	
EF1-3	2.76	86.47	8.88	571.56	
EF1-5	2.67	80.88	7.96	467.09	
EF1-7	2.77	66.61	3.79	154.99	ETF
EF2-1	2.64	83.65	7.83	470.17	
EF2-3	2.65	83.46	6.77	384.56	
EF2-4	2.75	82.94	7.47	437.97	
EF2-7	2.76	79.95	5.98	322.39	
EF3-2	2.85	85.38	8.38	536.14	
EF3-4	2.77	79.85	5.52	290.56	
EF3-7	2.82	75.05	4.70	225.68	

ETF = end-tab failure

Table F.2: Summary of average Young's Modulus, failure stress and failure strain, and S/S curve area for untreated fibre series.

Specimen	Modulus (GPa)	σ_f (MPa)	ϵ_f (%)	Curve Area (MPa%)	Comment
3F-1	2.96	69.00	4.04	178.44	
3F-2	2.97	70.33	4.40	202.66	
2F-1	3.22	77.11	5.33	284.12	
2F-2	3.10	73.93	5.00	252.07	
2F-6	2.88	79.39	5.00	260.79	
2P-1	2.89	67.92	3.90	164.99	
2P-2	2.88	66.34	3.80	138.04	
2P-9	2.98	71.79	3.71	162.98	

Table F.3: Summary of average Young's Modulus, failure stress and failure strain, and S/S curve area for unreinforced series.

Specimen	Modulus (GPa)	σ_f (MPa)	ϵ_f (%)	Curve Area (MPa%)	Comment
2E-1	2.57	78.11	11.34	708.19	
2E-2	2.56	67.85	5.36	252.39	
2E-8	2.43	48.15	2.38	62.8492	ETF
2EB-5	2.69	81.20	10.43	661.65	
2EB-6	2.59	69.81	4.70	208.80	ETF
2EB-9	2.53	73.14	5.98	294.54	
2EB-10	2.65	79.53	10.23	634.58	
AS-2	2.53	74.26	5.68	277.06	
AS-4	2.49	42.08	1.88	42.02	ETF
AS-6	2.28	77.77	9.4	559.13	
AS-7	2.55	68.38	4.41	93.04	ETF
AS-9	2.54	76.92	8.08	454.02	
ES-1	2.53	54.86	2.65	81.85	ETF
ES-2	2.67	34.33	1.37	36.20	ETF
ES-4	2.65	67.21	3.99	165.09	
ES-5	2.69	81.80	11.00	718.49	
ES-6	2.61	55.81	2.65	82.98	ETF

ETF = end-tab failure

Appendix G

Summary of Series 1 Testing

Figure G.1 shows that stress-strain curves for all series 1 tensile tests.

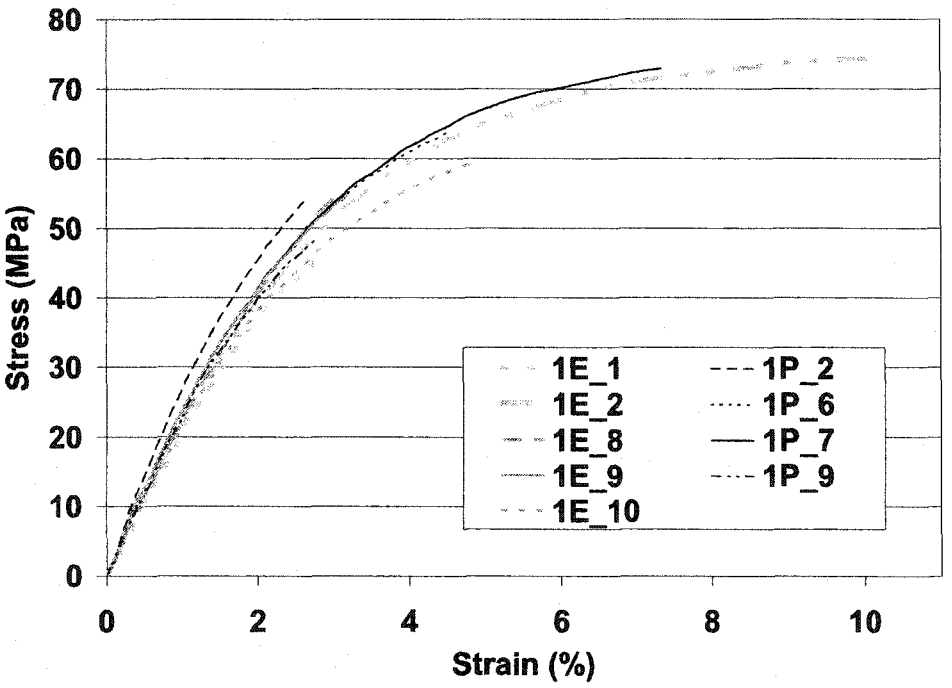

Figure G.1: Series 1: stress-strain curves.

Figure G.2 shows the stress-strain curves for extensometer and strain gauge tests in series 1.

Figure G.3 shows strain rate variation in the stress-strain responsive tensile specimens (Series 1 vs. Series 2).

Figure G.4 illustrates the variation in failure during tensile stress-strain tests for specimens with and without cloth protection.

Table G.1 provides the failure stress, failure strain and moduli for series 1 specimens.

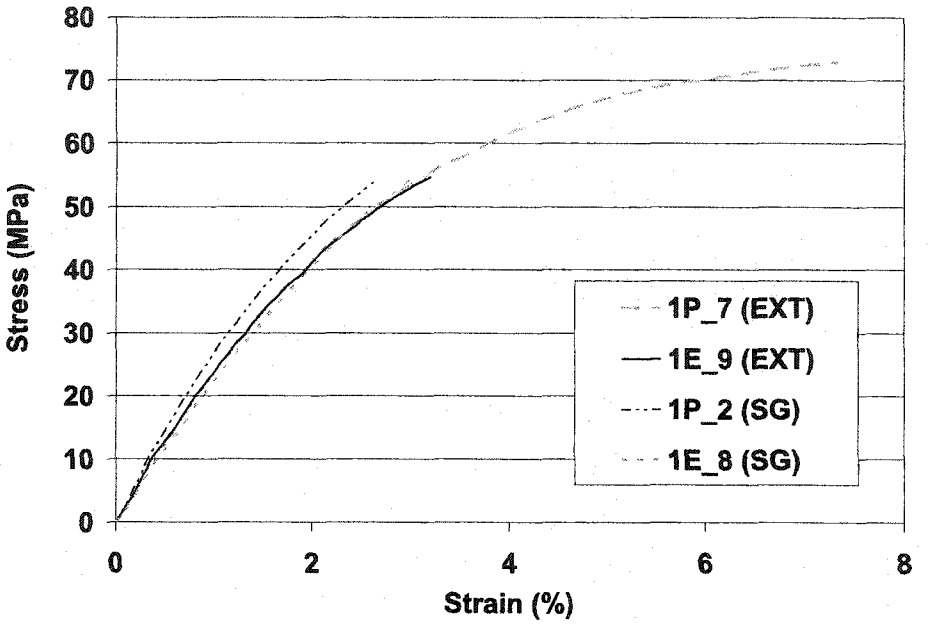

Figure G.2: Series 1: extensometer vs. strain gauge.

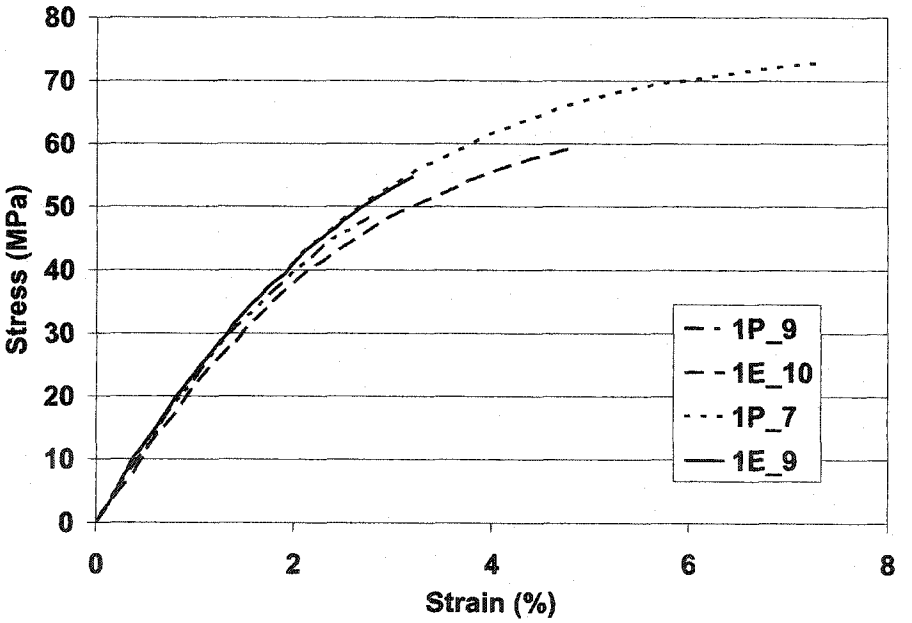

Figure G.3: Series 1: strain rate effect.

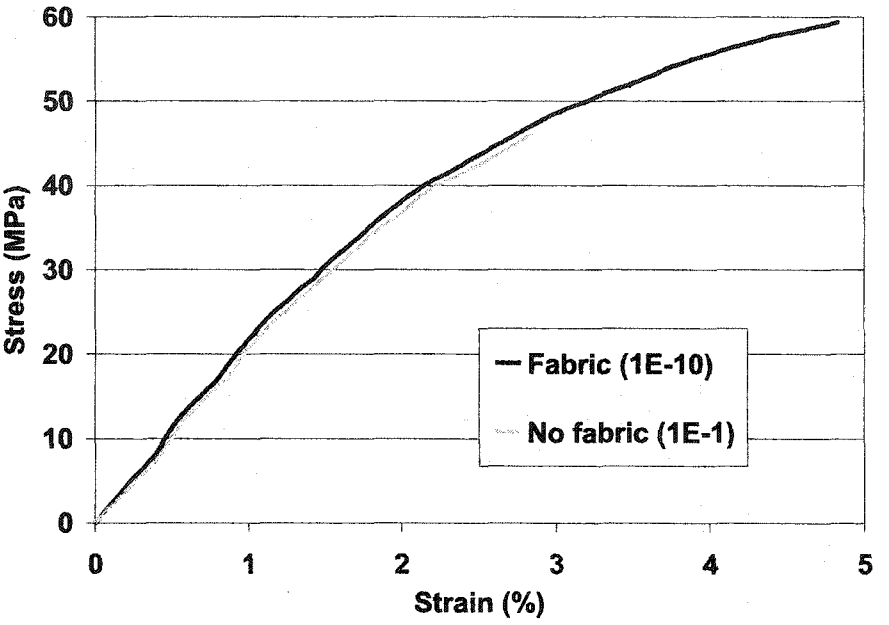

Figure G.4: Series 1: effect of fabric protector on tensile failure.

Table G.1: Summary of series 1 tensile response.

	E	σ_f	ϵ_f	Load Rate	Comment
	(GPa)	(MPa)	(%)	(N/s)	
1E-1	2.04	46.2	2.86	4.5	no cloth
1E-2	2.25	74.5	10.09	45	
1E-8	2.26	55.1	3.07	45	sg
1E-9	2.46	48.2	3.20	45	
1E-10	2.18	59.4	4.84	4.5	
1P-2	2.79	53.9	2.62	45	sg
1P-6	2.40	63.8	4.52	45	
1P-7	2.44	72.9	7.35	45	
1P-9	2.35	48.2	2.75	4.5	